Laser filaments interactions with clouds and electric fields

Schubert, Elise

UNIVERSITÉ DE GENÈVE
Département de physique appliquée

FACULTÉ DES SCIENCES
Professeur Jean-Pierre Wolf

Laser Filaments Interactions with Clouds and Electric Fields

THÈSE

présentée à la Faculté des sciences de l'Université de Genève
pour obtenir le grade de Docteur ès sciences, mention physique

par

Elise SCHUBERT

de

Genève (GE)

Thèse N° 5053

GENÈVE
Centre d'Impression de l'Université de Genève
2017

UNIVERSITÉ DE GENÈVE

FACULTÉ DES SCIENCES

Doctorat ès Sciences
Mention physique

Thèse de *Madame Elise SCHUBERT*

intitulée :

"Laser Filaments Interactions with Clouds and Electric Fields"

La Faculté des sciences, sur le préavis de Monsieur J.-P. WOLF, professeur ordinaire et directeur de thèse (Groupe de physique appliquée), Monsieur J. KASPARIAN, professeur associé (Groupe de physique appliquée), Monsieur J.-C. KIEFFER, professeur (Centre Energie Matériaux Télécommunications, Institut National de la Recherche Scientifique, Varennes (Québec), Canada) et Monsieur A. HOUARD, docteur (Laboratoire d'optique appliquée, Ecole Polytechnique, Ecole Nationale Supérieure de Techniques Avancées ParisTech, Université Paris-Saclay, Palaiseau, France), autorise l'impression de la présente thèse, sans exprimer d'opinion sur les propositions qui y sont énoncées.

Genève, le 1er mars 2017

Thèse - 5053 -

Le Décanat

N.B. - La thèse doit porter la déclaration précédente et remplir les conditions énumérées dans les "Informations relatives aux thèses de doctorat à l'Université de Genève".

Laser Filaments Interactions with Clouds and Electric Fields / by Elise Schubert

Thesis defended on March 1st, 2017 and accepted by the Faculty of Science of the University of Geneva in partial fulfillment of the requirements for the degree of Doctor of Philosophy (physics), on the recommendation of

Prof. Jean-Pierre Wolf, Université de Genève, Switzerland (supervisor)
Prof. Jérôme Kasparian, Université de Genève, Switzerland (co-supervisor)
Prof. Jean-Claude Kieffer, INRS, Canada
Dr Aurélien Houard, Ecole Polytechnique, France

Remerciements

Tout d'abord, je tiens à remercier Aurélien Houard, Jean-Claude Kieffer, Jérôme Kasparian et Jean-Pierre Wolf d'avoir accepté d'évaluer le résultat de mes trois années et demie de recherche à l'Université de Genève dans le groupe de physique appliquée.

Je remercie vivement mon directeur de thèse, Jean-Pierre Wolf, d'avoir su me convaincre d'entreprendre cette aventure. Grâce à lui, j'ai pu découvrir cette thématique fascinante et prendre part à de nombreuses collaborations internationales. Je tiens aussi à remercier tout spécialement Jérôme Kasparian, pour son optimisme et son encadrement durant toute ma thèse, ainsi que Denis Mongin et Mary Matthews pour tout ce que j'ai appris auprès d'eux jour après jour.

Merci à Michel Moret, Claudio Barreiro et Thomas Guillod pour leur aide technique visant à limiter l'utilisation du scotch carrossier et éviter les étincelles et à Luigi Bonacina et Sylvain Hermelin pour m'avoir initiée aux secrets de la technologie laser. La vie à l'université de Genève aurait aussi été bien plus compliquée sans l'aide administrative d'Isabel Vico-Fletcher, Dragana Pantelic et Nathalie Chaduiron, je vous en remercie.

Dans le cadre de mes collaborations internationales, je tiens à remercier pour leur accueil dans leur groupe Andrius Baltuška, Antoine Courjaud, Jean-Claude Diels, Knut Michel, Thomas Metzger et Audrius Pugžlys et je remercie Skirmantas, Jean-Gabriel, Chengyong, Brian, Sandro, Ali, Marcel, Valentina et Jay pour tout le temps passé à collaborer ensemble dans ces mêmes laboratoires aux quatre coins du monde. Ces collaborations furent très enrichissantes, autant du point de vue scientifique que du point de vue humain.

Merci à Debbie, Nadège et Gustavo pour les très bons moments passés dans le même bureau et un petit mot spécial à Lorena pour son excellent travail de master que j'ai eu énormément de plaisir à encadrer.

Je souhaite remercier mes collègues et amis du groupe de physique appliquée, Svetlana, Andrea, Nicolas, Adrien, Iris, Sebastien, Wahb, Julien, Geoffrey, Vasyl, Denis, Thibaud, Andrii et Cédric, ainsi que tous les collègues et amis "de l'autre côté du bâtiment", Tomer, Gianluca, Alberto, Joseph, Natalia, Valentina, Fabien, Thiago, Géraldine, Flavien, Pierre, Boris, Cyril, Jonathan, Tommaso, Anthony, Fernando, Gilles, Marc-Olivier, Denis, Peter, Nuala, Marco, Ephanielle, Emmanuel et tous ceux que j'ai bien entendu oublié de citer, ainsi que tous les étudiants de master qui sont passés au GAP durant ces trois années et demi, autant pour les nombreuses discussions scientifiques que pour tous les moments conviviaux partagés.

Je voudrais aussi remercier Patrycja Paruch, Frauke Müller, Corinne Charbonnel et Vittorio Zaccheo pour nos discussions qui m'ont beaucoup aidée en périodes de doute.

Ce travail aurait été bien plus rude sans chocolat, tartes aux poireaux, crêpes, concerts, danse et autres bons moments partagés avec mes amis, qui m'ont permis de garder les pieds sur terre, ainsi qu'à tous les membres de ma famille, qui m'ont toujours encouragée et soutenue durant mes études. Enfin, un grand merci à Julien Guillod, pour tout cela et bien plus encore.

Résumé

Ce travail rapporte différentes applications de filaments lasers dans la physique de l'atmosphère. L'attention sera plus particulièrement portée sur la propagation de faisceaux lasers dans une atmosphère turbulente, la formation d'aérosols induite par laser et l'interaction entre les filaments laser et des champs électriques.

En vue de futures campagnes d'expériences en conditions réelles, il est important de comprendre comment le faisceau laser se propage dans l'air et comment les turbulences ou les nuages peuvent affecter l'interaction des filaments laser avec l'atmosphère. Je montre que le motif géométrique des filaments dans le faisceau laser subit une transition due à l'intensité du faisceau qui est semblable à celle observée entre un gaz et un solide en physique du solide. Je démontre la robustesse du processus de filamentation quand le laser est propagé dans de mauvaises conditions atmosphériques telles que des turbulences ou de la brume.

De récentes études prédisent que les filaments laser dans l'infrarouge moyen pourraient être propagés sur de bien plus longues distances que leurs homologues dans l'infrarouge proche utilisés jusqu'alors. Ils pourraient donc augmenter le rayon d'action des filaments comme condenseurs de vapeur d'eau en gouttelettes. Ce travail présente l'étonnamment haute efficacité de formation d'aérosols des filaments lasers dans l'infrarouge moyen et des hypothèses des mécanismes sous-jacents sont proposées.

Une étude approfondie des propriétés électriques des filaments laser est discutée et les effets de la longueur d'onde, du taux de répétition et de l'intensité du champ électrique sont détaillés. Je présente une analyse de différentes techniques électriques de caractérisation du plasma créé par les filaments et définis la meilleure configuration pour analyser la densité d'ions quelques microsecondes après le passage du faisceau laser ou la densité électronique après quelques nanosecondes seulement. Je démontre grâce à des simulations que pour une énergie laser donnée, la durée de vie du plasma sera favorisée par la scission du faisceau en un train de sous-impulsions comportant chacune assez d'énergie pour créer un filament plutôt que par la propagation d'une seule impulsion créant un paquet de filaments.

Un nouveau phénomène d'interactions à distance de filaments laser avec des sources de haute tension est décrit. Les filaments lasers sont capables de supprimer des arcs électriques naturels entre deux électrodes chargées en les déchargeant progressivement, et ceci même à distance.

Finalement, je montre que le déclenchement et le guidage de décharges par des filaments laser dans l'ultraviolet est bien plus efficace que dans l'infrarouge proche. L'addition d'impulsions nanosecondes de lasers Nd :YAG (1064 nm et 532 nm) de l'ordre du Joule n'est pas suffisante pour augmenter la probabilité de déclenchement de décharge, bien que cet ajout augmente de manière significative la vitesse et la longueur de guidage des arcs électriques.

Abstract

This work reports different applications of laser filaments in atmospheric physics such as the propagation of light in a turbulent atmosphere, laser-induced aerosol formation or interactions between laser filaments and electric fields.

In order to achieve field experiments with lasers in the real atmosphere, it is important to understand how the beam propagates in the air and how turbulence or clouds on the beam propagation path can impact the laser filament interaction with the atmosphere. I show that the geometrical patterns of filaments within the laser beam follow a transition driven by the beam light intensity, similar to gas-solid phase transitions in solid matter physics. I demonstrate the robustness of the filamentation process when the laser is propagated through adverse conditions such as turbulent or foggy air.

Mid-infrared laser filaments are expected to propagate over longer distances than their near-infrared counterparts used up to now. They could therefore increase their range of action as water vapor condensers into droplets. The surprisingly high efficiency of aerosol formation by mid-infrared laser filaments is demonstrated in this work and hypotheses of the underlying mechanisms are given.

A thorough study of laser filaments electrical properties, which depend on the laser wavelength, the repetition rate and the electric field in which the laser is propagated is also discussed. I present an analysis of different plasma electric characterization techniques and define the most suitable configuration for an analysis of the ionic charge, microseconds after the beam propagation, or of the free electron density nanoseconds after it. I demonstrate through simulations that for a given available laser energy, plasma channels lasting longer can be created by the time partitioning of energy in a train of sub-pulses, each of them bearing enough energy to create a light filament.

A new phenomenon of remote interactions of laser filaments with high voltage sources is presented. Laser filaments can suppress natural breakdown between two charged electrodes by progressively unloading them, even from a distance.

Finally, discharge triggering and guiding by laser filaments in the ultraviolet range is proven to be much more efficient than in the near-infrared. It is demonstrated that adding Joule-class Nd:YAG nanosecond pulses (1064 nm and 532 nm) is not sufficient to increase the discharge triggering probability, although significantly accelerating and increasing the guided length of the electrical arc.

Contents

Résumé vii

Abstract ix

Introduction 3

1 Laser Filamentation in the Atmosphere 5
1.1 Nonlinear Processes in Ultrashort Laser Beams 6
1.1.1 Underlying Physics of Laser Filamentation 6
1.1.2 Several Properties of Laser Filaments in Air 9
1.1.3 Laser Filamentation in the Ultraviolet and Mid-Infrared 10
1.1.4 Multiple Filamentation 11
1.2 Gas-Solid Phase Transition in Laser Multiple Filamentation 12
1.2.1 Experimental Setup 13
1.2.2 Results and Discussion 13
1.2.3 Conclusion 18

2 Kilohertz Laser Filaments in Adverse Atmospheric Conditions 19
2.1 Dual-scale Turbulence in High Average Power Laser Filaments 20
2.1.1 Atmospheric Turbulence 20
2.1.2 Experimental Setup 21
2.1.3 Results 22
2.1.4 Conclusion 25
2.2 High Repetition Rate Ultrashort Laser Drills a Path through Fog 26
2.2.1 Interactions of Atmospheric Particles with Light 26
2.2.2 Experimental Setup 28
2.2.3 Results 29
2.3 Conclusion 32

3 Mid-Infrared Laser-Induced Condensation in Air 33
3.1 Background of Atmospheric Aerosol Condensation 34
3.1.1 Gases Present in the Atmosphere 34
3.1.2 Atmospheric Aerosols 35
3.1.3 Nucleation 36
3.1.4 Laser-Induced Aerosol Condensation 37
3.2 First Results of Mid-Infrared Laser-Induced Condensation in Air 38
3.2.1 Material and Methods 38

3.2.2 Results . . . 39
3.2.3 Discussion . . . 41
3.3 Conclusion . . . 42

4 How to Accurately Characterize Filament Charge Density 43
4.1 Experimental Setup . . . 44
4.2 Results . . . 45
4.2.1 Ionic Current . . . 47
4.2.2 Fast Polarization Signal . . . 49
4.2.3 Electronic Current Signal . . . 50
4.2.4 Comparison of the Three Signals . . . 51
4.3 Conclusion . . . 52

5 Optimal Laser Pulse Energy Partitioning for Air Ionization 53
5.1 Material and Methods . . . 54
5.1.1 Modeling . . . 55
5.2 Results and Discussion . . . 57
5.2.1 Experiments . . . 57
5.2.2 Simulations . . . 60
5.3 Conclusion . . . 61

6 Interactions of Laser Filaments with DC High-Voltage Sources 63
6.1 Electrical Breakdown Steps . . . 65
6.2 Remote Electrical Arc Suppression by Laser Filaments . . . 67
6.2.1 Experimental Setup . . . 67
6.2.2 Electrical Arc Suppression . . . 67
6.2.3 Influence of Wind on Discharge Triggering . . . 68
6.2.4 Discussion . . . 69
6.3 Charge Neutralization by Laser Filaments . . . 70
6.3.1 Experimental Setup . . . 70
6.3.2 Spark-Free Neutralization . . . 71
6.3.3 Geometrical Considerations . . . 72
6.3.4 Influence of the Average Power and Repetition Rate . . . 74
6.3.5 Influence of Wind . . . 75
6.3.6 Discussion . . . 75
6.4 Conclusion . . . 76

7 Discharge Triggering with Ultraviolet Laser Filaments 79
7.1 Material and methods . . . 79
7.2 Faster Discharge Triggering with Nanosecond Lasers . . . 81
7.3 Conclusion . . . 84

Conclusion 88

A Non-Linear Photochemical Pathways in Laser-Induced Atmospheric Aerosol Formation 89

B Conductivity and Discharge Guiding Properties of Mid-Infrared Laser Filaments 99

Bibliography 107

Index 125

Introduction

Humans have tried for ages to control the weather in order to avoid floods, drought or the dangers due to lightning strikes, first through religious practices and for the last century, through scientific experiments.

Considerable efforts have been made to control water condensation and rain, especially in the USA and in China. Seventy years ago, Langmuir (1947) demonstrated that water clouds could be formed by spraying small particles of dry ice in the atmosphere. Further experiments by Schaefer (1950) showed that similar results could be obtained with silver iodide or other salts. This technique, called *cloud seeding*, is mainly used in the USA (Saleeby *et al.*, 2011) and in China, which spends between 400 million and 700 million yuan (60-100 million US dollars) per year in its program for weather modification. They claim that cloud seeding controls when and where the rain will fall from the clouds and have used this technology during the Olympic games of 2008 in Beijing, although results are still controversial (Qiu & Cressey, 2008). Besides the question of the cloud seeding by salts or dry ice efficiency, the particles sprayed in the atmosphere could be harmful when they fall back on the ground.

On the other hand, although lightning rods have been invented by Benjamin Franklin in 1749 already, the fast growth of electronic devices very sensitive to electromagnetic fields created by lightning strikes has pushed scientists to find ways of diverting lightning strikes from sensitive buildings instead of attracting them with lightning rods. For fifty years, rockets followed by a conductive cable are used in scientific studies to trigger and guide lightning to the ground and divert them from sensitive sites, the goal being to protect for example airports, power plants or refineries. However, this technique suffers from severe limitations as the number of lightning strikes that can be triggered is at most as high as the number of rockets available (Gary, 2004).

Laser pulses could be good candidates for cloud seeding and lightning triggering and guiding with no other mean than light. Since the invention of the laser by Maiman (1960), lasers have been used in virtually all domains of the everyday life, from the small laser pointer for conferences to optical communication systems (DeCusatis, 2013). In specialized domains, they are used for precision contact-less measurements and machining (Chryssolouris, 2013) and as powerful tools in spectroscopy (Demtröder, 2013), microscopy (Zipfel *et al.*, 2003), medical applications (Berlien *et al.*, 2012) and many others.

In atmospheric physics, LIDAR technology allows remote measurements of wind velocity, temperature, water and pollutants concentration by mean of low intensity lasers, typically in the megawatt per squared centimeter range (Weitkamp, 2006). With such intensities, the beam light does not modify the propagation medium and is only used as a probe.

The invention of the *Chirped Pulse Amplification* (CPA) technique by Strickland & Mourou (1985) allowed the development of ultrashort laser pulses in the femtosecond range with very high powers in the gigawatt to terawatt regime, leading to intensities above the terawatt per squared

centimeter. At such a high intensity, the frontier of nonlinear optics is broken. Braun *et al.* (1995) demonstrated that very intense and narrow light structures around 1 to 100 TW/cm^2 called *filaments* are formed within the laser beam and propagate over distances from the centimeter to the hundred meters (Rodriguez *et al.*, 2004, Durand *et al.*, 2013). These light structures create a plasma of free electrons by photo-ionizing or photo-dissociating electrons from atoms or molecules. This changes the thermodynamic equilibrium between air constituents and can trigger atmospheric processes such as aerosol formation and growth or triggering and guiding of electric breakdown.

Rohwetter *et al.* (2010), Henin *et al.* (2011), Petit *et al.* (2011a) and Ju *et al.* (2012) demonstrated aerosol formation and water condensation with 800 nm laser filaments in laboratory as well as in field experiments. The underlying mechanism behind this laser-induced condensation remained however unclear.

Koopman & Wilkerson (1971) proved before the discovery of laser filaments that a high-power neodymium laser beam at 1 µm wavelength could guide an electrical discharge on short distances. Miki *et al.* (1993) demonstrated that very energetic nanosecond pulses from CO_2 lasers could guide electrical arcs but the guiding length was very short as the plasma generated by those long pulses is opaque. Uchida *et al.* (1999) also used a complicated system of three laser sources in the mid-infrared and cylindrical lenses to attempt to guide lightning in field experiments along the Japanese sea shore. Laser filament electrical discharge triggering and guiding by short laser pulses have been demonstrated in the near-infrared by La Fontaine *et al.* (2000) and in the ultraviolet by Zhao *et al.* (1995). The triggering and guiding of discharges by laser filaments is however not achieved yet on distances longer than a few meters as the lifetime of the plasma channel created by the laser filament is shorter than the time needed for an electrical arc to propagate through this channel.

Recently, attention has been drawn upon laser technology developments as well in the near-infrared by the development of high repetition rate lasers and high average power lasers as in other wavelengths such as the mid-infrared and the ultraviolet. Mitrofanov *et al.* (2015), Panagiotopoulos *et al.* (2015) and Geints & Zemlyanov (2014) showed that laser filaments in the mid-infrared are much wider than their near-infrared counterparts and can propagated with very high intensities over hundreds of meters. In the ultraviolet, the photo-ionization and photo-dissociation is much more efficient than in the near-infrared because of the wavelength-dependency of the process. The created plasma could therefore demonstrate interesting properties.

This work reports different applications of ultrashort laser pulses in atmospheric physics such as propagation of light in a turbulent atmosphere, laser-induced aerosol formation or interactions between ultrashort laser pulses and electric fields.

In the first part of this work, the properties of laser filaments propagating in the atmosphere are discussed in Chapter 1 and 2. In order to achieve field experiments in the atmosphere, it is important to understand how the beam propagates in the air and how the turbulences or the clouds on the beam propagation path can impact the efficiency of the laser filament interaction with the atmosphere. The geometrical patterns of filaments within the laser beam and the robustness of the filamentation process when the laser is propagated through adverse conditions such as turbulent or foggy air are investigated.

The second part discusses the laser-induced aerosol formation in air by a mid-infrared laser in Chapter 3. As mid-infrared laser pulses are expected to propagate over longer distances than their near-infrared counterparts used up to now, they could increase their range of action as water condensers.

The third part deals with the electrical properties of laser filaments. After a methodological study on how to accurately characterize the charge in the plasma in Chapter 4, a theoretical and experimental study of the laser energy partitioning into trains of sub-pulses to increase the plasma lifetime are discussed in Chapter 5. The remote interactions of laser filaments with high voltage sources, which was to the best of my knowledge never discussed before in the literature, are presented in Chapter 6. Finally, Diels & Zhao (1992) suggested to improve the triggering and guiding of discharges with ultraviolet laser filaments by adding a long visible pulse to the ultraviolet beam. I studied this, as well as the addition of a long near-infrared pulse, and I present those results in Chapter 7.

Two articles on the same research field for which I was a less involved coauthor are placed in the appendix at the end of this work.

Laser Filamentation in the Atmosphere 1

Since the mid-sixties, it was known that intense nanosecond pulses undergo self-focusing that generates filaments of light able to damage optics on the beam path and which therefore limited the design of high-power lasers (Chiao *et al.*, 1964, Hercher, 1964, Marburger & Dawes, 1968).

The development of the *Chirped Pulse Amplication* technique (CPA) by Strickland & Mourou (1985) allowed the amplification of mode-locked ultrashort pulses in the femtosecond range. These femtosecond pulses reached peak powers higher than the gigawatt powers of nanosecond pulses while keeping a lower average power. Braun *et al.* (1995) observed that launching such near-infrared pulses of 10 GW peak power in the air resulted in the spontaneous formation of narrow self-guided light structures, or *filaments*.

In the first part of this chapter, an overview of general physical properties of laser filaments during their propagation in the atmosphere will be made, derived from Couairon & Mysyrowicz (2007), Boyd (2008) and Henin (2013). It is however beyond the scope of this work to give a comprehensive view of the filament regime and of the filaments applications. Several authors such as Bergé *et al.* (2007), Couairon & Mysyrowicz (2007), Kasparian & Wolf (2008) and Chin *et al.* (2012) published detailed reviews on the topic.

In the second part, an experimental study of the geometrical arrangement of laser filaments within the laser beam will be discussed in detail. I have contributed to these results by taking part in the preparation and data recording of the experiment, which have been submitted for publication.

1.1 Nonlinear Processes in Ultrashort Laser Beams

Although laser filamentation has been studied for over twenty years, there is still no universally accepted definition among scientists of what is a filament and this fundamental issue is beyond the scope of this work. In the case of atmospheric physics, a laser filament can be thought of as a narrow and intense light structure that spontaneously arises at a remote location and keeps a self-confined structure over an extended length, beyond the Rayleigh length, while ionizing the air.

1.1.1 Underlying Physics of Laser Filamentation

In the following, the physical processes at work in laser filamentation will be explained in detail.

Optical Kerr Effect

In linear optics, when light propagates through an isotropic polarizable medium such as air, the instantaneous polarization P is directly proportional to the light electric field E

$$P = \varepsilon_0 \chi^{(1)} E \tag{1.1}$$

where $\chi^{(1)}$ is the first order susceptibility of the propagation medium and ε_0 is the permittivity of vacuum. For simplicity, a scalar formalism is kept throughout the text, corresponding to a linearly polarized field in an isotropic medium. The resulting linear refractive index of the medium is

$$n_0 = \sqrt{1 + \chi^{(1)}} \tag{1.2}$$

When the intensity $I = \frac{1}{2}\varepsilon_0 c \langle |E|^2 \rangle$ of the light is high, Equation (1.1) does not hold anymore. It can be generalized by expressing the polarization as a power series in the field E as

$$P = \varepsilon_0 \chi^{(1)} E + \varepsilon_0 \chi^{(2)} EE + \varepsilon_0 \chi^{(3)} EEE + ... \tag{1.3}$$

In centrosymmetric materials such as gases, all even terms of χ vanish and at the third order, the nonlinear polarization can be rewritten as

$$P = \varepsilon_0 \chi^{(1)} E + \varepsilon_0 \chi^{(3)} EEE \tag{1.4}$$

In the same way, the nonlinear refractive index becomes

$$n = \sqrt{1 + \chi^{(1)} + \chi^{(3)} \langle |E|^2 \rangle} \approx n_0 + n_2 I \tag{1.5}$$

Therefore, the effect of a strong optical field is to locally modulate the refractive index of the medium by superimposing to the constant linear term n_0 an intensity-dependent term $n_2 I$. This is called the optical Kerr effect and the *nonlinear refractive index* n_2 is given by

$$n_2 = \frac{3\chi^{(3)}}{4 n_0^2 \varepsilon_0 c} \tag{1.6}$$

As an example, the nonlinear refractive index of air is $n_2 = 3.2 \cdot 10^{-19}\,\mathrm{cm}^2/\mathrm{W}$ for a pulse centered at 800 nm, as reported by Couairon & Mysyrowicz (2007).

The change in refractive index, $\Delta n \approx n_2 I$, is usually positive as $\chi^{(3)}$ is positive in most media. Therefore, the phase velocity of light is reduced when the light intensity is increased. For example, if the laser beam transverse profile is assumed to be Gaussian, Δn will also be Gaussian, reaching its maximum at the center of the beam. The resulting wavefront will therefore bend as if propagating through a focusing optical lens, hence the reference to *Kerr-lens* effect or *self-focusing* to describe this phenomenon.

The self-trapping of light, or filamentation, occurs when the self-focusing is stronger than diffraction effects. This threshold was used by Marburger (1975) to define the *critical power* of the laser beam above which a filament can form

$$P_{\mathrm{cr}} \equiv \frac{3.72\lambda_0^2}{8\pi n_0 n_2} \tag{1.7}$$

When P_{cr} is reached, the beam self-focuses. The intensity within the self-focused region increases and nonlinear effects take place.

Ionization and Plasma Defocusing

Photo-ionization is the extraction of an electron from a molecule or an atom by one or many photons. In the latter case, one talks of *multi-photon ionization* (MPI). When the light self-focuses, the intensity increases to a few tens of terawatts per squared centimeters and with it the probability of multi-photon ionization, which scales as I^K, where K is the number of photons needed to extract one electron from a given molecule with photons of a given wavelength. For example, 12.06 eV are needed to extract the outer electron of an O_2 molecule (Couairon & Mysyrowicz, 2007). This means that eight photons are needed at 800 nm to ionize one single O_2 molecule.

When the field interaction with atoms is strong, the Coulomb barrier of the atom is distorted by the field and an electron can escape by passing through the barrier. This process is called *tunnel ionization* and different simulation codes such as the Perelomov, Popov, & Terent'ev (1966) (PPT) formula used in Chapter 5 are based on this interaction.

Keldysh (1965) demonstrated that the *Keldysh parameter* γ_k indicates the transition between those two distinct regimes. When $\gamma_k \gg 1$, the regime is non-resonant and multi-photon ionization is dominant, whereas when $\gamma_k \ll 1$, the regime is resonant and tunnel ionization dominates

$$\gamma_k = \frac{2\pi c}{|e|\lambda}\sqrt{\frac{2m_e U_i}{I}} \tag{1.8}$$

where c is the speed of light, e and m_e are the electron charge and mass, U_i is the ionization potential and I and λ are the intensity and wavelength of the light. In the near-infrared, γ_k is not in one of the limit cases and both multi-photon and tunnel ionization occur.

As reported by Feit & Fleck Jr (1974), the plasma of electrons has a negative contribution to the refractive index

$$n \approx n_0 - \frac{N_e}{2N_{\mathrm{cr}}} \qquad \Rightarrow \qquad \Delta n_{\mathrm{plasma}} = -\frac{N_e}{2N_{\mathrm{cr}}} \tag{1.9}$$

where N_e is the free electron density and $N_{\mathrm{cr}} = \varepsilon_0 m_e \omega^2 / e^2$ is the critical plasma density value above which the plasma becomes opaque, m_e and e being the electron mass and charge and ω_0 the laser frequency (at 800 nm, $N_{\mathrm{cr}} \sim 1.7 \cdot 10^{23}\ \mathrm{m}^{-3}$). The negative refractive index variation therefore counterbalances the Kerr-lens effect.

Laser filamentation stems from the interplay of self-focusing by Kerr effect and plasma defocusing by photo-ionization and it leads to refocusing cycles that maintain the filament diameter approximately constant over a distance longer than several Rayleigh lengths, up to tens of meters and above, as reported by La Fontaine *et al.* (1999), Durand *et al.* (2013) and Rodriguez *et al.* (2004). The balance between those two effects also lead the light intensity to saturate at a fixed value within the laser filament, as demonstrated by Kasparian *et al.* (2000). This phenomenon is called *intensity clamping*. At 800 nm, the filament has a diameter of 100–200 µm, keeps an almost fixed energy of a few millijoules and an intensity around 50 TW/cm^2 according to Kasparian *et al.* (2000).

Photon Bath

Filaments cannot be considered as virtual optical fibers guiding the light within their core. Courvoisier *et al.* (2003), Kolesik & Moloney (2004), Skupin *et al.* (2004b) and Liu *et al.* (2005) showed that they continuously interact and exchange energy with the *photon bath* surrounding them. This photon bath, also called *energy reservoir* by Liu *et al.* (2005), Eisenmann *et al.* (2008) and Mills *et al.* (2013), consists of the photons in the laser beam that are not within the filament volume but a few millimeters around it.

The photon bath plays a key role in the filamentation process. In particular, the photon bath feeds the filament and balances its energy losses due to ionization, allowing it to self-heal after an obstacle as demonstrated by Courvoisier *et al.* (2003), Kolesik & Moloney (2004) and Skupin *et al.* (2004b) or to extend its propagation distance as shown by Scheller *et al.* (2014).

Self-Phase Modulation

As described above, the nonlinear refractive index, modulated by the spatial light intensity gradient, leads to self-focusing of the beam. In the same way, as $n(r,t) = n_0 + n_2 I(r,t)$, the temporal intensity variation will lead to the appearance of new frequencies in the spectrum of the laser pulse. This effect is called *self-phase modulation* (SPM). After a propagation over a distance z, the phase is modulated by the nonlinear refractive index as

$$\phi(z,t) = \phi_0 + \frac{\omega_0}{c}\int_0^z n_2 I(z',t)\, dz' \tag{1.10}$$

where ϕ_0 is the initial phase of the electric field and ω is the carrier frequency. Therefore, the phase offset due to the nonlinearity over a length z is $\Delta\phi = n_2\omega I z/c$ and the instantaneous frequency is

$$\omega(t) = -\frac{\partial\phi(t)}{\partial t} \approx \omega_0 - \frac{z\omega_0 n_2}{c}\frac{\partial I}{\partial t} \qquad \Rightarrow \qquad \Delta\omega(t) = -\frac{z\omega_0 n_2}{c}\frac{\partial I}{\partial t} \tag{1.11}$$

In other words, the rising edge of the electromagnetic wave generates redder frequencies while the trailing edge adds bluer frequencies to the initial spectrum. Self-phase modulation therefore broadens the spectrum, phenomenon also called *white-light generation* or *supercontinuum generation*. The emitted light preserves the coherence of the driving electromagnetic field, even between different filaments within the same laser beam (Henin, 2013). The white-light beam generated during filamentation consists of a white spot at the position of the filament surrounded by a distribution of colored rings, as shown in Figure 1.1.

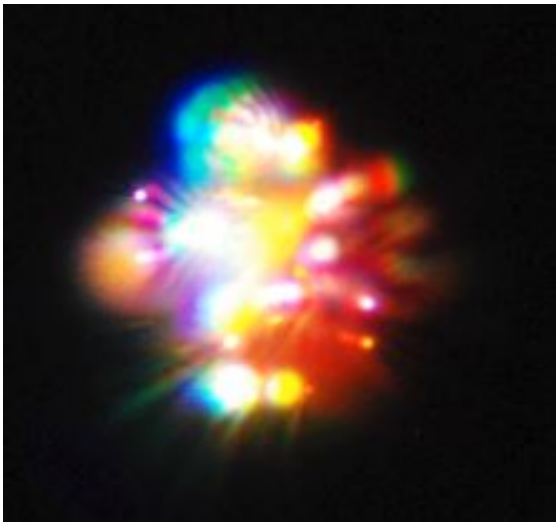

Figure 1.1: Conical emission from multiple filaments from the TERAMOBILE laser beam (800 nm, 200 mJ, 100 fs). The bright round spots are filaments and the colors are due to conical emission.

1.1.2 Several Properties of Laser Filaments in Air

As discussed above, plasma is created during the propagation of a laser filament in air. This plasma creation leads to many physical processes within the filament volume. First of all, the release of free charges helps creating clusters of a few molecules, especially for polarized molecules such as H_2O, which will then lead to aerosol formation, as it will be described in Chapter 3. If the laser filament is propagated in an electric field, the free charges create a conductive channel within the filament volume, a property which will be described and used in Chapter 4 to 7.

The excitation of nitrogen molecules is visible by eye in part of the filament volume. The fluorescence ratio of the 391 nm and 337 nm lines of N_2 molecules has been used by Xu *et al.* (2012) to determine the length of laser filaments while the backscattered fluorescence has been used by Hosseini *et al.* (2003) to determine this length remotely via LIDAR technique (light detection and ranging technique, Measures (1984)).

Vidal *et al.* (2000), Cheng *et al.* (2013), Jhajj *et al.* (2014) and Lahav *et al.* (2014) demonstrated that laser filaments act as thermal sources which generate a radial expansion of the plasma, therefore decreasing the air particle density in the region where the laser filament has propagated. This density rarefaction takes place within 0.1 µs and lasts up to hundreds of microseconds. It generates a shock wave that can be heard by naked ear and which is called *plasma noise* in this work. This plasma noise was used by Yu *et al.* (2003) to characterize the filament length. The more efficiently the filament heats the air, the stronger the shock wave, hence the choice in many of the experiments described in this work to place the experimental setup where the plasma noise was the strongest.

The radial expansion of the gas heated by the filament continues until the pressure balance with the external gas is restored, leading to a density dip several hundreds of micrometers wide and lasting up to a millisecond (Cheng *et al.*, 2013). This density profile has been used by Jhajj *et al.* (2014) to guide a nanosecond laser pulse at 532 nm while Vidal *et al.* (2000) identified this mechanism as improving the triggering and guiding of electrical discharges as it will be discussed in detail in Chapter 6.

1.1.3 Laser Filamentation in the Ultraviolet and Mid-Infrared

All the examples up to now in this section have been concentrating on near-infrared laser filaments at 800 nm. Indeed, the technology for reaching the filament regime at this wavelength is available for almost thirty years and the phenomenon has been investigated since twenty years, as discussed in the introduction of this chapter. Table 1.1 summarizes some relevant parameters for filaments at 800 and 1030 nm.

Laser filaments have also different properties depending on their wavelength and as ultraviolet and mid-infrared laser beams are also used in the experiments described in this work, here is a short review of the main differences between those wavelengths and the more well-known case of the near-infrared.

Mid-Infrared Laser Filaments

Femtosecond mid-infrared filaments of 2 to 10 µm wavelength have recently attracted much attention because of their unique properties as compared to their more traditional counterparts in the visible and near infrared spectral range. They are expected to produce single millimeter size "optical pillars" bearing very high intensities over hundreds of meters according to Mitrofanov *et al.* (2015), Panagiotopoulos *et al.* (2015) and Geints & Zemlyanov (2014), which is impossible to achieve at shorter wavelengths. The difference in the filamentation process between the near-infrared and the mid-infrared regimes relates, to a large extent, to the λ^2 dependence of the critical power in Equation (1.7). While Couairon & Mysyrowicz (2007) showed that $P_{cr} \approx 3.3$ GW at 800 nm and Houard *et al.* (2016) demonstrated that $P_{cr} \approx 5.3$ GW at 1030 nm, P_{cr} reaches 80 GW at 3.9 µm according to Mitrofanov *et al.* (2015).

The first experimental observation of mid-infrared filaments in gases was achieved in 4 bar pressure Argon by Kartashov *et al.* (2012), using *Optical Parametric Chirped Pulse Amplification* (OPCPA) technologies at 3.9 µm developed by Andriukaitis *et al.* (2015). Thanks to further development of this unique system by Mitrofanov *et al.* (2015), reaching now around 280 GW $\approx 3.5 P_{cr}$ and energies up to 30 mJ, they demonstrated for the first time the propagation of mid-infrared filaments in atmospheric air. Significant work is currently carried out for developing mid-infrared multi-terawatt sources, including scaling up OPCPAs and ultrashort laser seeded high pressure CO_2 amplifiers (Polyanskiy *et al.*, 2015, Haberberger *et al.*, 2010, Lassonde *et al.*, 2015).

Table 1.1 summarizes some relevant parameters for filaments at 3.9 µm.

Ultraviolet Laser Filaments

Experiments and simulations showed that ultraviolet laser filaments were around the same width than those at 800 nm, ranging from 80 to 200 µm (Schwarz *et al.*, 2000, Tzortzakis *et al.*, 2000a). The three photons needed to photo-ionize oxygen and nitrogen in the ultraviolet is much smaller than in the near to mid-infrared and the peak intensity of ultraviolet filaments is therefore much lower than at longer wavelengths (see Table 1.1). Therefore, ultraviolet laser pulses are expected to ionize the air much better than near-infrared pulses. This should lead to better conduction of high-voltage electrical breakdown and better condensation of aerosols than with near-infrared pulses.

Ultraviolet laser filaments have been used for discharge triggering and guiding since more than twenty years (Zhao *et al.*, 1995). However, the technology to obtain stable and reliable

high-power lasers in the ultraviolet has been difficult to achieve as ultraviolet suffers from high absorption and diffraction in air and optics. Recently, interest for ultraviolet laser filaments has regained popularity in the field and Dergachev *et al.* (2013), Geints *et al.* (2015), Zvorykin *et al.* (2015a) and Smetanin *et al.* (2016) have published results comparing ultraviolet laser filaments beams to their near-infrared counterparts. Some experiments have also been conducted recently by Matthews *et al.* (2013) and Joly *et al.* (2013) to compare aerosol formation by ultraviolet and near-infrared laser filaments. Table 1.1 summarizes some relevant parameters for filaments at 266 nm.

λ (nm)	266	800	1030	3900
$\varnothing$ (µm)	80–150 [a]	100–200 [c]		600–800 [e]
I_{peak} (TW/cm^2)	1–2 [a]	50 [c]	23 [d]	20 [e]
P_{cr} (GW)	0.1 [b]	3.3 [c]	5.3 [d]	80 [f]
K_{O_2} (photons)	3	8	11	38
K_{N_2} (photons)	4	11	13	49

Table 1.1: Filament diameter and peak intensity, critical power and calculated number of photons for multi-photon ionization at different wavelengths used in this thesis. a: Schwarz *et al.* (2000); b: Smetanin *et al.* (2016); c: Couairon & Mysyrowicz (2007); d: Houard *et al.* (2016); e: Mongin *et al.* (2016b); f: Mitrofanov *et al.* (2015).

1.1.4 Multiple Filamentation

When the laser beam peak power is far above the critical power P_{cr} described in Section 1.1.1, the local power in the filament is high enough to allow filamentation at places where the light intensity is high. Therefore, filaments tend to appear on beam profile inhomogeneities which can be caused by optics such as astigmatism, by inhomogeneous amplification of the beam or external turbulence caused by heat gradients along the beam as it will be discussed in more details in Chapter 2. At long wavelengths such as the mid-infrared, filaments appear insensitive to spatial break-up into multiple filaments because of the λ^2 dependency of the critical power in Equation (1.7), as discussed above.

The behavior of filaments is very rich and their interactions within the beam through the photon bath can be explained by statistical physics and condensed matter physics (Ettoumi *et al.*, 2015a,b). In the next section, this will be illustrated by an experimental and theoretical study for which I participated experimentally.

1.2 Gas-Solid Phase Transition in Laser Multiple Filamentation

Many physical systems are well described by statistical models driven by nearest-neighbor interactions, such as spin models (Marro & Dickman, 2005, Kosterlitz & Thouless, 1973, Rogers & Desai, 1989). Recently, Ettoumi *et al.* (2015a,b) showed that the formation of multiple filamentation patterns in high-power ultrashort laser pulses also belong to this category.

As discussed above, in the case of multiple filamentation, the laser energy reservoir mediates interactions between neighboring filaments as shown by Bergé *et al.* (1997), Ren *et al.* (2000), Bergé *et al.* (2003), Hosseini *et al.* (2004a), Ma *et al.* (2008), D'Asaro *et al.* (2009) and Stelmaszczyk *et al.* (2009). Xi *et al.* (2006) and Shim *et al.* (2010) showed that this interaction is attractive if the filaments are in phase, and repulsive if they are in antiphase, corresponding to constructive and destructive interferences in the photon bath, respectively. Previous theoretical and experimental studies by Shim *et al.* (2012) have shown that the relative phase between filaments is mainly driven by the random intensity fluctuations during the collapse and that it is then stabilized for the filaments propagating after the collapse, as shown by Jhajj *et al.* (2016).

Recently Henin *et al.* (2010) showed that at laser powers exceeding 100 TW, this mutual interaction limits the density of filaments in the transverse beam profile, resulting in the rise of the photon bath intensity. As a consequence, the photon bath effectively contributes to nonlinear effects like white-light generation (Petit *et al.*, 2011b) or laser-induced condensation (Petrarca *et al.*, 2011), resulting in an overall increase of the yield of these processes.

The unexpected limitation of the number of filaments in the beam cross-section by the available space instead of the available power drove the interest to investigate this phenomenon in more depth. Many previous studies such as those by Méjean *et al.* (2005), Skupin *et al.* (2004a), Méchain *et al.* (2005) and Béjot *et al.* (2007) reported indeed that the number of filaments is directly proportional to the available power, and more precisely that the formation of each filament would require typically 5 critical powers P_{cr}. Since the space-limited filament formation was observed at 100 TW, this suggested the existence of a threshold between two different regimes.

Here, the generality of this transition is demonstrated, also for lower powers, and it is shown that the driving parameter of this transition is intensity and not power. Finally, the transition for near-infrared multi-terawatt beams it shown to occur at an intensity of 0.4 TW/cm^2. Above this threshold, the density of filaments is not limited by the available power but by their mutual interaction. In this situation, the local filament density saturates around 12 cm^{-2}, with fixed characteristic distances which reminds the structure of a solid. The two regimes can thus be considered as two phases, one close to a gas, where filaments have negligible interaction, and one close to a solid, where distances are determined by the balance between attractive interactions through Kerr effect and repulsive interactions from diffraction and plasma generation. The transition between these two phases is induced by increasing the equivalent of a pressure, i.e. the light intensity over the beam section in the case of this study. This work therefore offers an analogy between atomic/solid state physics and multifilamentation phenomena, where the organization of filaments in the transverse beam of a given intensity is similar to that of molecules for a given pressure.

1.2.1 Experimental Setup

The evolution of the filament number in the beam section was investigated over 45 m in the free atmosphere with the TERAMOBILE laser (Wille *et al.*, 2002), which produced at 800 nm either 130 fs pulses with an energy tunable from 10 to 100 mJ in an 8 mm diameter beam (FWHM), i.e. an intensity of 0.15 to 1.5 TW/cm^2, or 50 to 400 mJ, 180 fs pulses in a 30 mm beam, i.e. an intensity of 40 to 275 MW/cm^2. Both beams were emitted collimated, i.e. unfocused.

Beam profiles of individual pulses were recorded by a digital camera (NIKON D90, ZEISS macro f = 2/100 mm ZF.2 lens) through a long-pass 750 nm filter. Simultaneously, a pre-calibrated photodiode monitored the energy of each individual pulse in order to take into account the input energy fluctuations typically around 10 % related to the laser operation and assign the actual intensities to each recorded image.

Data were recorded at four distances, upstream, close to and downstream of the nonlinear focus, which was measured at 7 m and 20 m from the laser exit for the 8 mm and the 30 mm beam, respectively. Single-pulse beam profiles and pulse energies were recorded at each distance. Filaments were identified as bright disks of diameter between 0.2 and 0.5 mm corresponding to 12–30 pixels, using a circular Hough transform (MATLAB function *imfindcircle*). The resulting filaments number and individual positions were used to compute the filaments surface density, as well as the nearest neighbor distance in each condition. These results were then averaged over 40 energy bins. The error bars displayed in the following figures show the standard deviation evaluated from these statistics. To get rid of the fact that the filamenting region shifts towards shorter distances when the intensity is increased, the results presented for each intensity bin correspond to the region where the filament number was maximal.

1.2.2 Results and Discussion

As displayed in Figure 1.2, the beam-averaged filament density rises almost linearly with the beam-averaged incident intensity, until it saturates at a typical packing density of 12 cm^{-2} for intensities above approximately 0.4 TW/cm^2. These density saturation and sub-TW/cm^2 intensity values are in line with what was estimated by Henin *et al.* (2010), i.e. 10 cm^{-2} and 0.2 TW/cm^2.

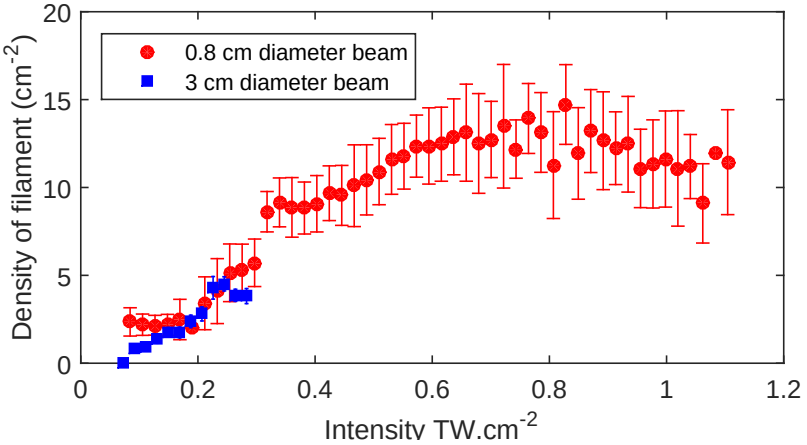

Figure 1.2: Experimental averaged filament density in the beam profile as a function of the averaged intensity, for the two beam geometries of the multi-terwatt near-infrared laser.

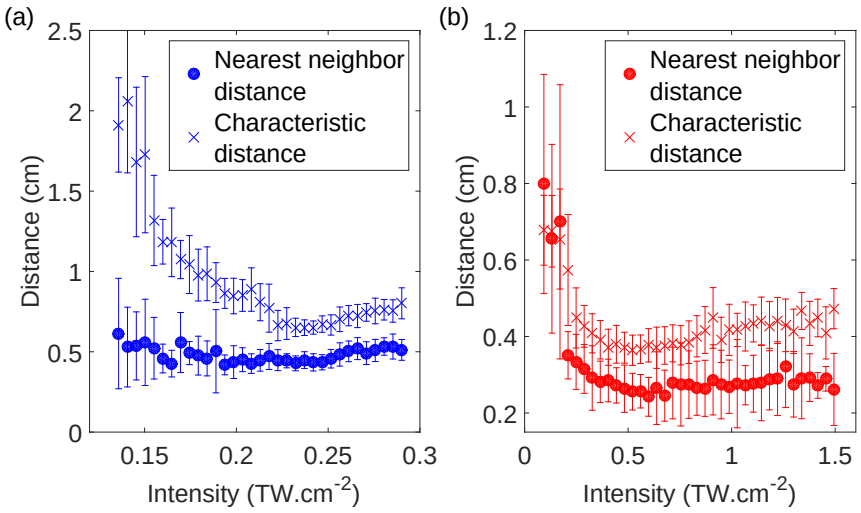

Figure 1.3: Mean nearest-neighbor distance and characteristic distance $d = 1/\sqrt{\sigma}$, where σ is the mean filament density as a function of the incident intensity, for the 3 cm (a) and 0.8 cm diameter beams (b).

The fact that the present experiment is performed at a hundred-times lower peak power and beam cross section than those of Henin *et al.* (2010) demonstrates the universality of the filament density saturation at high intensities, regardless of the influence of the beam boundaries.

This transition to the regime where the interaction between filaments dominates – solid-like phase – appears to imply a rich physics when comparing the present data with previous studies by Henin *et al.* (2010), Chin *et al.* (2002) and Stelmaszczyk *et al.* (2004), traditionally expressed in terms of number of critical powers per filament with $P_{cr} = 4$ GW. For intensities exceeding the 0.4 TW/cm^2 threshold for condensation, the number of critical powers per filament increases linearly with the incident intensity due to the saturation of the filament number. Conversely, below 0.06 TW/cm^2, various multifilamentation data from the literature such as those by Méjean *et al.* (2005), Skupin *et al.* (2004a), Méchain *et al.* (2005) and Béjot *et al.* (2007) fit to the value of 5 P_{cr} per filament, typical of the power-limited regime – gas-like phase (Henin *et al.*, 2010). Between these two phases, a new mixed phase state is identified where both gas and solid coexist. In this regime, the number of critical power amounts to 10–20 P_{cr} per filament.

To better understand this mixed-phase, characterized by intensities lower than the phase transition threshold, the mean nearest-neighbor distance of the filaments was calculated for energy bins corresponding each to 40 single shot pictures of the beam. This average nearest-neighbor distance was compared with a characteristic inter-filament distance calculated as $d = 1/\sqrt{\sigma}$, where σ is the filaments surface density in the beam profile.

The transition from the gas phase to the solid phase is evidenced by the decrease of both the nearest-neighbor distance and the characteristic distance d (Figure 1.3). The nearest-neighbor distance decreases to a constant plateau at 2.7 mm when the incident beam intensity is above 0.4 TW/cm^2 (Figure 1.3b). This particular feature is also evidenced by looking at the arrangement of the filaments in the 8 mm beam in the Figure 1.4d–f. Below this threshold (Figure 1.3a), the characteristic distance is divided by a factor 3 over the intensity range while the nearest-neighbor distance decreases only by 50 %. This means that filaments are not randomly distributed but rather packed into clusters where they strongly interact among each other. This explains the early saturation regime observed for $0.06\,\mathrm{TW/cm^2} < I < 0.4\,\mathrm{TW/cm^2}$. A further increase of

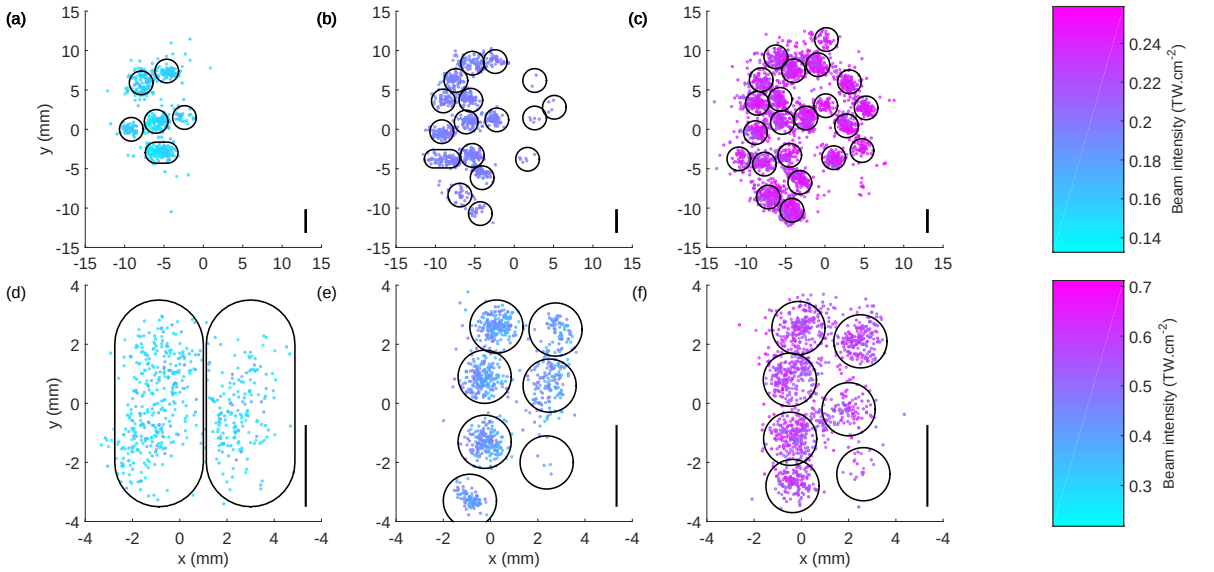

Figure 1.4: Superposition of the filaments detected over 200 single-shot images for the 3 cm beam (a−c) and the 8 mm beam (d−f) displayed in three classes of average incident beam intensities for clarity; Each pattern of filaments corresponding to the same incident beam intensity is displayed with the same color and the corresponding average beam intensity is indicated in the colorbar. The local intensity in each filament is about 50 TW/cm^2. The wandering region of each individual filament is marked as a black circle. The black vertical bar at the bottom right of each panel indicates the average inter-filament length of 2.7 mm.

intensity (Figure 1.4a−c) leads to the growth of the existing clusters as well as the nucleation of new ones until the whole beam is saturated. In other words, the local inhomogeneities in the beam profile act as seeds for local nucleation or deposition of the solid phase. This leads to the mixed-phase regime described above.

The formation of filamenting clusters that progressively spread over the beam can be directly observed on the patterns in Figure 1.4. Filaments first appear in regions where the local intensity is the highest. These islands then progressively grow towards less dense regions as the beam-averaged intensity increases, instead of increasing their local filament density. This behavior is observed for both 30 mm and 8 mm diameter beams, with the same nearest-neighbor distance of 2.7 mm inside the clusters (Figure 1.4). The intensities reached in the 8 mm beam lead to a stable crystal-like pattern formation that expands to the whole beam cross-section (Figure 1.4d−f).

This distance corresponds to a density of 13.7 cm^{-2} for a square lattice and 15.8 cm^{-2} for a close-packed (honeycomb) lattice, slightly above the beam-averaged space-limited density of 10 cm^{-2} previously reported by Henin *et al.* (2010). As the nearest-neighbor distance is representative of the equilibrium distance of the filaments interaction, the fixed value of the former, which corresponds to the plateau in Figure 1.3b, indicates that filaments form a solid with a characteristic Wigner-Seitz constant of 2.7 mm. The statistical analysis of the pictures also provides access to the pulse to pulse wandering of each individual filament and thus an analogy of a temperature linked to the intensity fluctuations in the beam profile. For filaments in the gas phase ($I < 0.06\,\mathrm{TW/cm^2}$) the variance on the position amounts to $0.20-0.22\,\mathrm{cm^{-2}}$, while for filaments in the solid phase ($I > 0.4\,\mathrm{TW/cm^2}$), the variance drastically decreases to $0.06-0.07\,\mathrm{cm^{-2}}$, in agreement with a stronger binding potential between the filaments.

The presence of the solid-like interaction between filaments can be modeled by considering the Hamiltonian associated to the two-dimensional nonlinear Schrödinger equation that describes the beam propagation. The normalized version is considered here

$$i\partial_\eta \psi + \Delta\psi + f(|\psi|^2)\psi = 0 \tag{1.12}$$

where ψ is the complex amplitude of the electric field, η is the normalised propagation coordinate, Δ the transverse Laplacian which accounts for geometrical diffraction, and the function f describes the nonlinear mechanisms at play.

Notice that the focus is put here on the interaction between already established filaments propagating in a stabilized regime, not on their formation during the self-focusing, pre-collapse, phase. One can consider in the f function the Kerr effect and the defocusing due to plasma created by ionization with K photons

$$f(|\psi|^2) = |\psi|^2 - |\psi|^{2K} \tag{1.13}$$

The Hamiltonian associated to this equation is $H = \int \mathcal{H} dr$ with

$$\mathcal{H} = -\frac{|\psi|^4}{2} + |\nabla\psi|^2 + \frac{|\psi|^{2(K+1)}}{K+1} \tag{1.14}$$

Following the pioneering work from Bergé *et al.* (1997), the interaction between two filaments can be studied by considering ψ as the superposition of two localized Gaussian beamlets

$$\psi(r, \delta, \theta, N) = \sqrt{\frac{N}{\pi\rho^2}} \left[\exp\left(\frac{-r^2}{2\rho^2}\right) + \exp\left(\frac{-(r-\delta)^2}{2\rho^2} + i\theta\right) \right] \tag{1.15}$$

where δ is the distance between the beamlets and θ their relative phase. For the sake of simplicity, both beamlets have the same power N and radius ρ. For a filament diameter of 150 µm, the maximum intensity in the beamlet corresponding to one critical power – so $P = P_{cr}$, $N = 4\pi$ here (Bergé *et al.*, 1997) and 4 GW at 800 nm – is 5.6 TW/cm^2. The interaction Hamiltonian can then be calculated numerically using the *chebfun* library from MATLAB (Driscoll *et al.*, 2014)

$$H_{\text{int}}(\delta, \theta, N) = H(\delta, \theta, N) - H(\infty, \theta, N) \tag{1.16}$$

Figure 1.5 displays the calculated Hamiltonian as a function of both δ and θ, for a moderate power $P = 0.2P_{\text{cr}}$ corresponding to 1.12 TW/cm^2 maximum intensity. The curve exhibits a saddle shape, with a turning point for $\theta = \pi/2$ and $\delta \simeq 1.5\rho$. One side of the saddle ($\theta > \pi/2$) leads to merging the two filaments (i.e. H_{int} is minimal when $\delta = 0$), while the other part ($\theta < \pi/2$) leads to a "Morse-like" potential with an equilibrium distance $\delta_{\text{eq}} > 0$. The analogy with a diatomic molecule is quite remarkable. The overall shape of this curve is kept when increasing the power although the amplitudes of the negative and positive peaks for $\delta = 0$ become orders of magnitude larger than the peaks for $\delta > 0$. The bonding potential observed for $\theta < \pi/2$ is the result of the attractive part due to the Kerr effect as filaments in phase tend to merge because of self-focusing and the repulsive effect of the plasma as reducing the inter-filament distance creates more plasma that repels the filaments away from each other. If one considers as Jhajj *et al.* (2016) that formed and coexisting filaments are in phase, Figure 1.6c and d show that δ_{eq} increases with the power and tends to converge to $\delta = 9\rho$, that is 1.35 mm for $\rho = 150\mu$m. This value, although a factor 2 smaller than the observed one (2.7 mm) is still comparable, especially considering that

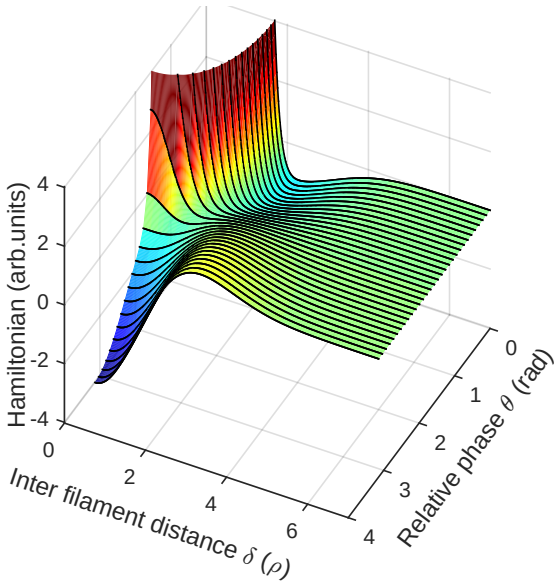

Figure 1.5: Interaction potential between two filaments of power $P = 0.2P_{cr}$ as a function of the inter-filament distance δ and their relative phase θ.

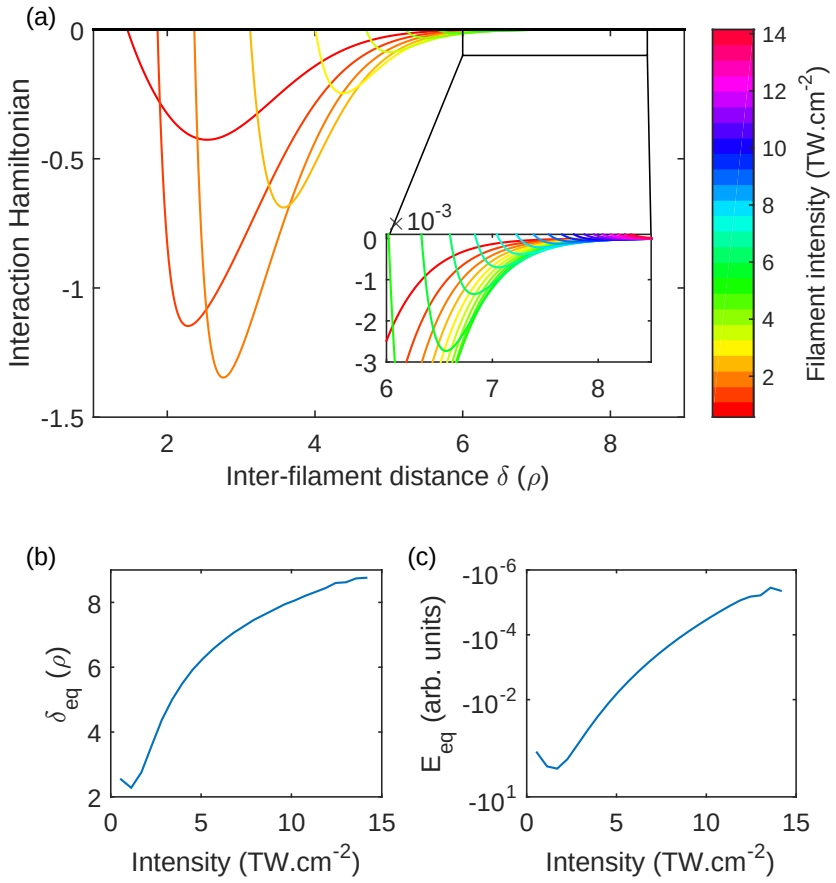

Figure 1.6: Interaction Hamiltonian for $0 < P < 2.5P_{\mathrm{cr}}$ and $\theta = 0$ function of the inter-filament distance δ (a). Evolution of the equilibrium distance (b) of the curves displayed in (a). Hamiltonian value at the equilibrium distance as a function of power (c).

the interaction was calculated between only two filaments, like the bond length in a diatomic molecule, and not in a 2D lattice. Clearly, the equilibrium distance will increase in this latter case, regarding that a factor 1.5 is typical between the equilibrium distance in a dimer and the lattice constant in the equivalent solid. The energy gained by forming a solid-like structure reduces when the power increases (Figure 1.6), because of the dominant repulsive effect of the plasma.

Although the values of the transition thresholds and of the inter-filament distances are specific to near-infrared pulses propagating at atmospheric pressure, the phenomenon itself, i.e. the transition between different phases of filamentation, and its description are valid for a wide range of mutlifilamentation processes in the sense that it requires only the competition of self-focusing and self-defocusing effects.

It should be noted that although the present model is able to qualitatively explain the essence of the observed phenomenons, modeling filaments with a Gaussian shape and a uniform phase is a crude model. Further modeling should include realistic intensity flux (Faccio *et al.*, 2006, 2009) and intensity shapes (Kolesik *et al.*, 2004), and advanced phase profile such as the recently studied spatio-temporal optical vortices (Jhajj *et al.*, 2016). Such features will expectedly improve the description of inter-filament interactions.

1.2.3 Conclusion

The transition between a multiple filamentation regime with weak inter-filament interaction (gas-like) to a regime with strong inter-filament interaction (solid-like) was investigated. This transition is independent of the beam diameter, but can be realized by changing the local beam intensity, which plays the role of pressure in this analogy. A mixed phase state occurring for intensities between 0.06 TW/cm^2 and 0.4 TW/cm^2 was evidenced for a near-infrared beam, in which filaments are closely packed in localized clusters. Those clusters are probably nucleated on inhomogeneities in the transverse intensity profile of the beam. The density in the clusters is almost constant, while the remaining of the beam, initially void of filaments, progressively fills up as the clusters spread over the whole profile when the incident intensity is increased.

These findings are confirmed by considering and calculating the interaction Hamiltonian between two filaments, taking into account the effect of diffraction, Kerr effect and plasma. This simple model suggests that filaments interact with an effective potential which shares fundamental characteristics with an atomic model. The shape of the potential is the result of the counteracting actions of the short-range repulsion of the plasma defocusing and the longer-range attraction of the Kerr effect focusing. The resulting bond length, or equilibrium distance, is a signature of this trade-off. Similarly, the potential curve is dependent on the relative phase between the two interacting filaments. This behavior reminds a diatomic molecular orbital formed by linearly superposing the two orbitals of the individual atoms in the orbital approximation. The relative phase between the two orbitals of the individual atoms determines indeed whether the molecular state will be bonding or anti-bonding.

Now that the general physics of laser filamentation has been discussed, the propagation of laser filaments in the atmosphere, and especially in turbulent atmosphere and cloudy conditions will be discussed in the next chapter.

Kilohertz Laser Filaments in Adverse Atmospheric Conditions 2

In order to use laser filaments for atmospheric purposes, efficient transmission of the beam through the atmosphere is essential and clouds and fogs constitute obvious obstacles. A high atmospheric humidity can lead to the presence of water droplets in air which will induce losses during the beam propagation. Another obvious difference between a controlled laboratory atmosphere and outside atmospheric conditions is the presence of turbulence. With turbulence, refractive index changes will happen on the beam propagation path, impending the beam pointing stability and beam profile.

The interactions of both turbulence and clouds with laser filaments have already been investigated at low repetition rates. Ackermann *et al.* (2006) and Salamé *et al.* (2007) reported that the Kerr effect in the laser filament itself creates transient refractive index gradients at least one order of magnitude larger than the random fluctuations induced by external turbulence. They reported that this holds even if the turbulence is much stronger than actual atmospheric perturbations, allowing the filaments to survive the propagation through extremely turbulent regions. On the other hand, laser filament propagation through clouds or fog has been demonstrated experimentally and numerically by Méjean *et al.* (2005) and others with ultrashort laser pulses and by Kwok *et al.* (1988) and Pustovalov & Khorunzhii (1992) with high energy CO_2 lasers up to 650 mJ per pulse.

In this chapter, a study of the repetition rate impact on filament propagation through adverse atmospheric conditions will be discussed. Section 2.1 focuses on the impact of turbulence created by a local heat source on the filaments propagation at 1 Hz to 1 kHz repetition rates and for two different average power regimes (1 mW to 100 W) as discussed in Schubert *et al.* (2016b). Section 2.2 presents results published in de la Cruz *et al.* (2016) indicating that for kHz repetition rates, a clear increase in light transmission occurs compared to repetition rates of 100 Hz or lower.

I personally contributed to the work presented in this chapter by designing the setup, collecting the data and supervising a master student who processed the data. The experiments were done in collaboration with TRUMPF Scientific Lasers in Munich (DE). This chapter is strongly inspired by the two articles published on these experiments (Schubert *et al.*, 2016b, de la Cruz *et al.*, 2016).

2.1 Dual-scale Turbulence in High Average Power Laser Filaments

Recently, thermal refractive index changes up to 20 % have been reported by Jhajj *et al.* (2014) in the trail of laser filaments at repetition rates up to the kHz range, featuring sufficient average power to heat the air. Cheng *et al.* (2013) and Lahav *et al.* (2014) showed that at this repetition rate, the resulting air density depletion can partially persist until the next laser pulse, resulting in a cumulative effect. In turn, these thermal effects can induce a beam wandering as presented by Yang *et al.* (2015).

Conversely, Lahav *et al.* (2014) and Rosenthal *et al.* (2014) demonstrated that the channel of depleted air density left behind the filaments can also self-guide subsequent pulses or be used in a filament array to stabilize and guide a laser beam. One could therefore expect that more intense beams would self-stabilize and even overcome the effect of externally imposed turbulence, with an increasing stability for increased incident average powers and repetition rates.

This section will address this question by investigating the beam pointing stability of high-repetition rate laser filamenting beams over a wide range of average powers (1 mW to 100 W), with and without externally imposed atmospheric turbulence.

2.1.1 Atmospheric Turbulence

Before going into the details of the experiments, a short reminder of atmospheric turbulence properties is required. On small scales, the atmosphere can be seen as being an incompressible fluid of density ρ which depends on temperature, humidity and pressure. Turbulence will then result in variations of these parameters and irregularities in the flow velocity in the spatial and temporal domains. The equation of continuity for such a fluid is

$$\vec{\nabla}\vec{u} = 0 \tag{2.1}$$

where $\vec{u}$ is the velocity vector of the turbulent motion. If the turbulent region is considered homogeneous, the density ρ and therefore the viscosity ν of the turbulent region are uniform. The variation of $\vec{u}$ in space and time is given by

$$\frac{\partial \vec{u}}{\partial t} + \vec{u} \cdot \vec{\nabla}\vec{u} = -\frac{1}{\rho}\vec{\nabla}P + \nu\nabla^2\vec{u} \tag{2.2}$$

where P is the pressure (Batchelor, 1982). The refractive index along the beam propagation path is therefore directly dependent to the density of each turbulent parcel and the changes in refractive index depend on the motion of each parcel in time and space.

Turbulence requires a continuous energy input as this process is highly dissipative due to the formation of eddies at different scales in the atmosphere. At large scales in the meter range, also called outer scales L_0, the kinetic energy injected by friction or convection generates and maintains the turbulence. This energy is given back to the system by heat dissipation at the end of a cascading chain on much smaller scales, also called inner scales l_0 which are in the millimeter range.

A *structure parameter of the refractive index*, C_n^2, can be defined through this concept of energy cascade as proposed by Kolmogorov (1941a,b) to quantify atmospheric turbulence. This parameter characterizes the correlation loss of the refractive index at increasing distances. It can

be calculated experimentally by measuring the pointing stability of a laser beam propagating through the turbulent region and it is given by the formula

$$C_n^2 = \sigma_\theta^2 \frac{\phi^{1/3}}{2.91 \cdot L} \tag{2.3}$$

where σ_θ^2 is the standard deviation on the beam pointing, ϕ is the beam diameter at $1/e$ of the intensity profile and L is the propagation length within turbulence. Atmospheric turbulence is comprised in the range $10^{-15} < C_n^2 < 10^{-13}$ m$^{-2/3}$ (Bendersky *et al.*, 2004).

2.1.2 Experimental Setup

As sketched in Figure 2.1, the experiment consisted in propagating the beam of an ultrashort laser beam through a turbulent hot air column generated by locally heating the air with an electric resistor. The electric resistor used in this experiment was a one-slit toaster and the laser beam was sent 3.5 cm above the 26 × 3 cm wide slit. The turbulence of the hot air column was measured by propagating a low power continuous wave (CW) He:Ne laser on the same path as the main laser and measuring its beam pointing stability on a screen. A THORLABS FGB37S filter was used to record the He:Ne image on the screen.

The standard deviation σ_θ^2 on the beam position was calculated and the C_n^2 parameter was estimated through Equation (2.3) to be $1.5 \cdot 10^{-8}$ m$^{-2/3}$ with the resistor on and $1.7 \cdot 10^{-11}$ m$^{-2/3}$ without it.

Two different laser systems were used to compare the average power impact on the propagation through turbulence. The first one, hereafter denoted the moderate-power beam, is a Ti:Sa laser from COHERENT delivering 82 fs pulses with an energy of 3 mJ at a wavelength of 800 nm. Its repetition rate was varied between 1 Hz and 1 kHz, corresponding to average powers of 1 mW to 1 W. The 13 mm initial beam diameter (at $1/e$) was slightly focused with an $f = 2$ m lens, 3.5 cm above the electric resistor. It produced a 16 cm long filament at the waist, where the beam diameter was 0.4 mm. The turbulent region was placed at the most intense part of the filament, defined as the position where the plasma acoustic noise was the loudest. After a further 2.5 m, the beam was imaged on an aluminium oxide screen. Approximately 3000 single shot images were recorded for each repetition rate with a PHANTOM high speed camera (600 × 800 pixels) through an OD4 optical density and a long-pass 750 nm filters.

The second system, hereafter denoted the high-power beam and represented in Figure 2.1, was developed by Klingebiel *et al.* (2015) at TRUMPF SCIENTIFIC LASERS. It is an Yb:YAG DIRA

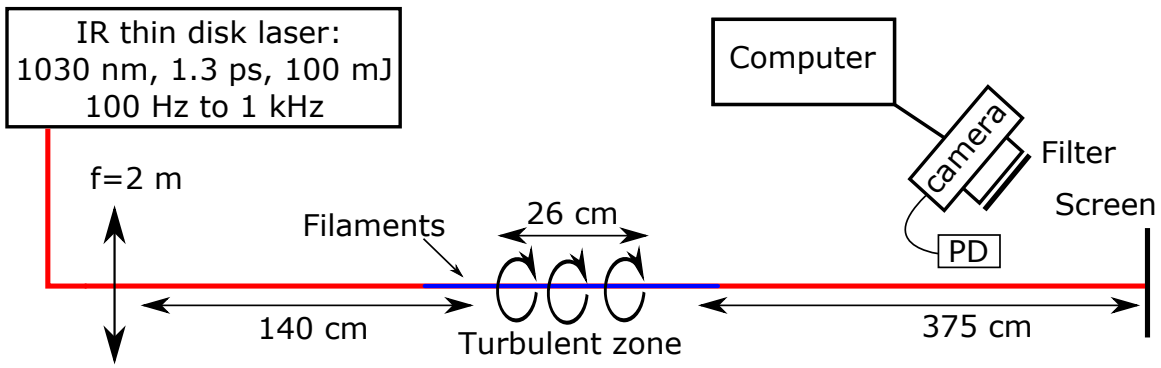

Figure 2.1: Experimental setup. Values correspond to the high-power beam.

thin disk laser, it delivers 100 mJ, 1.3 ps pulses at 1030 nm and generates typically three to four 50 cm long filaments. The repetition rate was varied between 100 and 1000 Hz, corresponding to average powers of 10 to 100 W. The use of pulses longer than those of the moderate-power system allows to reach much higher average powers for similar peak powers, hence similar levels of nonlinearity. The geometrical configuration was identical to that of the moderate power beam, except for an initial beam diameter of 12 mm and the propagation distance between the turbulent region and the aluminium oxide screen, namely 3.75 m. In this experimental condition, approximately 1900 single shot images were recorded at 50 ms time interval using a PIXELINK PL-B761U CCD camera with 480×752 pixels through a SCHOTT BG7 filter.

Considering that filaments at 800 nm are usually defined with a 100 µm diameter and a 50 TW/cm^2 peak intensity, an energy of 5 mJ/filament was calculated for the 1030 nm in a first approximation. Houard *et al.* (2016) recently measured 1030 nm laser filaments peak intensities of 25 TW/cm^2. Therefore, considering that the diameter of 4 µm filaments is in the 600–800 µm range Mongin *et al.* (2016b) and that no filament diameter value was found in the literature for 1030 nm, an arbitrary diameter of 100 to 200 µm will fit both the peak power measurements from Houard *et al.* (2016) and the filament energy calculated at 800 nm and stay in a reasonable range. This implies the assumption that the 20 % increase in wavelength will not affect too much the energy in the filament.

For the data processing in both cases, each image was thresholded at 10 % of the maximum intensity to isolate the beam from the background and the beam position was defined as being the center of mass of this area. The position of the filament in the moderate-power beam was determined using a higher threshold, at 87 % of the maximum intensity.

Two parameters characterize the beam wandering. The magnitude of movement is defined as the two-dimensional standard deviation σ_θ of the pointing direction and its instantaneous speed v_w is defined as the displacement of the beam position between two successive images divided by the corresponding time interval. As the phase mask induced in the air by turbulence evolves slowly as compared to the beam repetition rate, the beam wandering speed can be accurately resolved. As a consequence, if the time interval between the laser pulses is sufficiently short, their successive positions on the screen will display some correlation. The corresponding time constant has been determined by calculating the autocorrelation function of these positions and the corresponding correlation time was defined as the decay time (at $1/e$) of this beam position autocorrelation function.

The deviation of the beam profile from its initial circular shape was finally quantified by calculating the two-dimensional second moment of the thresholded image.

2.1.3 Results

The 1 mJ pulse energy of the moderate-power laser ensures that the beam constantly produces one single filament strong enough to survive the propagation through the turbulent region. Without external turbulence, the wandering of the filament increases with the repetition rate or consequently the average power (Figure 2.2a) because the filament deposits energy in the air and induces direct turbulence as reported by Lahav *et al.* (2014), Cheng *et al.* (2013) and Yang *et al.* (2015). Accordingly, the standard deviation of the filament pointing rises from 50 µrad at 10 Hz to 310 µrad at 1 kHz. The self-induced turbulence extends beyond the filament itself: it increases the wandering of the whole beam, although to a lesser extent ($\sigma_\theta = 210$ µrad at 1 kHz).

When imposing an external turbulence, both the filament and the whole beam are randomly

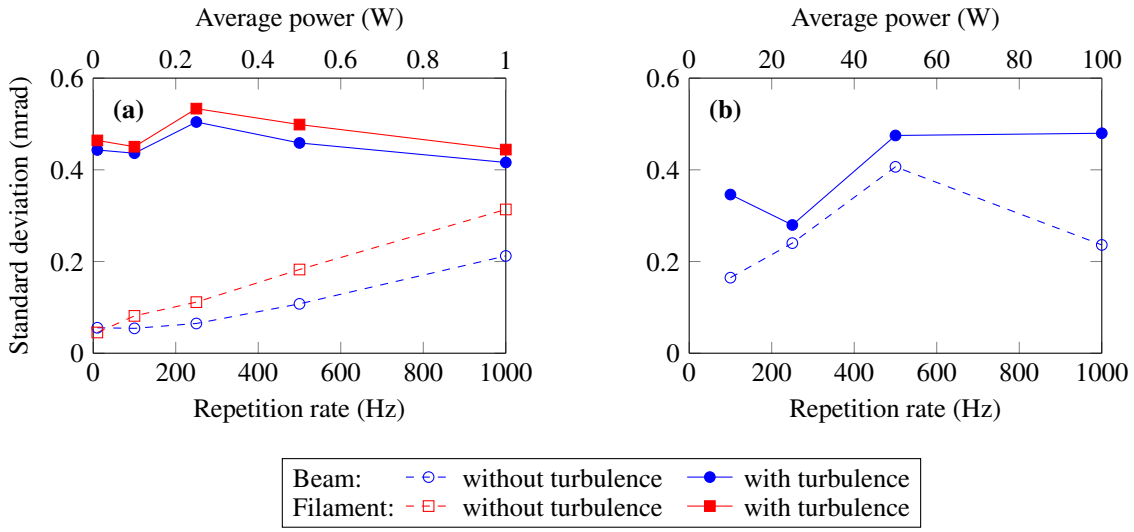

Figure 2.2: Wandering of the single filament and of the whole moderate-power (a) and high-power (b) beams propagating through a turbulent region.

deflected, which further increases their wandering. The standard deviation rises to approximately 450 µrad independently from the repetition rate. This shows that the effects of the self-induced turbulence do not influence those of the externally-imposed one, that dominates the beam propagation when present. As a consequence, neither self-stabilization, nor self-destabilization are observed.

Surprisingly, in a 100 times higher power range, the self-induced turbulence is only slightly stronger. This can be understood by considering that the energy deposition is much less efficient with the high-power laser system. Indeed, Houard *et al.* (2016) measured the energy losses for laser pulses identical (respectively similar) to those produced by the high-power (respectively moderate-power) system. These losses are ten times lower (2 % *vs.* 20 %) for 1030 nm, 1.5 ps pulses than for 800 nm, 100 fs pulses. Furthermore, the formation of a multiple filament pattern may also result in a more homogeneous energy deposition over a wider volume, limiting the associated refractive index gradients. The increase of the beam wandering in externally-imposed turbulence is also influenced by the strong intrinsic dependence of the laser pointing stability. Without external turbulence, the beam pointing stability of the high-power laser system itself is optimized for operation at 1 kHz repetition rate. At intermediate repetition rates (500 Hz), the thermal lensing or other processes inside the amplifiers degrade the pointing stability.

With the externally imposed turbulence, the beam wandering is larger and the angular standard deviation ranges from 350 to 480 µrad (Figure 2.2b). Furthermore, this wandering does not seem to depend on the repetition rate: no beam self-stabilization occurs when the repetition rate increases, even at the 100 W average power level.

The fact that the self-induced thermal effects do not affect the wandering through the externally induced turbulence can be understood by observing their respective influences on the beam trajectory on the screen, displayed on Figure 2.3. Without externally imposed turbulence, i.e. under the control of the self-induced turbulence, the beam stays confined for typically 0.5 s within a cluster of approximately 100 µrad. Between these confinement times, it experiences rare long-distance (sub-milliradian) jumps to a new cluster position (Figure 2.3a). Accordingly, the beam pointing displays correlation times up to 110 pulses corresponding to 0.1 s at 1 kHz.

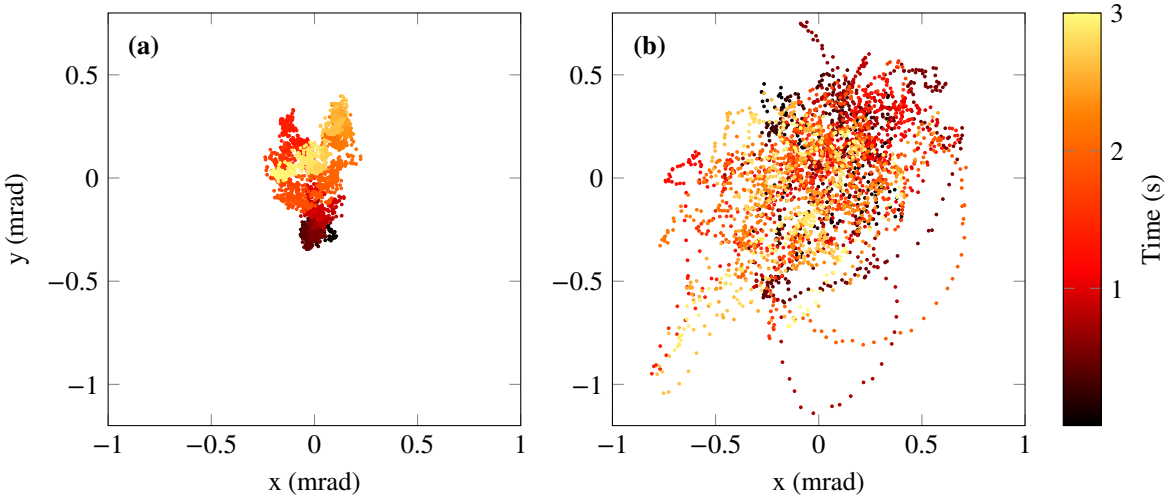

Figure 2.3: Trajectory of the moderate-power beam pointing at a repetition rate of 1 kHz, without (a) and with (b) externally imposed turbulence.

As the jumps between clusters are larger than the typical cluster size, they govern the overall magnitude of the beam wandering. The increase of the beam wandering for higher repetition rates is therefore the signature of longer jumps. However, these jumps are sufficiently rare to have a negligible influence on the average wandering speed (dotted lines in Figure 2.4), which is more representative of the beam motion within the clusters.

Externally imposed turbulence substantially increases the shot-to-shot wandering of the beam within the clusters, so that they grow in size and widely overlap each other (Figure 2.3b). Consequently, both the speed (solid lines in Figure 2.4) and the magnitude of the wandering (Figure 2.2a and Figure 2.2b) are governed by the size of the clusters and keep independent of the jumps between them, hence of the self-induced turbulence.

In summary, the external turbulence governs the shot-to-shot motion of the beam within the clusters, while the self-induced one is responsible for the jumps from cluster to cluster at a much longer time scale of 0.5 s. This behavior is observed not only for the whole beam, but also for the individual filaments. In the latter case, the wandering speed is slightly higher, by approximately 1 mrad/s. This longer time scale of the self-induced turbulence is attributed to smoother and wider refractive index gradients produced by the local convection. The vorticity of the externally imposed turbulence on the contrary has more space to develop during the transport of the corresponding air mass to the laser beam location.

This dual time scale may explain the apparent discrepancy of these results with those of Yang *et al.* (2015), who measured a structure parameter for the refractive index C_n^2 typically two orders of magnitude smaller than in this work: $C_n^2 \approx 5 \cdot 10^{-9}\,\mathrm{m}^{-2/3}$ for 2 mJ, 45 fs pulses, comparable to our moderate-power system. As they measured the fluctuation of the beam position over only 20 pulses (i.e. 20 ms), they focus on the short scale wandering within a cluster, in other words on the effect of the residual external turbulence in the laboratory. Several seconds (3000 pulses in this work's setup correspond to three seconds) are on the other hand necessary to get access to the full excursion of the beam pointing controlled by the self-induced turbulence.

Finally, neither the self-induced nor the externally imposed turbulences significantly affect the beam shape or the filaments. The beam profile, characterized as described above by its two-dimensional second moment, is almost unchanged by both turbulence sources. This is presumably

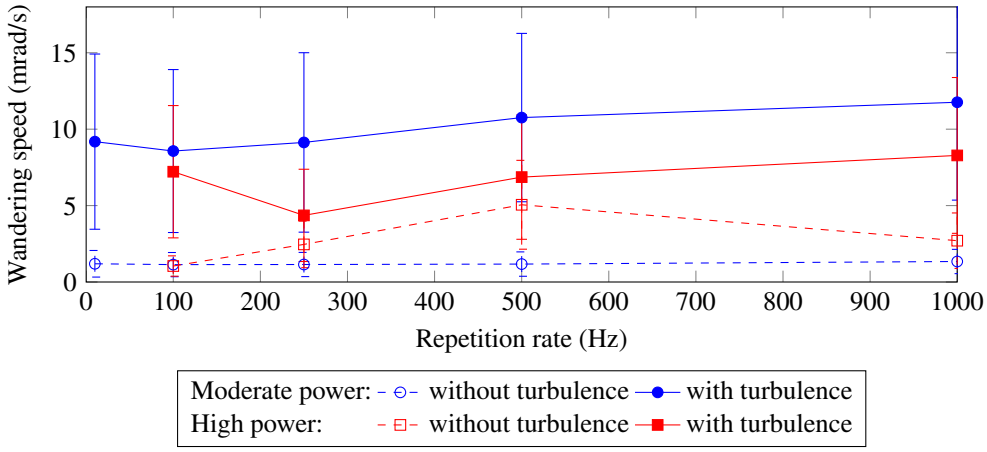

Figure 2.4: Instantaneous wandering speed of the laser beam

due to the fact that the beam diameter does not exceed the inner scale of the turbulence ($l_0 \sim 1$ mm as shown by Meyzonnette & Lépine (2001)), so the refractive index gradient is homogeneous over the beam profile.

The filament formation process is also unaffected by the turbulence. At moderate power, the filament and the full beam display very similar trajectories (Figure 2.2a). Indeed, the correlation coefficient between their positions ranges between 0.96 and 0.98 at all investigated repetition rates. This correlation was not studied in the case of the high-average power laser as the multiple filament pattern strongly complicated the study of individual filaments in the data analysis. However, it can be noted that at full power on the high-average power system which corresponds to 100 mJ, 100 W average power, 76 GW peak power, i.e. approximately $15\,P_{cr}$, 80 to 100 % of the filaments survive the propagation through the turbulent region. This survival probability does not depend significantly on the repetition rate and such robustness is consistent with prior results at lower repetition rate and average power such as 22.5 Hz, 14 mW demonstrated by Ackermann *et al.* (2006).

2.1.4 Conclusion

As a conclusion, the respective contributions of externally-imposed and self-generated turbulence on high repetition rate, ultrashort-pulse lasers with average powers ranging from 1 mW up to 100 W were investigated. Externally-imposed and self-induced turbulences display very different time constants, in the millisecond and sub-second respectively.

Furthermore, the self-induced thermal contributions do not affect the externally-imposed turbulence contribution and no beam self-stabilization is therefore induced in the investigated power range. However, the long time scale of the self-induced turbulence at high repetition rates may facilitate its compensation using adaptive closed-loop techniques, potentially helping propagating high-power, high repetition rate pulses through perturbed atmospheres.

In the next section, the presence of water droplets in the atmosphere and its impact on the laser beam propagation will be discussed.

2.2 High Repetition Rate Ultrashort Laser Drills a Path through Fog

In the previous section, the consequences of refractive index changes in air due to turbulence on laser filaments propagation has been discussed. This section will focus on the impact of particles such as water droplets in the beam path.

As explained in Chapter 1, laser filaments are surrounded by a photon bath carrying most of the beam energy. Courvoisier *et al.* (2003), Kolesik & Moloney (2004) and Skupin *et al.* (2004b) showed that this bath is able to reconstruct filaments after they have been blocked by an obstacle like a water drop. However, the bath propagates in an approximately linear regime because of its low intensity. It undergoes therefore elastic scattering and the aerosols ultimately limit the filamentation length as a filament cannot propagate without being fed by its photon bath (Liu *et al.*, 2005).

Vidal *et al.* (2000), Jhajj *et al.* (2014) and Lahav *et al.* (2014) showed that laser filaments leave behind them a cylindric region where the air density is depleted with a lifetime of hundreds of microseconds. In this chapter, it is demonstrated that the associated shock wave could help clearing up the atmosphere not only in the filament, but also in a significant fraction of the photon bath. Indeed, the energy of such a shock wave can expel particles out of the beam at a very low energy cost.

This approach substantially differs from earlier attempts to clear clouds and fogs with lasers. Zuev *et al.* (1984) reviewed the use in the 70's and '80s of 10 kW/cm^2 CW lasers and Kwok *et al.* (1988) and Pustovalov & Khorunzhii (1992) used 1 to 1000 MW/cm^2 pulsed lasers to obtain similar results. However, prohibitively high intensities and energies are needed to evaporate and shatter water drops with these high energy CO_2 lasers.

Here, near-infrared ultrashort (ps) laser pulses are sent through a dense fog and it is demonstrated that the transmission increases with the repetition rate, i.e. with the average beam power. Indeed, the above-mentioned shock wave expels the particles from the beam central region well beyond the filament volume itself.

2.2.1 Interactions of Atmospheric Particles with Light

Although this chapter presents results of beam propagation through clouds, the cloud structure will not be discussed here. A very complete book on the topic was written by Pruppacher & Klett (1978) for interested readers. Here, clouds will be considered to be a random distribution of approximately spherical water droplets. Therefore, the only processes that will be important to this work are the interactions between these droplets and the laser beam.

The concept of extinction, absorption and scattering will be explained in the following. As the mathematical details of this theory are not needed to understand the work presented here, readers keen on learning more about this aspect are kindly redirected to Bohren & Huffman (1983) and Seinfeld & Pandis (2006) from which this theoretical introduction is extracted.

When a beam of light hits a particle, electric charges in the particle are excited into oscillatory motion. Some energy may be converted into thermal energy in an *absorbed* process and the rest is radiated out of the particle in all directions through *scattering*. If the beam is collected by a detector after impinging a particle, the power absorbed and scattered by a particle is proportional to the incident intensity I_0

$$P_{\text{ext}} = P_{\text{abs}} + P_{\text{sca}} = (\sigma_{\text{abs}} + \sigma_{\text{sca}})I_0 = \sigma_{\text{ext}} I_0 \tag{2.4}$$

where σ are the single particle absorption and scattering cross sections in units of area. P_{ext} is the extinction power of the beam and σ_{ext} is the single particle extinction cross section in units of area.

The total intensity loss is a combined effect of scattering and absorption and is referred to as *extinction* and the

It is convenient to define a dimensionless *efficiency*

$$Q_{\text{abs}} = \frac{\sigma_{\text{abs}}}{A} \qquad Q_{\text{sca}} = \frac{\sigma_{\text{sca}}}{A} \qquad Q_{\text{ext}} = \frac{\sigma_{\text{ext}}}{A} = Q_{\text{abs}} + Q_{\text{sca}} \tag{2.5}$$

where A is the geometrical cross section of the particle. In this work, particles are taken to be spherical and $A = \pi r^2$ for a particle of radius r.

Light scattering mechanisms of particles can be divided into three categories:

- *Elastic scattering* where the wavelength of the scattered light is the same as the incident wavelength.
- *Quasi-elastic scattering* where the wavelength shifts because of Doppler effects and diffusion broadening.
- *Inelastic scattering* where the emitted radiation has a wavelength different from that of the incident radiation.

Although nonlinear optics lead to inelastic and quasi-inelastic scattering, these processes are much less efficient than elastic scattering and only the later will be discussed in the following.

The key parameters that govern the scattering and absorption of light by a particle are the wavelength λ of the incident beam and the diameter D of the particle. These parameters are usually expressed as a dimensionless size parameter

$$\alpha = \frac{\pi D}{\lambda} \tag{2.6}$$

Scattering and absorption of light by a particle is a classical problem in Physics and the mathematical formalism behind it is called *Mie theory*. This theory is explained in detail in Bohren & Huffman (1983) and it can serve as the basis of a computational procedure to calculate the scattering and absorption of light by any sphere as a function of wavelength. Mie scattering theory can be simplified in certain limiting cases to provide insight into the physics of the problem.

Rayleigh scattering $\alpha \ll 1 \Rightarrow D \ll \lambda$: the particles are small compared to the wavelength (Bohren & Huffman, 1983, pp. 130–154). The definition Rayleigh gave in 1871 is still valid nowadays:

> *When light is scattered by particles which are very small compared with any of the wavelengths, the ratio of the amplitudes of the vibrations of the scattered and incident light varies as the square of the wavelength and the intensity of the lights themselves as the inverse fourth power.*
>
> Rayleigh (1871)

In short, this can be written as

$$Q_{\text{sca}} \propto \frac{1}{\lambda^4} \tag{2.7}$$

A typical example of this regime is given by the sky turning red at sunset because shorter wavelengths are scattered more efficiently. In the case of near-infrared to mid-infrared laser sources as those used in this work, particles in the order of the micron size and smaller are in this regime.

Mie scattering $\alpha \approx 1 \Rightarrow D \approx \lambda$: when the particle diameter is comparable to the wavelength, only Mie scattering holds (Bohren & Huffman, 1983, pp. 82–129). In this work, this means the particle diameters are around 800 to 1030 nm. A concrete example of Mie scattering is the visualization of a laser beam propagating through a cloudy or dusty atmosphere.

Diffraction $\alpha \gg 1 \Rightarrow D \gg \lambda$: the particles are much larger than the wavelength (Bohren & Huffman, 1983, pp. 166–180). In this case, light is reflected, refracted and diffracted and scattering strongly depends on the particle shape and orientation relative to the incoming beam. In the atmosphere, big water droplets larger than a few microns fall in this category. The halo around the moon through fog is a typical example of atmospheric diffraction.

As the droplet density on the beam propagation path is relatively small and as the light is collected far from the interaction region, the multiple scattering was not taken into account in this work.

Coming back to the extinction efficiency, if the particle considered is a large weakly absorbing sphere such as a water droplet, it can be shown that (Bohren & Huffman, 1983) Q_{ext} approaches the limiting value of 2 when the size parameter increases

$$\lim_{\alpha \to \infty} Q_{\text{ext}}(\alpha, m) = 2 \tag{2.8}$$

This is twice as large as predicted by geometrical optics. This is the so-called *extinction paradox*. In qualitative terms, the incident wave is influenced beyond the physical boundaries of the sphere: the edges of the sphere deflect rays in its neighborhood that would have passed unimpeded from the viewpoint of geometric optics (Seinfeld & Pandis, 2006).

In the frame of this work, a mid-infrared (1030 nm) laser was propagated through fog. At this wavelength, the atmosphere is very transparent although some weak absorption by H_2O and CO_2 is noticeable.

2.2.2 Experimental Setup

To investigate the propagation of a high repetition rate ultrashort laser beam through fog, the experimental setup sketched in Figure 2.5a was built. The laser source used for this experiment was already presented in Section 2.1.2 as the high average power laser and all the parameters are the same, including the slight focusing of $f = 2$ m before the chamber.

The beam was imaged on a screen 3.5 m after the fog chamber and the beam profile was recorded by a PIXELINK PL-B761U CCD camera with 480×752 pixels. Approximately 1900 single-shot images were recorded for each experimental condition through a SCHOTT BG7 filter blocking the 700 to 900 nm continuum spectral region but only attenuating the fundamental 1030 nm wavelength. The profile-integrated fluence on the screen normalized by the reference measurement without fog was used to calculate the energy transmission through the fog.

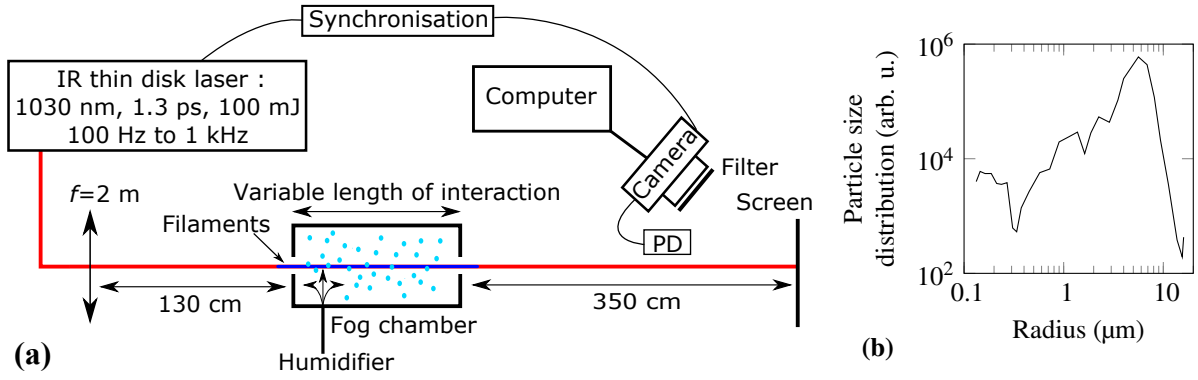

Figure 2.5: Experimental setup (a) and particle surface size distribution (b) measured by the GRIMM 1.109 in the fog chamber.

The fog was produced by a large volume droplet generator (humidifier) and introduced into a $40 \times 60 \times 30$ cm chamber, the laser propagating through the 40 cm box length. Leaks through the openings implied an interaction length of 50 cm between the laser beam and the fog. Alternatively, the fog at the exhaust of the generator was directly blown across the laser beam, reducing the propagation length to 6 cm. In either case, the fog interacted with the most intense longitudinal section of the filament, i.e. where the plasma noise was the strongest.

The fog droplet size distribution was measured by using an optical aerosol sizer GRIMM, model 1.109 (Figure 2.5b). The size distribution was homogeneous across the fog chamber and the typical droplet size was also measured with direct imaging of the particles impacted on a glass surface. Both methods render a size distribution mode of $a_{\text{eff}} = 5\,\mu$m compatible with typical fog conditions in the atmosphere. In order to reach optical densities encountered in fogs on the meter-scale of the laboratory, the droplet concentration was increased 100 times as compared to actual fogs.

2.2.3 Results

The beam transmission through fog as a function of the repetition rate is displayed on Figure 2.6. At the highest repetition rates corresponding to average powers up to 100 W, the transmission through fog is increased. At 100 Hz, only 0.1 % of light is transmitted through 50 cm fog whereas up to 32 % passes through at 1 kHz. Taking into account the estimate made before that the three filaments carry only 15 % of the beam energy, this implies that the laser transmission increases even in the photon bath where the intensity is lower than in the filaments. The increased transmission is indeed associated with a transmitted beam diameter growth as shown in Figure 2.7. While only the central part of the beam profile is partially transmitted at 100 Hz, this part covers almost the whole beam at 1 kHz. In other words, increasing the repetition rate – therefore the average power and the deposited heat – increases both the transmission in the beam center and the width of the region over which this transmission is increased. These observations cannot be explained by vaporization or shattering of the water droplets present in the filament volume. Such effect would not allow a transmission increase larger than the 15 % of the transmitted beam energy in the filaments, and the transmitted beam profile would be independent from the repetition rate. These results rather point towards the ejection of droplets out of the beam by the shock wave in the air associated to local heating as presented by Jhajj *et al.* (2014). This thermal contribution is

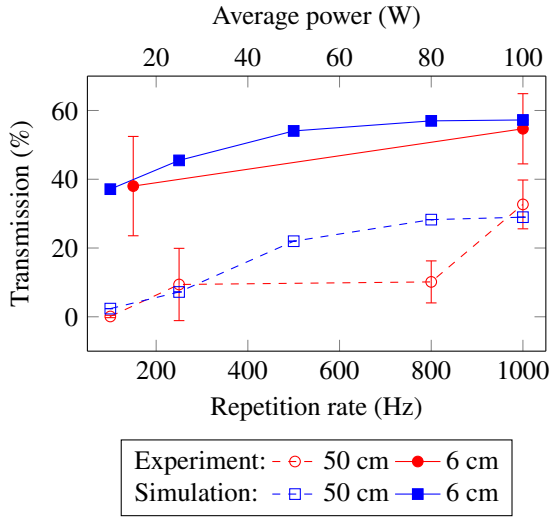

Figure 2.6: Beam transmission of 1030 nm, 100 mJ, 1.3 ps laser pulses through the fog chamber for different lengths of interaction and repetition rates.

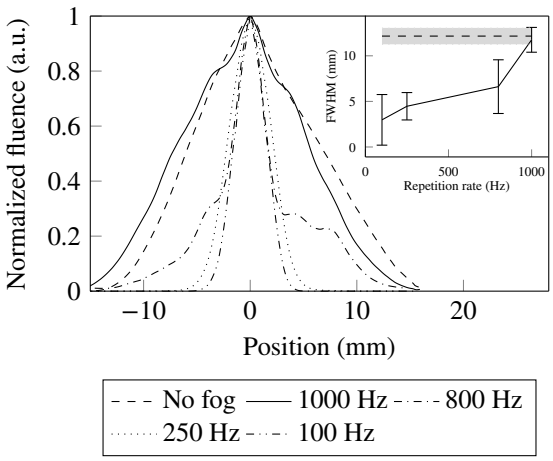

Figure 2.7: Typical fluence profile of the beam as a function of the repetition rate. Inset: FWHM of the profile as a function of the repetition rate.

related to the cumulative energy deposition by the filaments in the air demonstrated by Lahav *et al.* (2014) which is typically 2 % of the total energy at 1 kHz according to Houard *et al.* (2016).

The heat deposited by filaments in comparable conditions typically generates a depleted channel with a local pressure reduced to $P \approx 0.5$ atm as demonstrated by Vidal *et al.* (2000) and Jhajj *et al.* (2014). This implies that the air parcel doubles volume and it was therefore assumed that the shock wave swept a volume at least twice as large as that of the filaments, i.e., a cylinder of 140 µm diameter. Based on the temporal evolution of the air density calculated by Vidal *et al.* (2000), the radial expansion speed of air was assumed to be $v_{\text{air}} = 21$ m/s for $t = 0\text{–}1$ µs and the collapse speed $v_{\text{air}} = -10$ mm/s for $t = 10^{-4}\text{–}2 \cdot 10^{-3}$ s. Outside of these two time intervals, the air was considered to stay still. The equation of motion of an individual droplet under aerodynamic drag taken from Belkhelfa (2008) was solved assuming that the droplets kept their spherical shape

$$m_{\text{drop}} \cdot \frac{\mathrm{d}\vec{v}_{\text{drop}}}{\mathrm{d}t} = \frac{1}{2}\pi a^2 \rho_{\text{air}} C_d \left(\vec{v}_{\text{air}} - \vec{v}_{\text{drop}}\right)^2 \tag{2.9}$$

where m_{drop} and v_{drop} are respectively the mass and the speed of the droplet, ρ_{air} is the air density, v_{air} is the speed of the displaced air parcel and $C_d = 0.47$ is the drag coefficient for a sphere. The shock wave has therefore a net effect of ejecting the droplets at a speed $v_{\text{out}} = 60$ mm/s out of both the filament and its surrounding photon bath.

The balance between the particle ejection by the shock wave and the advection by the transverse wind can be characterized by calculating the net flux ϕ of particles through the outer surface of the region swept by the shock wave, modeled as a cylinder of length L and radius $R = 70$ µm

$$\phi_{\text{net}} = \frac{\mathrm{d}N(t)}{\mathrm{d}t} = n_{\text{drop}} v_{\text{in}} 2RL - \frac{2N(t)v_{\text{out}}}{R} \tag{2.10}$$

where $N(t)$ is the number of particles in the considered cylinder, t is the time and n_{drop} is the drop concentration supplied by the droplet generator far from the filament. The advection speed

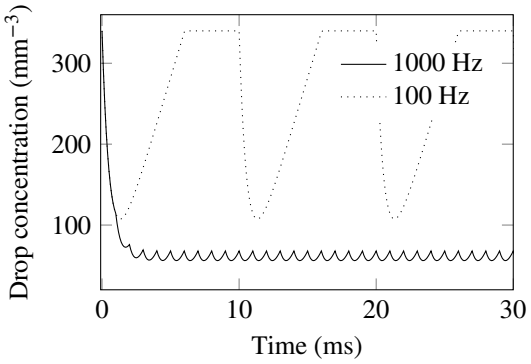

Figure 2.8: Evolution of the average drop concentration in the 70 µm cylinder swept by the shock wave.

v_{in} of the incoming droplets is estimated to be 12 mm/s based on the droplet generator flow and chamber geometry.

Figure 2.8 displays the droplet concentration evolution within the cylinder swept by the shock wave, based on the integration of Equation (2.10). At 100 Hz, the advection is fast enough to reach the initial droplet concentration between two pulses. In contrast, the droplet concentration decreases because the advection at 1 kHz is too slow as compared to the particle flow. After 3 to 5 pulses, the concentration reaches a steady regime in which advection and droplet expulsion by the shock wave balance each other. The droplet concentration has then dropped by almost a factor 6 from $3.4 \cdot 10^{10}$ to $6 \cdot 10^{9}$ m^{-3}. The concentration estimated by this approach is independent from the diameter of the considered cylinder because the drag force of the air is insufficient to slow the ejected particles down significantly over a few milliseconds. Their speed can therefore be considered constant at the investigated time scales.

The impact of the droplet ejection by the shock wave on the beam transmission was precisely estimated by modeling in two dimensions the interactions of droplets carried by an advection flow under the influence of the laser-generated shock wave. More specifically, Monte-Carlo simulations were performed by computing the trajectory of 40 000 droplets of radius $a_{eff} = 5$ µm with an initial advection speed $v_{in} = 12$ mm/s transverse to the laser beam. At each laser pulse, droplets located within the area swept by the shock wave associated with each of the three filament are ejected radially at a speed of 60 mm/s. The resulting droplet concentration map is then used to determine the local transmission, that is then integrated over the beam intensity profile to yield the beam transmission value.

Propagation lengths of both 50 cm and 6 cm have been considered to represent the experiments. In order to match the experimental parameters, the beam is modeled as a Gaussian beam with a FWHM diameter of 5 mm and three filaments are evenly positioned on a 0.7 mm radius circle around the beam center. The orientation of the triangle formed by the three filaments evolves randomly from shot to shot and the results are insensitive to the details of this motion.

When running the Monte-Carlo simulations, a droplet-depleted region appears downstream of the filamenting region. The corresponding transmission increase of the photon bath contributes to one half of the total observed beam transmission increase at high repetition rates. As shown in Figure 2.6, this model reproduces well the experimental results for an initial droplet concentration of 344 mm^{-3}. This demonstrates the key role of the shock wave in clearing the fog and increasing the laser beam transmission. Note that the discrepancy with the experimental point at 800 Hz is due to a lower laser beam stability at this repetition rate which limits the cumulative thermal effect. Although the size mode of actual fog is slightly lower ($\sim$1 µm), one can expect that these results can be extended at least to atmospheric ranges in a dense fog.

Due to the energy deposition in the air, a shock wave expels the fog droplets not only within the filament volume but also out of the photon bath. In consequence, a drastically improved beam transmission is observed above approximately 20 Hz repetition rate. This effect increases at higher repetition rates where the balance between the expulsion and the advection of new background droplets is broken and favors the clearing of the beam propagation path. This opens therefore new prospects to improved laser beam transmission through fog.

2.3 Conclusion

In this chapter, the advantages of high repetition rate laser for real-scale experiments have been demonstrated. Self-induced turbulence has been demonstrated to change on timescales of half a second and filaments have proven to survive propagation through atmosphere more turbulent than the outdoor atmosphere. The propagation through fog of a kilohertz repetition rate laser showed that high repetition rate filaments can clear the beam propagation path on a much larger scale than their individual position, leading to an increase in the full beam transmission. This can therefore lead to a longer propagation length of filaments in the real atmosphere as the photon bath around the filament is less attenuated.

In general, these results are very promising for kilohertz ultrashort pulses applications in field experiments such as LIDAR experiments or for lightning control.

Now that perspectives to improve the propagation through adverse climatic conditions have been demonstrated, the next chapter will focus on the chemical interactions between laser filaments at different wavelengths and the atmosphere.

Mid-Infrared Laser-Induced Condensation in Air 3

The previous chapter presented the impacts of real atmosphere on the filamentation process and transmission at different repetition rates. This chapter will present how high intensities in filaments can create new atmospheric aerosols and how the laser wavelength will influence the aerosol formation.

The high intensities reached in laser filaments allow nonlinear interactions of the photons with the air molecules such as multi-photon ionization and photo-dissociation of air molecules as shown by La Fontaine *et al.* (1999), Schwarz *et al.* (2000), Bergé *et al.* (2007), Couairon & Mysyrowicz (2007), Petit *et al.* (2010) and Saathoff *et al.* (2013). This changes the physico-chemical equilibrium of the atmosphere and leads to aerosol condensation such as demonstrated by Rohwetter *et al.* (2010), Henin *et al.* (2011), Kasparian *et al.* (2012) and Leisner *et al.* (2013). Other papers such as those by Sun *et al.* (2013) and Ju *et al.* (2014) also suggest that air flows induced by the filament heat could increase the droplet concentration by thermal mixing of the air.

For laser beams in the near-infrared (800 nm), both laboratory (Petit *et al.*, 2010) and field studies (Henin *et al.*, 2011) have shown that laser-induced condensation is associated with the local production of high ozone and NO_x concentrations in the gas phase due to photo-ionization and photo-dissociation. Henin *et al.* (2011) have shown using ion chromatography on laser-produced particles sampled on filters that substantial amounts of NO_3^- ions can be detected in the laser-condensed particles. Rohwetter *et al.* (2011) have also modeled the cinetics and thermodynamics of this process. The formation of highly hygroscopic HNO_3 has therefore been identified as one major pathway to support near-infrared laser-induced condensation of aerosol mass for relative humidity (RH) in the atmosphere higher than 70 %. Saathoff *et al.* (2013) also suggest that the nonlinear photochemistry with organics could participate to the laser-induced aerosol condensation as they demonstrated the very high impact of α-pinene traces on the particle growth.

In the mid-infrared, multi-photon processes are much less efficient than in the near-infrared. For example, 38 photons are needed to ionize O_2 molecules at 3.9 µm whereas only 8 – 11 photons are enough at 800 – 1030 µm. Therefore, the main pathway to condense aerosols in the near-infrared seems unlikely to have a big impact in the mid-infrared.

In this chapter, I demonstrate in a collaboration with the group of Professor A. Baltuška in Vienna (AU) that aerosol condensation can also be induced by mid-infrared laser filaments. This promising experiment shows that despite the low photon energy at those wavelengths, aerosol condensation is possible. Hints of chemical pathways to investigate are given at the end of the chapter. A more precise study of the aerosol composition produced by mid-infrared laser filaments should be conducted in the future. In the near-infrared, Mongin *et al.* (2015) have published the first thorough study of laser-generated aerosol composition and this paper is

presented in Appendix A as I have participated in these experiments. This paper is of special interest for atmospheric chemists as near-infrared laser-induced organics oxidate much faster than in normal atmosphere. Ultrashort laser pulses could therefore strongly shorten the duration of experiments studying the aging of organics in the atmosphere without adding any chemical reactors and changing the atmospheric chemical composition as it is sometimes done nowadays.

3.1 Background of Atmospheric Aerosol Condensation

Before discussing the interaction of laser filaments with the atmosphere, it may be useful to remind the reader of basic concepts of atmospheric composition and dynamics. The important definitions and processes involved that are relevant to the interaction of laser filaments with the atmosphere will be presented in this section. For a more detailed presentation of this specific topic, the PhD theses of Rohwetter (2011) and Henin (2013) give a more detailed view of the topic. For a broader insight in atmospheric chemistry and physics, the books of Seinfeld & Pandis (2006) and Pruppacher & Klett (1978) are very thorough and inspired this section.

3.1.1 Gases Present in the Atmosphere

In this present work, the considered atmospheric layer is the lower part of the troposphere. It is the lowest layer of the atmosphere, extending from the Earth's surface up to the tropopause at 10 to 15 km altitude depending on the latitude and the time of year. This layer is characterized by a decreasing temperature with hight which eventually leads to cloud formation.

The general gaseous composition of the atmosphere is well-known as being roughly 78 % nitrogen (N_2), 21 % oxygen (O_2) and 1 % argon (Ar). What is less known is the constitution of all the other traces present in the gaseous or particle form. Traces are generally quantified in *parts per million*, 1 ppm = 1 µmol/mol, *parts per billion*, 1 ppb = 1 nmol/mol or *parts per trillion*, 1 ppt = 1 pmol/mol.

Virtually every element in the periodic table is found in the atmosphere but some big classes of species can be made according to their chemical composition. Below are described a few of the most relevant chemical compounds for aerosol formation in the atmosphere.

Sulfur is present in the atmosphere at a very low total volume ratio of less than 1 ppm but it has a non-negligible impact on atmospheric chemistry and on climate. The main compounds found in the atmosphere are H_2S, CH_3SCH_3, CS_3, OCS, SO_2, H_2SO_4 and sulfates. Chemical reactivity of atmospheric sulfur compounds is inversely related to their *oxidation state*, which is an indicator of how many electrons the compound lost – an atom with an excess of electrons will have a negative oxidation state. In normal atmosphere, sulfates are very efficient to produce aerosols as they are extremely water soluble

In contrast with sulfur, nitrogen is the most present gas in the atmosphere. A big fraction of this nitrogen is inert in the atmosphere as the triple bond of the N≡N is very strong and makes the N_2 molecule extremely stable. The important nitrogen-containing traces are N_2O, N_2O_5, NO, NO_2, NO_3, HNO_3 (nitric acid) and NH_3 (ammonia). The sum of NO and NO_2 is usually designated as NO_x. Nitrogen-containing compounds are very important in the atmospheric chemistry and in laser-induced aerosol condensation. HNO_3 is extremely water-soluble as H_2SO_4 and in the presence of NH_3, it can form amonium nitrate aerosols. Petit *et al.* (2010) demonstrated that HNO_3 concentrations in the laser-filament volume could reach the parts per million range, which

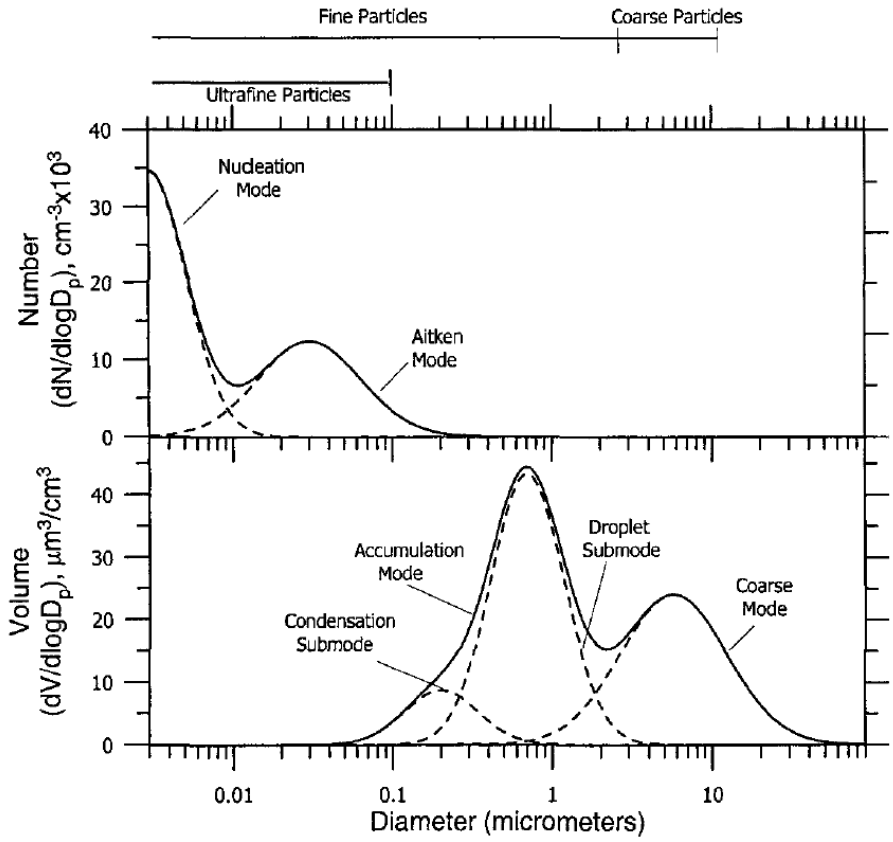

Figure 3.1: Typical number and volume size distributions of atmospheric particles (Reprint from Seinfeld & Pandis (2006)).

is 1000–10 000 times higher than in the natural atmosphere according to Chiwa *et al.* (2008) and that they therefore play a key role in the laser-induced aerosol condensation.

Carbon atoms have four valence electrons and they can therefore share bonds with on to four other atoms. Volatile organic compounds (VOCs) are the entire set of vapor-phase atmospheric organics, i.e. molecules containing carbon and hydrogen atoms. Saathoff *et al.* (2013) suggested that they could play a non-negligible role in laser-induced aerosol condensation.

3.1.2 Atmospheric Aerosols

In the previous chapter, water droplets were described as particles and this term can be extended here to any substance that exists as a liquid or solid in the atmosphere under normal conditions and is of microscopic or submicroscopic size but larger than molecular dimensions. This definition is taken from Seinfeld & Pandis (2006) and generalized to include water droplets.

Aerosols are defined as a suspension of fine solid or liquid particles in air. Their diameters range from a few nanometers to tens of micrometers. Those particles can change their size and composition by condensation, evaporation, coagulation with other particles or chemical reactions. Aerosols arise from many different sources, natural such as sea salt, biological debris or mineral dust among others or anthropogenic such as industrial dust, ashes or volatile organic compounds.

An aerosol population is usually described by its size distribution. In general, two modes can be observed in the atmospheric aerosol size distribution with respect to the aerosol volume (Figure 3.1

lower panel). The first mode, called *accumulation mode* is between ∼0.1 and ∼2 µm and is the result of condensation of sulfates, nitrates and organics from the gas phase and coagulation of smaller particles. A second mode called the *coarse mode*, that lies between ∼2 and ∼50 µm includes particles produced by erosion or other mechanical processes.

It is interesting to note by comparing the two panels of Figure 3.1 that although most of the volume, i.e. of the particle mass can be attributed to the larger particles, their number is actually very low in comparison with the particles smaller than 0.1 µm. These are the particles that will be studied in the experiment further down in this chapter. They can also be separated in two distinct modes. The *nucleation mode* is made of freshly nucleated aerosols smaller than 10 nm whereas the *Aitken nuclei* are between 10 and 100 nm or so and are usually condensation nuclei upon which secondary material such as water has condensed.

As shown above Figure 3.1, particles are also usually classified into three categories depending on their size. Particles smaller than 100 nm are *ultrafine*, those larger than 2.5 µm are *coarse* and those in-between are *fine*.

3.1.3 Nucleation

In the atmosphere, a gas vapor will not transform into liquid at once when the free energy is lower than the phase-transition threshold. Rather, small *clusters* will first form. *Nucleation* is defined as this abrupt appearance of a new phase of a substance. Here, only the phase-transition from gas to liquid will be treated as this is the most relevant phase-transition for this work but sublimation (gas to solid transition) or crystallization (liquid to solid transition) also occur in the atmosphere.

Nucleation can occur in a fully gaseous environment, this process is called *homogeneous nucleation*. When the gas condenses on a preexisting substance or surface, such as an ion or a solid particle also called *condensation nucleus* (CN), this is called *heterogeneous nucleation*. In addition, nucleation can be *homomolecular*, i.e. involving a single species, or *heteromolecular*, involving two or more gas species. In consequence, four types of nucleation processes can be indentified:

- Homogeneous-homomolecular: gas to liquid phase transition of a single species, with no foreign substances involved.
- Homogeneous-heteromolecular: gas to liquid phase transition of a mixture of species, with no foreign substances involved.
- Heterogeneous-homomolecular: gas to liquid phase transition of a single species on a preexisting substance.
- Heterogeneous-heteromolecular: gas to liquid phase transition of a mixture of species on a foreign substance.

The homogeneous nucleation of water is a very slow process occurring at extremely high *relative humidity* (RH). The relative humidity is defined as the ratio of partial pressure of H_2O vapor to the saturation vapor pressure of H_2O at a given temperature. It is usually expressed in percent

$$\mathrm{RH} = 100\frac{P_{\mathrm{H_2O}}}{P^2_{\mathrm{H_2O}}} \tag{3.1}$$

When this ratio is above 100 %, the air is *supersaturated* with water. The water homogeneous nucleation rate at 200 % RH is about 10^{-54} cm^{-3} s^{-1}. This means that more than 10^{46} years would be necessary to form one droplet in 1 cm^{-3} of air. As droplets appear in the atmosphere at relative humidities just slightly above 100 % and feature much higher nucleation rates than this, it means that water nucleate easier via heterogeneous-heteromolecular processes. If aerosols such as ions, soluble or insoluble particles are present in the supersaturated air, they will act as *cloud condensation nuclei* (CCN). Cloud formation is therefore only possible in presence of aerosols.

The initial growth of freshly nucleated particles to a detectable diameter is driven by the competition between the aggregation of new molecules from the surrounding gas, the evaporation of the cluster and the scavenging via coagulation of preexisting aerosols. The balance between those processes determines the production rate of the detectable new particles. More in-depth theory on this very vast topic can be found in Kulmala *et al.* (2004) and in the specific conditions of laser-induced aerosol condensation in Rohwetter (2011) and Henin (2013).

3.1.4 Laser-Induced Aerosol Condensation

The photo-excitation of atmospheric particles can accelerate the aerosol formation by breaking molecules, exciting or ionizing them.

Photo-dissociation, also called photolysis, are reactions of the kind Seinfeld & Pandis (2006, p. 75)

$$\mathrm{A} + h\nu \rightarrow \mathrm{B} + \mathrm{C} \tag{3.2}$$

in which $h\nu$ is a photon of frequency ν. A simple example of photo-dissociation is the dissociation of O_2 in two individual oxygen molecules by a photon of 240 nm wavelength.

Photo-ionization on the other hand is the extraction of an electron from a molecule or an atom by one or many photons. In the latter case, one talks of multi-photon ionization, as already discussed in Section 1.1.1. For example, 12.6 eV are needed to extract the outer electron of an O_2 molecule. This means that 8 photons at 800 nm are needed to ionize one single molecule of O_2.

3.2 First Results of Mid-Infrared Laser-Induced Condensation in Air

3.2.1 Material and Methods

In this experiment, a 3.9 µm, 15 to 28 mJ home-made laser from the group of Professor Baltuška described by Andriukaitis *et al.* (2011) was shot through a cloud chamber (Figure 3.2). The 95 fs laser pulses were sent at a 20 Hz repetition rate. The beam diameter was 5 mm at full width at half maximum (FWHM). The laser was focused with a 75 cm CaF_2 lens if not otherwise specified. The 295 GW maximum peak power corresponded to typically 3.7 critical powers of ∼80 GW for filamentation at 3.9 µm according to Mitrofanov *et al.* (2015). Optionally, the beam was compressed to ∼83 fs by inserting a 2 mm YAG slab at Brewster angle in the beam before entering the chamber. With this compression, the peak power reached 4.2 P_{cr}.

In all configurations, the filament was produced at the level of the detector sampling inlets.

The cloud chamber dimensions were 95 × 60 × 60 cm inside with 12 cm thick expanded polystyrene walls to insure insulation and 4 cm diameter holes on both sides to propagate the beam. The laser filament was centered in the middle of the chamber. Water ice was placed approximately 10 cm under the filamenting region and tepid water (∼30 °C) was placed in two trays around 20 cm above the filamenting region. A plexiglas window was placed on the top of the chamber to avoid any turbulence in the chamber while allowing to monitor the experiment from outside.

The air in the chamber was sampled from the side, 2 cm away from the beam. A TESTO 635-2 relative humidity (RH) and temperature (T) sensor was placed at the center of the filament, roughly 2 cm below the beam. An optical aerosol sizer, the GRIMM 1.109, measuring particles from 250 nm to 32 µm in 32 size classes at a 1.5 l/min sampling rate and 12 s sampling interval, was placed approximately 10 cm upstream of the temperature and relative humidity measurement. It was equipped with a nanoparticle detector (GRIMM NANOCHECK) measuring the concentration and median size of particles between 25 and 300 nm with the same sampling rate than the GRIMM 1.109. An ozone detector (HORIBA APOA-350E) was sampling roughly 10 cm downstream of the filament middle at a rate of 2 l/min and measuring the ozone concentration every 20 s. A photodiode (PD) was used to monitor the white light from the filament on the back of a window around 10 cm after the cloud chamber. It was used to assess the laser ON and OFF times. The CO_2 concentration was also monitored in the chamber with a TROTEC BZ30 device, that was

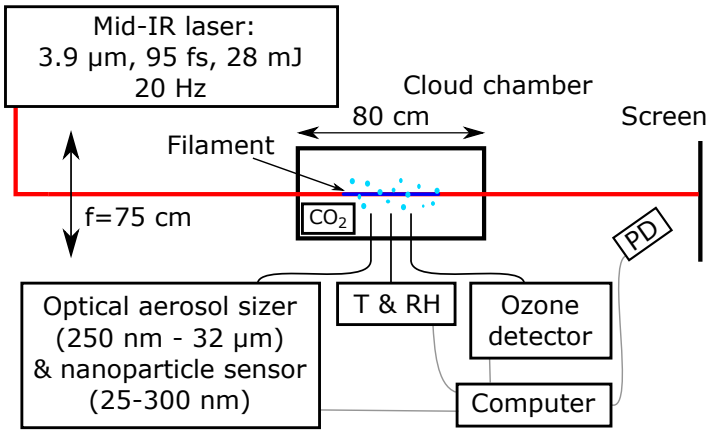

Figure 3.2: Experimental setup.

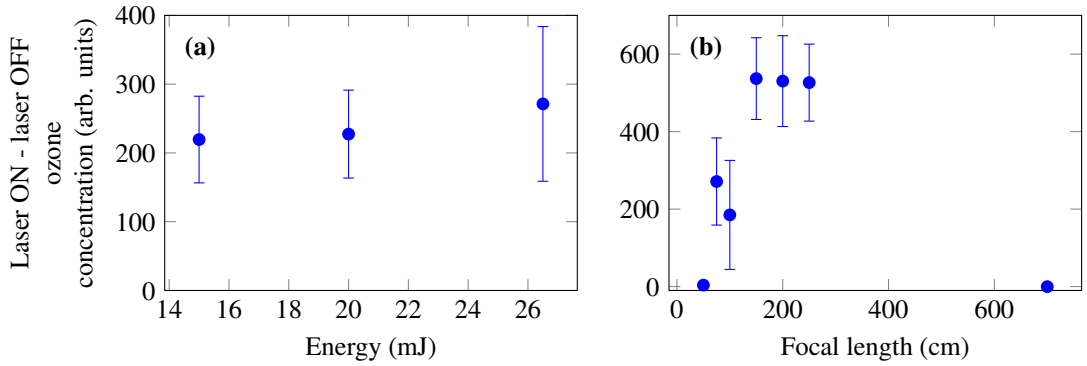

Figure 3.3: Ozone production as a function of the incident energy (a) and geometrical focusing length (b).

also used to cross-check the temperature and relative humidity measured by the TESTO 635-2 device.

The CO_2 level in the chamber stayed pretty constant over the campaign, around 600 to 700 ppm. It did not vary sufficiently to influence the condensation and it was also not impacted by the condensation.

Data processing For each parameter under investigation, the impact of the laser was assessed by comparing the values while the laser was firing (ON period) and the time before the laser was switched on. More specifically, the time starting 2 min after the laser was switched on in order to remove the transient regime and until the laser was switched off was taken as the laser ON time. The laser OFF period correspond to the 2 min before the laser was sent through the chamber. Each experiment was repeated 2 to 10 times. The stability of the environmental and laser conditions allowed to merge all times corresponding to each condition into a single set, in order to compute the average value and standard deviation for both the ON and OFF periods of time.

Filament properties The laser pulses produced a filament in each investigated configuration. The filament length increased linearly from 3 cm to 46 cm when the focal length was increased from 25 cm to 2.5 m. At 7 m focal length, the filament was approximately 180 cm long. Under 3 m focusing, the filament diameter was around 0.4–0.6 mm and this diameter increased to 0.7–0.8 mm at 7 m focal length as described by Ališauskas *et al.* (2012).

3.2.2 Results

Primary process – Ozone and nanoparticle production Switching the laser on increased the measured ozone concentration typically by a factor 100 with regard to the background level. Simultaneously, the number density of particles in the 25–300 nm range rises by a factor 10 to 100 and even beyond, reaching up to 10^6 cm^{-3}. As displayed on Figure 3.3a and Figure 3.4a, the corresponding concentrations tend to rise with increasing energy. On the other hand, compressing the pulse duration to 83 fs does not significantly affect the ozone nor the nanoparticle production. The concentrations also display a smooth maximum for a moderate focusing ($f \approx 200$–250 cm, Figure 3.3b and Figure 3.4b), i.e. in conditions that optimize the plasma production.

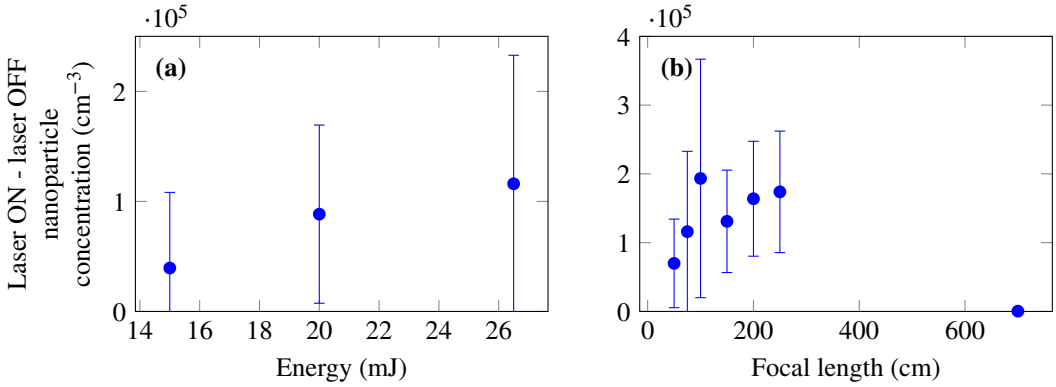

Figure 3.4: Nanoparticle (25–300 nm) production as a function of the incident energy (a) and geometrical focusing length (b).

Secondary process – Particle growth The larger particles progressively increase their concentration over at least 10 min, evidencing a progressive growth of some of the particles. This growth can be observed for sizes up to a typical diameter of 0.6 µm (Figure 3.5). Beyond this size, the two size distributions with and without laser cannot be distinguished. Furthermore, the conditions corresponding to the strongest nanoparticle formation (highest energy, loose focusing) do not maximize the concentration of generated larger particles. Rather, the latter are more abundant for the uncompressed beam and a tight focusing ($f = 50$ cm) where the concentrations in ozone and nanoparticles are lower (Figure 3.6).

The difference in efficiencies between nucleation and growth of particles can be understood by integrating the size distribution of Figure 3.5. In all conditions, a large majority (80–97 %, except for $f = 700$ cm where no nucleation occurs) of the condensed volume, or in other words of the total mass, is concentrated in the first size class, i.e. particles below 300 nm, with a median size of 50 to 100 nm. The corresponding density of condensed mass lies in the 11 to 12 µg/m^3, a value comparable with the initial water vapor contents in the air at 15° and 90 % RH. Therefore, in the diffusion-limited regime typical of this experiment, where transport of moisture from remote regions of the chamber volume is very slow, a great generation of nanoparticles harvests a fraction of the available moisture sufficient to prevent their further growth. Indeed, the nucleated particles are in competition for the water vapor and none can get enough to grow. This interpretation is

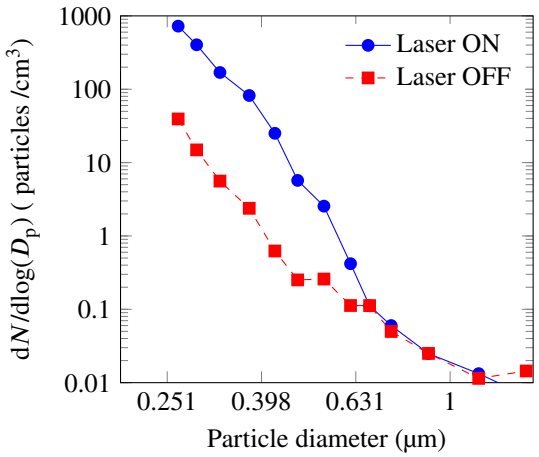

Figure 3.5: Size distribution of the background aerosols and of the aerosols when the reference beam is sent. D_p is the particle diameter and N is the particle number per cm^3.

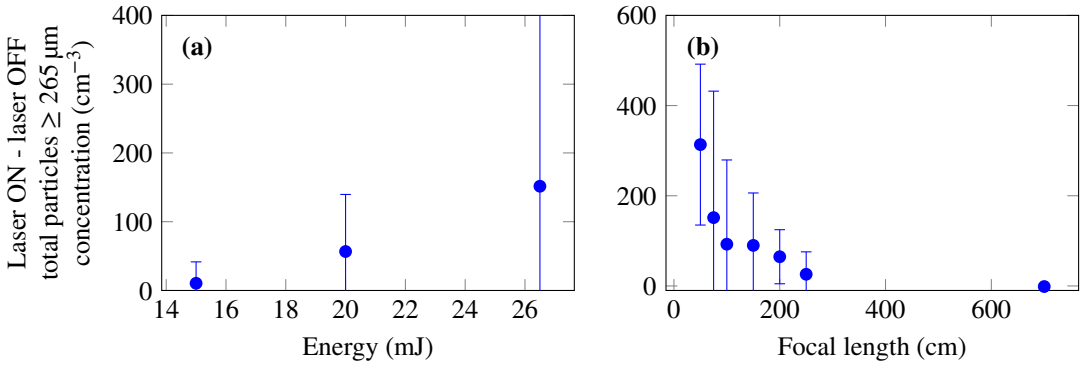

Figure 3.6: Increase of the particle number over 250 nm as a function of the incident energy (a) and the focusing (b).

confirmed by the fact that the growth of the larger particle concentration saturates after a couple of minutes, very soon after the nanoparticle concentration reaches its plateau.

Note that the growth by coalescence is negligible in these experimental conditions. Considering an average quadratic diffusion speed due to Brownian motion of the 50 nm particles of $< v >= \sqrt{k_B T/m} = 0.25\,\mathrm{m/s}$ (Kheifets *et al.*, 2014) and a mean free path of $1/\sigma n$, with $\sigma = \pi d^2$ as the collision distance is $2r$, and $n \approx 10^5/\mathrm{cm}^3$, the mean free path is in the range of 1 km and the collision time in the range of tens of minutes.

3.2.3 Discussion

The massive production of ozone and nanoparticles, as well as the moderate increase of particles above a few hundreds of nanometers and of their associated condensed mass, is surprisingly analogous to previous results obtained both with near-infrared lasers by Petrarca *et al.* (2011), Henin *et al.* (2011) and Mongin *et al.* (2015) and with ultraviolet lasers by Joly *et al.* (2013).

From a quantitative point of view, the concentration of the 25–300 nm particles induced by the laser is comparable with those observed in those previous experiments at 800 nm with various incident energies (160 mJ to 3 J), as well as a few tens of millijoule in the ultraviolet.

On the other hand, the ozone production is poorly correlated with the nanoparticle production. In particular, nanoparticles are produced even when no ozone is produced (see Figure 3.3 and Figure 3.4). Mongin *et al.* (2016b) showed that the N_2 fluorescence intensity in 3.9 µm filaments is only 10 % of that of the 800 nm filament (see also Figure 2b of Appendix B). All this tends to indicate that the nitrate route presented by Mongin *et al.* (2015) in Appendix A for near-infrared laser-induced aerosol condensation is not the dominant chemical pathway to produce aerosols in the mid-infrared.

Another chemical pathway specific of the mid-infrared could rely on the photo-dissociation of C–H bonds in volatile organic compounds (VOCs). Indeed, C–H bonds have a strong vibrational resonance between 3.3 and 3.6 µm, depending on their chemical environment. The wide spectrum of the supercontinuum generated by the mid-infrared filaments is maybe intense enough at these wavelengths to pump efficiently resonant excitations by ladder-climbing and ultimately photo-dissociate the C–H bonds. The better cross-section for C–H photo-dissociation due to this resonance and the lower number of photons needed than for photo-dissociation and multi-photon ionization of O_2 at 3.9 µm (respectively 17 and 38-photons processes) could explain this new

pathway.

Mid-infrared filaments also deposit less energy in the air (7 % in comparison with 12 % at 800 nm according to (Mongin *et al.*, 2016b)) and this energy is spread over a wider volume. Both the temperature variations and the associated gradients are weaker, resulting in a reduced heating and associated convection and mixing of air masses. Therefore, contributions of air mixing by convection such as suggested by Ju *et al.* (2012) are very unlikely to contribute.

3.3 Conclusion

Mid-infrared laser pulses of 25 mJ efficiently induce condensation, with concentrations in nanoparticles close to those of 11 mJ ultraviolet pulses and 160 mJ to 3 J, 800 nm pulses (Joly *et al.*, 2013, Henin *et al.*, 2011, Petrarca *et al.*, 2011). These similar concentrations are related to the depletion of the available moisture that limits the condensation and especially the further growth of the generated particles.

The chemical pathway for laser-induced aerosol condensation is different at 4 µm than at 800 nm wavelength. There are some hints that aerosol production at 4 µm could include a contribution of photo-dissociation of C−H bonds by ladder-climbing in volatile organic compounds.

A way to verify this assumption would be to analyze the laser-induced NO_x concentration to show that the main chemical pathway at 800 nm is not dominant at 4 µm. Investigating the particle condensation rate at a shorter wavelength, around the 3.3 to 3.6 µm absorption of the C−H bond could help confirming this hypothesis.

Panagiotopoulos *et al.* (2015) demonstrated that mid-infrared filaments can propagate over long distances and are resistant to strong spatial and temporal perturbations. They could therefore be good candidates in perspective to seed clouds with laser filaments instead of current chemical cloud seeding.

How to Accurately Characterize Filament Charge Density 4

As discussed in Chapter 1, laser filaments ionize the air molecules, leaving behind them a plasma channel. Besides the creation of new aerosols in the atmosphere as discussed in the previous chapter, this plasma is essential to describe the effect of laser filaments on electric fields. This is a very important topic for laser applications in atmospheric physics as interactions with thunderstorm clouds could help guide or prevent lightning strikes on sensitive buildings.

La Fontaine *et al.* (1999), Panagiotopoulos *et al.* (2015) and Houard *et al.* (2016) demonstrated that at respectively 800 nm, 1030 nm and 4 µm, the amount and distribution of free electrons in the plasma induced by the laser filament is a key parameter to assess the presence of self-guided mechanism within the laser beam and to estimate the losses along the beam propagation axis to propagate over long distances. This information is also necessary to define the electric properties of the laser filaments and their ability to interact with high-voltage sources.

Several methods have been suggested to characterize the ionization along the filaments, providing a longitudinal profile of the free charges. Hosseini *et al.* (2003) observed the backscattered fluorescence from the excited nitrogen molecules along the laser filament for remote characterization of filament length via LIDAR technique (light detection and ranging technique, (Measures, 1984)). In the same idea, Bernhardt *et al.* (2008) investigated the side-spectrum of the filament as a measurement of the induced plasma density. Yu *et al.* (2003) on the other hand used the calibrated filament-induced shock-wave as a plasma measurement when Centurion *et al.* (2004), Rodriguez *et al.* (2008) and Abdollahpour *et al.* (2011) used holographic techniques and Tzortzakis *et al.* (2000b), Minardi *et al.* (2009) and Liu *et al.* (2010) shadowgraphy. Microwave wave-guides are also used as plasma probes by Alshershby *et al.* (2013) and Papeer *et al.* (2013) and Bodrov *et al.* (2011) uses terahertz scattering.

Beside all these different ways of determining the free electron concentration in the laser-induced plasma, some simple electrical setups have been developed such as conductivity characterization by Tzortzakis *et al.* (1999, 2000b), Vujicic *et al.* (2006), Lu *et al.* (2015), capacity change measurements by Schillinger & Sauerbrey (1999), Ladouceur *et al.* (2001), Akturk *et al.* (2009), Henin *et al.* (2009), Abdollahpour *et al.* (2011) and Ionin *et al.* (2014), as well as ionic current measurements by Polynkin (2012) and Mongin *et al.* (2016b).

Electric measurements are widely used because their implementation is rather simple. Furthermore, they appear as the most direct characterization of free charges. However, the measurement is still indirect as the results are influenced by screening by free charges, induction, as well as the plasma dynamics (electron attachment, ion–ion and electron–ion recombination) that affect the fraction of charges that reach the electrodes as discussed by Zhao *et al.* (1995) and Vidal *et al.* (2000). Furthermore, several electrode configurations and signal analysis strategies are promoted by different groups, with an ongoing debate about their respective validity (Abdollahpour *et al.*, 2011, Polynkin, 2012).

Hosseini *et al.* (2004b) demonstrated that the signal from backward emitted nitrogen fluorescence, the acoustic wave method and the capacity change measurements yield qualitatively consistent results. A precise evaluation of the respective accuracies of each electrical measurement setup is nevertheless still needed.

This chapter will investigate in detail the validity of electric characterization methods with different electrode configurations and signal analysis commonly used to characterize the filament plasma. The cumulated electrical response of two single filaments sent separately through the apparatus will be compared to the signal recorded when the two laser filaments are sent together through the setup to assess the response linearity with the amount of free charges created. I have personally contributed to this work submitted for publication by setting up the experiment and collecting the data.

4.1 Experimental Setup

The experimental setup is sketched in Figure 4.1a. A laser system producing 50 fs pulses at a central wavelength of 800 nm and a repetition rate of 1 kHz was slightly focused ($f = 2$ m) and separated by a 70/30 beam splitter into two sub-beams labeled A and B and carrying 3 and 1.5 mJ, respectively. The two beams propagated in air, parallel and at a distance of 2 mm from each other. Each beam generated one filament. Two circular plane electrodes with a separation of 2 cm were positioned close to the most intense part of the beam, characterized by the strongest visible fluorescence and the maximum signal of the electric measurement. Unless otherwise specified, the filaments propagated in the middle of the gap between the two electrodes. The electrodes are two 2 cm by 2 cm square copper PCB facing each other, with 2 cm between them.

Two configurations were investigated, with the electrodes positioned on both sides of the filaments and parallel to the plane containing the two sub-beams (hereafter denoted the parallel

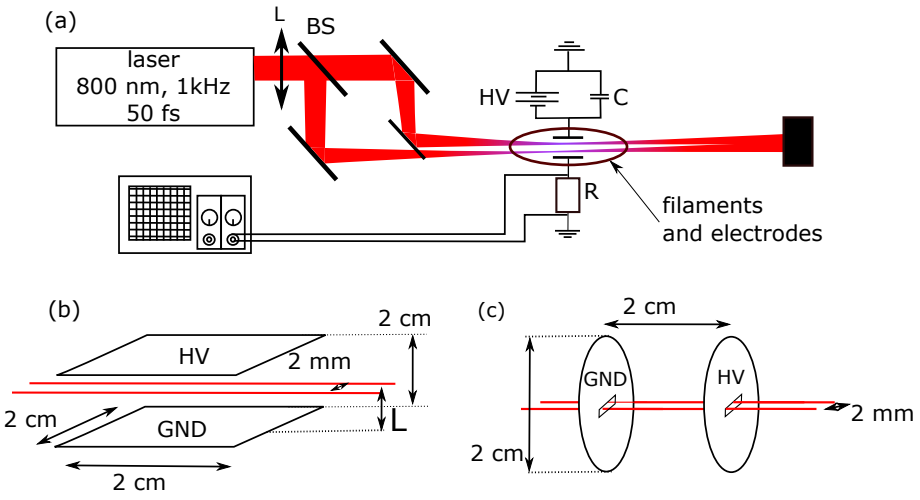

Figure 4.1: Experimental setup. A kilohertz 800 nm 50 fs laser system delivering 5 mJ is focused with an $f = 2$ m lens (L) and split in two arms with a 70/30 beam splitter (BS), creating two filaments sent between two electrodes. One of these electrodes is connected to a high voltage supply (HV) and a capacitor (C), while the other is connected to the ground (GND). The current flowing to the ground is monitored on an oscilloscope through a resistor (R) (a). Two main electrode configurations are used: parallel configuration (b) and longitudinal configuration (c).

configuration and considered as the reference condition, Figure 4.1b) and electrodes located longitudinally in the propagation direction, with the filament propagating through them (longitudinal configuration, Figure 4.1c).

The electrodes were connected to a DC high voltage generator delivering 2 to 10 kV. The transient current generated by the filament was recorded via an oscilloscope on a resistor $R = 47\,\mathrm{k\Omega}$ for the parallel configuration, respectively $R = 13\,\mathrm{k\Omega}$ for the longitudinal configuration. The coupling impedance of the oscilloscope was 1 MΩ and its capacitance was 190 pF, resulting in a circuit response time of approximately 8 µs. The capacitor load under 10 kV was $1.6 \cdot 10^6$ C, five orders of magnitude larger than the total charge collected on the electrodes, ensuring that the charge supply by the capacitor was not limiting the measurement. The curves were averaged 500 times on the oscilloscope.

The first setup (parallel configuration, Figure 4.1b) was used to perform both the *polarization response measurement*, in which a current was induced by the fast change of the dielectric constant due to the plasma, and the *ionic current measurement*, where a current due to a transverse flow of ions was measured. The second setup (longitudinal configuration, Figure 4.1c) was used to perform the *electronic current measurement*, due to the ohmic bridging of the gap by the electrons.

The linearity of these different measurements was investigated with regard both to the bias electric field and to the amount of charges in the electrode gap. This was achieved respectively by varying the voltage between 2 and 10 kV and by comparing the sum of the individual signals obtained from the filaments A and B individually, hereafter denoted A + B, with the signal obtained when both filaments propagated together between the electrodes (hereafter denoted AB). Both filaments were, if not otherwise specified, separated by a distance of 2 mm, and were optically independent because the time delay between both laser pulses was larger than their duration. When possible, both the peak of the current flow and its time-integrated value – i.e. the total charge – were considered, in order to assess their relevance.

4.2 Results

As displayed in Figure 4.2(a), the typical current recorded on the ground electrode in the case of the parallel configuration exhibits two time scales.

The first one consists of a short negative peak, resulting from the fast polarization of the

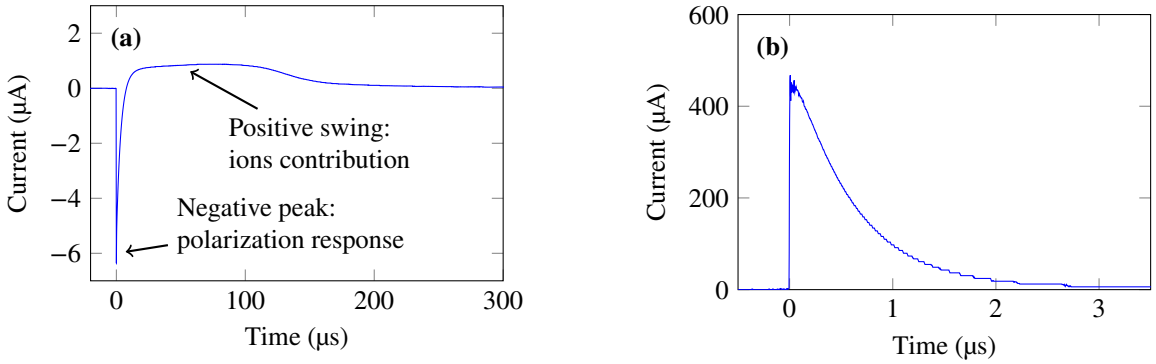

Figure 4.2: Typical shape of the signal measured by the oscilloscope in the parallel, perpendicular (a) and longitudinal (b) configurations.

plasma channel. This is due to the charge separation under the external field and it causes a transient current related to the capacity change between the electrodes. When one single filament is propagated between the electrodes, the electron displacement with time $x_e(t)$ in an electric field E along the x-axis perpendicular to the electrodes can be written as

$$x_e(t) = \mu_e E t \tag{4.1}$$

where μ_e is the electron mobility (Zhao *et al.*, 1995)

$$\mu_e = -\frac{N_0}{3N_{\text{Tot}}}\left(\frac{5\cdot 10^5 + E_0}{1.9\cdot 10^4 + 26.7\cdot E_0}\right)^{0.6}\left[\frac{\text{m}^2}{\text{V}\cdot\text{s}}\right] \tag{4.2}$$

N_0 being the molecule density at 1 atm, N_{Tot} the initial heavy species density and $E_0 = EN_0/N_{\text{Tot}}$.

The induced polarization is

$$P(t) = eN_e(t)x_e(t) \tag{4.3}$$

where e the elementary charge and $N_e(t)$ the electron density. The electric displacement field D is

$$D = \varepsilon_0 E + P \tag{4.4}$$

The variation of D with time is a density of current, according to Ampere's law. The current density variation due to the induced polarization is therefore

$$J_P = \frac{\partial P}{\partial t} \quad \Leftrightarrow \quad J_P = e\left(x_e(t)\frac{\partial N_e(t)}{\partial t} + N_e(t)\frac{\partial x_e(t)}{\partial t}\right) \tag{4.5}$$

with the electron density averaged over the whole electrode surface.

The induced current signal due to this current density decays within 8 ns (1/e decay of the maximal electron density) because of the electrons attachment to O_2 molecules and because of the electron–ion recombination in agreement with Zhao *et al.* (1995) and Vidal *et al.* (2000). For an initial electron concentration of $1.8\cdot 10^{21}$ m^{-3}, the contributions of these terms are 20 % and 80 % respectively. Such dynamics is not resolved temporally by the detection setup.

The attachment of the free electrons is faster than their travel over 1 cm to the electrodes. With an electronic mobility varying between 0.14 m^2/Vs and $7\cdot 10^{-2}$ m^2/Vs under fields between $1\cdot 10^5$ and $5\cdot 10^5$ V/m as described by Zhao *et al.* (1995), the electrons transit time to the electrodes vary between 270 and 700 ns. During this time, the electron density will have decayed to 10^{11} and 10^8 electrons per cubic meter respectively if one considers an initial electronic density of 10^{20} m^{-3}. Therefore, almost none of the initial electrons are collected on the electrodes and the negative polarization signal overrides the competing positive signal that would correspond to the collection of free electrons on the positive electrode.

The second time scale is the consequence of the ions traveling to the electrodes of opposite polarity at a typical velocity of 10 m/s, according to Zhao *et al.* (1995). As detailed by Polynkin (2012), the collection of these free charges yield an ionic current consisting in a long positive swing of 200 µs.

In the longitudinal configuration, the signal recorded show the typical shape displayed in Figure 4.2(b). Here a unique positive signal is observed, mainly due to electrons collected close to the electrodes during the filament lifetime. No ionic signal is observed at longer time scales. One possible reason could be that ions of opposite polarity recombine during their travel between the electrodes as they travel within the same volume but in opposite directions.

In the following, the focus will be successively driven to the ionic current, the fast capacity change signal in the parallel configuration and the electron current (conductivity) in the longitudinal configuration.

4.2.1 Ionic Current

The ionic contribution in the recorded signal is given by the long positive swing in the parallel configuration. In this case, the sum of the charge collected from the individual filaments, A+B, is equal to that of the filaments measured jointly, within an error of 12 % at most (Figure 4.3a).

The total charge collected on the electrodes increases linearly with the electric field (Figure 4.3a). This can be understood considering the second order kinetics of the ionization recombination process. This kinetics, dominant after few tens of nanoseconds, implies an evolution of the ion density N_{ions}

$$\frac{dN_{\text{ions}}}{dt} = -\beta_{np} N_{\text{ions}}^2 \quad \Leftrightarrow \quad N_{\text{ions}} = \frac{N_0}{1 + N_0 \beta_{np} t} \tag{4.6}$$

with N_0 being the initial concentration and $\beta \simeq 2 \cdot 10^{-13}\ \text{m}^3/\text{s}$, the ion–ion recombination rate at 300 K. Considering a typical value for N_0 in the order of $10^{21}\ \text{m}^{-3}$, the concentration of ions after some tens of nanoseconds is very close to $1/(\beta t)$, which is independent from the initial density. As the quantity of ions collected by the electrodes is proportional to the concentration at

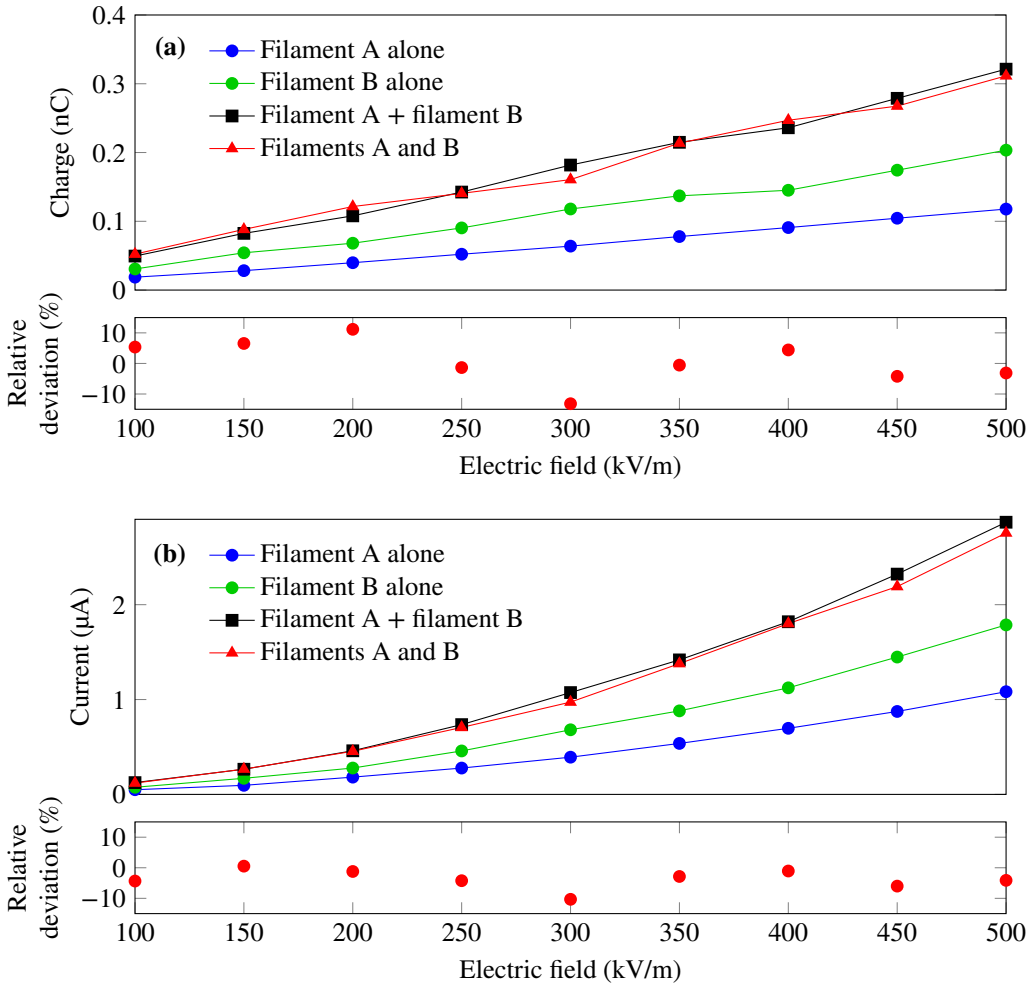

Figure 4.3: Linearity of the collected charge (a) and the peak current (b) measured in the ionic (long) positive swing by a capacitive probe in the parallel configuration (Figure 4.1b).

the time of arrival $t_f \simeq \frac{1}{\mu_{ion} E}$, where $\mu_{ion} \simeq 2.5 \cdot 10^{-4}\,\mathrm{m^2/(Vs)}$ is the ionic mobility according to Zhao *et al.* (1995), this results in a linear dependence in field strength.

The peak current is also linear with respect to the available charge, with a maximum deviation of 10 % (Figure 4.3b). This signal rises quadratically with the electric field, which is consistent with the linear increase of the collected charge with the electric field. This correlates well with the linear increase of the drift speed presented above, implying a constant ionic mobility (Zhao *et al.*, 1995).

Approaching the filaments from either electrode splits the positive swing into two sub-peaks corresponding to the two times of flight of the positive and negative ions to reach their respective target electrode. While the maximum current of the second bump keeps linear with the available charge within 10 %, even when the filaments are as close as 2 mm to either electrode, the first positive sub-peak (i.e charges having a shorter way to travel) deviates from linearity by up to 40 % and tends to deform when the filaments approach one of the electrodes. The observed deviation from linearity and the deformation of the first sub-peak is due to the influence of the fast negative polarization signal and the contribution of electrons reaching the electrodes when the filaments get closer than 5 mm, that is when their travel time is below 100 ns.

These features demonstrate that the capacitive probe in a parallel configuration is highly robust to misalignments, either permanent or associated to beam wandering. This robustness is remarkable, considering the finite size of the electrodes and the associated inhomogeneities in the electric field. To confirm the relatively low impact of the electric field inhomogeneity on the peak current linearity, the square electrodes were replaced by 7 cm diameter spherical electrodes spaced with 2 cm between their nearest point. This configuration further reduced the maximum deviation to 2 %.

The sensitivity of the capacitive probe to the screening of the electric field by space charges was

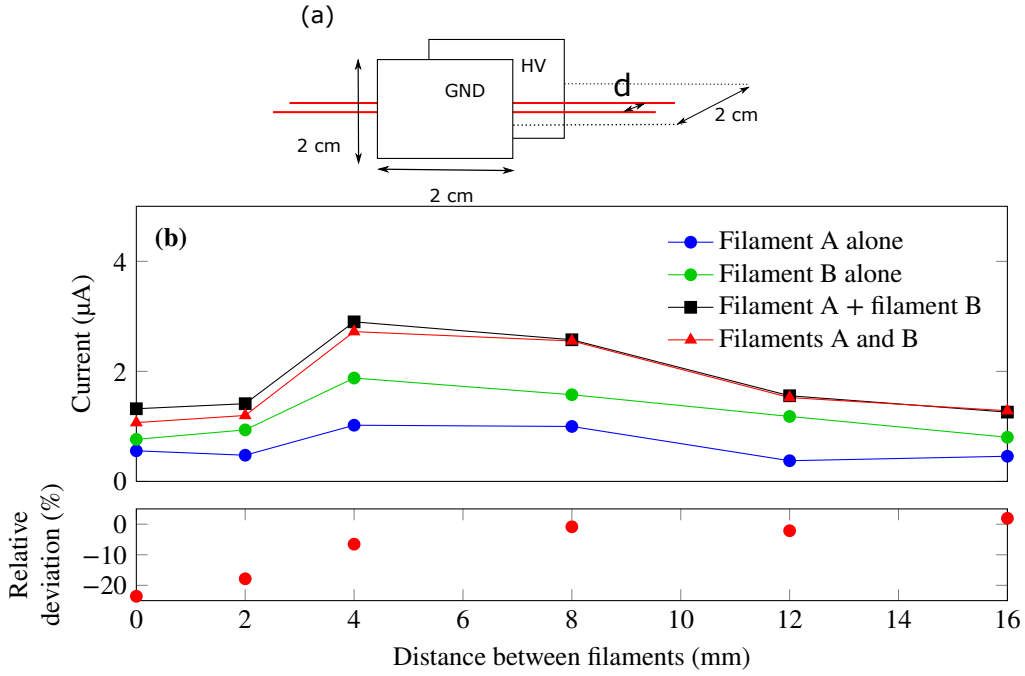

Figure 4.4: Transverse configuration (a) and effect of the distance between the filaments (b) in the transverse configuration for a $5 \cdot 10^5$ kV/m electric field.

investigated by switching to a configuration where the electrodes are perpendicular to the plane containing the two filaments (transverse configuration, see Figure 4.4a). In this configuration, the charges released by each filament screen the other filament from the opposite electrode. The measurement significantly deviates from linearity for short distances between the filaments ($d \leq 4\,\text{mm}$, see Figure 4.4). The error is negative, i.e. the measurement underestimates the ion density by 20 % when both filaments are measured together (A and B), evidencing some screening effect. In contrast, at larger distances, the relative deviation to linearity keeps below 10 %, comparable to the case of the parallel configuration.

In summary, both the total collected charge and the peak current during the long positive swing are representative of the plasma density inside the plasma channel. This could be due to the fact that a larger volume is ionized at high electric fields, keeping the charge density constant but increasing the number of charges collected. This characterization is limited if more than one filament are present in the gap and the distance between them is smaller than a few millimeters or if the filament is closer than a few millimeters to the electrodes. Such situation is for example representative of multiple filamentation, where the typical distance between filaments is in the range of one millimeter according to Petit *et al.* (2011b), Ettoumi *et al.* (2015b) and Mongin *et al.* (2016a). This behavior can now be compared with that of the short polarization peak.

4.2.2 Fast Polarization Signal

The maximum current in the short peak associated with the polarization response is quite linear with the applied electric field (Figure 4.5, parallel configuration). It nevertheless deviates from linearity with respect to the amount of charges by up to 80 % when comparing the signal generated by two filaments with the sum of the signals of each individual filament. This deviation can be explained by the interaction of the two filaments with each other. As discussed at the beginning of Section 4.2, the drift of the free electrons polarizes the medium between the two electrodes during the electron lifetime and induces the collected negative current displayed in Figure 4.2a.

Now if two filaments are propagated between the electrodes, the coupling between them can be expressed as the coupling between two sets of dipoles as the filaments diameters are small as

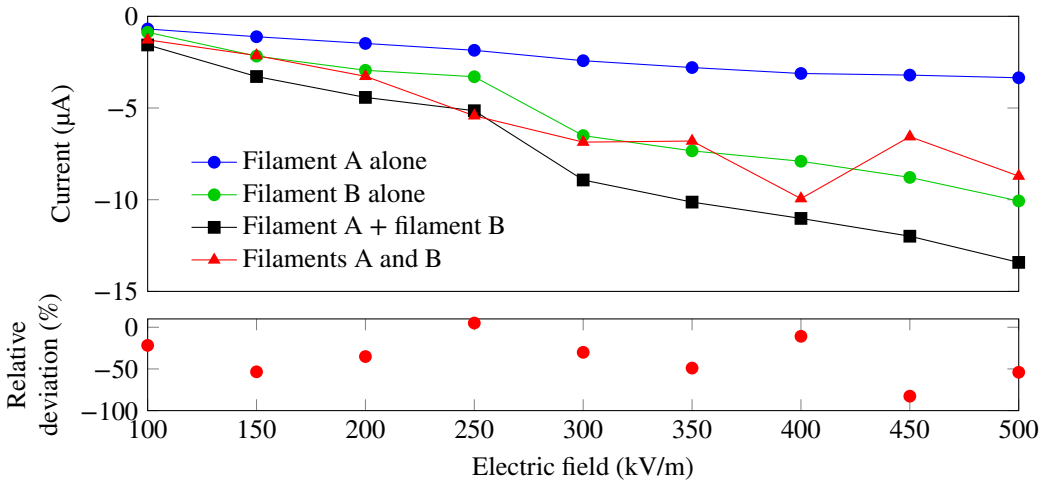

Figure 4.5: Polarization peak current as a function of the applied voltage with $L = 1\,\text{cm}$ and $d = 2\,\text{mm}$ in the parallel configuration (Figure 4.1b).

compared to the distance between them. In the case where the two filaments are in the parallel configuration (Figure 4.1b), the induced electric field E_d on the middle of one filament from the second one is

$$E_d = \frac{-aeN_e(t)}{4\pi\varepsilon_0} x_e(t) \int_{-l/2}^{l/2} \frac{\mathrm{d}z}{\sqrt{d^2+z^2}^3} \tag{4.7}$$

where $l = 2\,\mathrm{cm}$ is the width of the square electrode, a is the filament cross-section and d is the distance between them. E_d can then be inserted in Equation (4.1)

$$x_e(t) = \mu_e(E + E_d)t \tag{4.8}$$

As E_d is in the opposite direction than the electric field from the plates, the second filament reduces the electric field at the place of the first filament and vice versa. For a free electron concentration curve peaking at $3.9 \cdot 10^{21}\,\mathrm{m}^{-3}$, the induced electric field E_d represents 40 % of the $5 \cdot 10^5$ V/m electric field between the electrodes. The new electron position can be replaced in Equation (4.3) to (4.5) and the induced current will be reduced by this dipole interaction. This explains therefore the negative relative deviation in Figure 4.5.

Furthermore, it was observed that the measurement and its linearity are highly sensitive to the distance between the filaments and the electrodes. When the filaments get closer than 5 mm to the electrodes, the polarity of the signal even reverses. This inversion is due to a more efficient collection of the free electrons by the positive electrode as the distance to travel is shorter. This induces a current associated to the electron conduction which overrides the polarization response. Indeed, for an electric field of $5 \cdot 10^5$ V/m (10 kV for a 2 cm gap) and therefore an electronic mobility of $7.6 \cdot 10^{-2}\,\mathrm{m}^2/(\mathrm{Vs})$, it takes around 130 ns for the electrons to travel over 5 mm. Their density at arrival is then of the order of $10^{16}\,\mathrm{m}^{-3}$, five orders of magnitude larger than their density after traveling 1 cm.

4.2.3 Electronic Current Signal

In the case of the longitudinal configuration, where the filaments propagate through the electrodes (see Figure 4.1c), only a short positive signal is observed (see Figure 4.2b). The fact that the

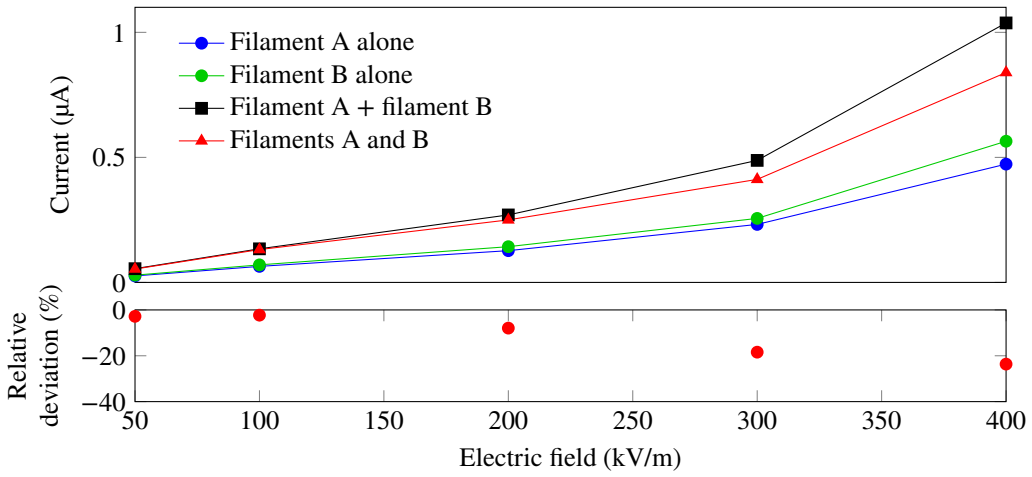

Figure 4.6: Short peak current as a function of the applied external field in the longitudinal configuration (see Figure 4.1c).

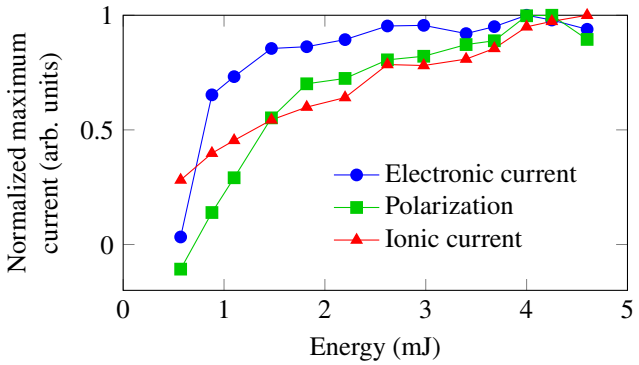

Figure 4.7: Comparison of the three electric signals.

signal is positive here indicates that a flow of charges is indeed measured between the electrodes, and not a polarization response. This signal is mainly attributed to the collection of electrons produced close to the electrodes. No positive swing is observed at long times, due to a more efficient charge neutralization. In contrast to the other configurations, the free charges travel along the same pathway and in opposite directions, increasing the probability for free charges of opposite polarities to meet.

As shown in Figure 4.6, the peak current is quite linear within 2 % error provided the applied electric field stays below 100 kV/m. Conversely, the relative deviation increases up to 19 % for 400 kV/m. This is probably due to the production of secondary electrons by avalanche ionization. The total collected charge behaves similarly.

4.2.4 Comparison of the Three Signals

The respective variation of the three signals can be compared with respect to the beam energy, hence to the ionization increase. These three signals are (1) the maximum ionic current and (2) the maximum current induced by the polarization response in the parallel configuration for a 300 kV/m electric field, as well as (3) the maximum electronic current in the longitudinal direction under a 50 kV/m field. The beam energy was varied between 0.6 and 4.5 mJ and for each energy, the measurement was performed at the propagation distance corresponding to the maximum polarization and ionic signal. The results are displayed in Figure 4.7.

The electronic current in the longitudinal configuration shows a saturation behavior. The first fast rise of the signal corresponds to the increase of the charge density with the beam power and the change of slope for an energy above 1.6 mJ corresponds to the clamping of the filament intensity in its core as described by Kasparian *et al.* (2000). In this case, the remaining slow increase in the signal is due to the higher intensity in the periphery of the filament core, leading to the slight charge increase in this region and therefore to the stronger measured current.

The ionic current increases rather linearly with the beam power. This is surprising as Equation (4.6) shows that ions detected microseconds after the filament formation are almost independent from their initial density if it is higher than 10^{18} m^{-3}. The linear increase measured here could maybe correspond to a linear increase of the isovolume corresponding to this density. Numerical simulations are under progress to better understand this counterintuitive behavior.

Finally, the fast polarization signal seems to evolve as a mixture of the two previous curves, which suggests that ions also contribute to this signal.

4.3 Conclusion

In conclusion, three variants of electric measurements of the free charge density in laser filaments were investigated and compared. Two configurations out of three have been validated as they offer a good linearity with respect to the free charges released in the laser beam.

The longitudinal configuration yields a good linearity when the applied electric field is kept below 100 kV/m, with a deviation lower than 5 %. It shows a saturation behavior with the increase of the beam intensity due to the intensity clamping in the filament. It therefore seems to be the best candidate to measure the initial free electron density in the filament.

On the other hand, measuring either the peak current or the total collected charge in the long positive swing (∼200 µs) on the electrodes parallel to the beam yields a signal insensitive to misalignments, as already put forward by Polynkin (2012). This signal is quite linear with the available free charges but it is difficult to link to the initial electron density in the filament as the ion and electron decay kinetics are very different. This signal should be considered as an indicator of the ionic charge available in the filament, that is the charge after most of the electrons attached to oxygen molecules, rather than as a measure of the initial plasma free electrons. It is interesting to note that the timescale of this signal is in the microsecond range, i.e. the timescale of high-voltage triggering.

Finally, the measurement of the fast polarization signal leads to relative deviations on the linearity of charge quantity up to 80 %, consistent with the measurements of Abdollahpour *et al.* (2011). This is therefore not a good measurement when one aims to investigate the free charge density in a filament but it is still a semi-qualitative indication of the presence of charges, hence a valid way to characterize the filament length.

This study should clarify the controversy about ionization measurement techniques in the context of laser filamentation and help experimentalists choose the most relevant approach to perform accurate measurements of free charges in laser-induced plasma channels.

In the next chapter, the partitioning of laser pulses into multiple sub-pulses and its impact on air ionization will be investigated.

Optimal Laser Pulse Energy Partitioning for Air Ionization 5

The plasma filament probing techniques detailed in the previous chapter will now be applied to the optimization of plasma production by laser filaments.

Optimizing the discharge triggering efficiency of laser filaments requires to maximize both the laser ionization yield and the free electron lifetime, which can be improved by heating the surrounding gas. Using sequences of multiple pulses has been shown to be relevant in this purpose, in the case of LIBS Sattmann *et al.* (1995), laser ablation in solids (Chichkov *et al.*, 1996, Vorobyev & Guo, 2005) or dielectrics (Jasapara *et al.*, 2001) and such effort is especially relevant in the case of laser filamentation.

Multiple pulses can increase the ionization yield and free electron lifetime through different processes, such as avalanche ionization, photo-detachment of electrons from O_2^- ions or by heating the plasma created by the first pulse with one or more subsequent pulses as shown by Wang *et al.* (2011), Shen (1984), Burch *et al.* (1958) and Polynkin & Moloney (2011). However, most results reported to date investigate the effect of adding one or several subsequent pulses to a main pulse. Such addition of energy can only result in an increase of the observed effect. Méjean *et al.* (2006), Diels & Zhao (1992), Papeer *et al.* (2014), Polynkin & Moloney (2011) and Zhou *et al.* (2009) showed for example that launching a frequency-doubled YAG pulse of 7 ns duration at 532 nm together with a near-infrared (800 nm) pulse significantly increased the probability of triggering a discharge over 1.2 m, lowering the median breakdown voltage by at least 5 %. Alternatively, Lu *et al.* (2015) reported that a 60 ns long sequence of over 30 pulses, with a total energy of 120 mJ, maintains the ionization over a duration comparable to the sequence itself, each pulse interacting more or less independently with the plasma.

In contrast to those experiments, one can consider a laser system with a fixed total energy and optimize the ionization with an optimal temporal partitioning of the pulse energy. This optimization is in particular characterized by the relative energy splitting and the delay(s) between sub-pulse(s) in a train of pulses. Although this has already been well investigated for nanosecond pulses with microsecond inter-pulse delays by Sattmann *et al.* (1995), only one specific situation has been investigated for ultrashort pulses. Zhang *et al.* (2009) have shown that splitting a 30 mJ, 30 fs pulse into two sub-pulses separated by 7 ns decreased the ionization measured by acoustic signal and had no impact on the pulse ability to guide electric discharges.

In this chapter, an ultrashort laser pulse of several millijoules is split into a pulse train of two to four sub-pulses with arbitrary relative intensities and delays and the resulting plasma ionization yield and lifetime is studied. Furthermore, numerical simulations show that at a higher energy allowing multiple filamentation, a sequence of filamenting sub-pulses increases the temperature of the heavy species as compared to the bundle of multiple filaments with the same energy. This could improve the efficiency of discharge triggering.

My contribution to the present work has been to contribute preparing the equipment and

experimental setup and to record and treat the data. This work was published in Schubert *et al.* (2016a).

5.1 Material and Methods

The chirped pulse amplifier laser system used for this experiment delivers 450 fs FWHM pulses at a central wavelength of 1030 nm, the gain medium being an Yb:CaF_2 crystal. The spectral bandwidth is 5 nm broad and pulses are delivered at 10 Hz repetition rate. The total output energy of the system is 6.3 mJ and the beam has a diameter of 6 mm.

As sketched on Figure 5.1, the energy can be split between one to four pulses with arbitrary amplitude ratios and tunable delays between the pulses over a range of 10 ns, limited by the length of the regenerative amplifier cavity. This is achieved by splitting the oscillator out-coming pulse into multiple pulses by a series of tunable passive beam splitters. The pulses are then recombined and amplified in the regenerative amplifier. The development of this multi-pulse laser was realized by J.-G. Brisset during his PhD thesis at Amplitude Systèmes in Bordeaux (FR). The peak power obtained is 13.7 GW, above the 7 GW critical power for filamentation at this wavelength mentioned by Kasparian *et al.* (2000) and Bergé *et al.* (2007). To help self-focusing and to keep the focus at the same position independently of the energy of the individual pulses, a $f = 50$ cm lens is added after the laser amplifier.

To measure the effect of the laser filament on conductivity, two 2.5 cm × 2.5 cm square electrodes were placed in the beam, with holes allowing the beam to propagate through the center of the plates without touching the electrodes (similar setup than the longitudinal configuration from Figure 4.1c). One electrode is connected to a DC HV power supply that provides up to 25 kV. A capacitor with $C = 150$ pF is placed in parallel to the HV power supply to act as a charge reservoir. The other electrode is placed 1 to 3 cm apart from the first one, centered on the filamenting region and grounded. A resistance with $R = 15\,\Omega$ is placed in series to probe the current flowing from the electrode to the ground. A DPO 7254C 2.5 GHz bandwidth oscilloscope is used to record the signal. The recording is triggered with a photodiode aiming at the beam dump after the electrodes and the data have been analyzed using MATLAB.

The time-integrated measured intensity, i.e. the total collected charge, is proportional to its maximum value when the electrodes are 1 cm apart, which ensures that the initial charge of the capacitor is only marginally depleted. This means the measurements are indeed representative of the air ionization in the plasma, and the measurements do not impact the measured plasma

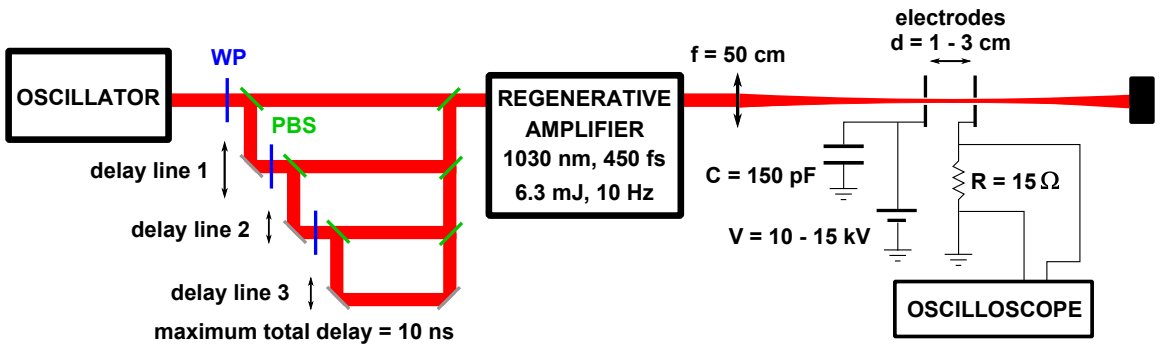

Figure 5.1: Experimental setup. blue WP: half-wave plate; green PBS: polarizing beam splitter.

lifetime. It must be noted that when the electrodes are 3 cm apart, this proportion is less clear. In the following, the maximal value of the signal has been taken as a measurement of ionization.

The free electron lifetime was defined as the longest time interval over which the electron density was kept over $1.6 \cdot 10^{20}$ m^{-3}. According to Ihaddadene & Celestin (2015), this threshold density is typical of that of a leader. The lifetime corresponds to the typical interval over which the plasma left behind by the laser would have a substantial influence on the atmospheric electricity behavior. One may note that this threshold is equivalent to 10 % of the peak value for a single pulse containing the full 6.3 mJ energy of the laser.

5.1.1 Modeling

In order to better understand the observed results, the evolution of the plasma under multiple pulse illumination was modeled. The evolution of the electrons density is driven by (Zhao *et al.*, 1995, Fernsler *et al.*, 1979)

$$\frac{\mathrm{d}N_e}{\mathrm{d}t} = R_{\mathrm{col}} + R_{\mathrm{av}} + R_{\mathrm{ion}} - R_{\mathrm{ep}} - R_{\mathrm{at}} + R_{\mathrm{pd}} \tag{5.1}$$

where

$$\begin{aligned}
R_{\mathrm{col}} &= \alpha N_e && (5.2)\\
R_{\mathrm{av}} &= \frac{1}{\omega_0^2\tau^2+1}\frac{q_e^2\tau}{c\varepsilon_0 m_e U_{\mathrm{p,O_2}}} I_L N_e && (5.3)\\
R_{\mathrm{ion}} &= N_{\mathrm{Mol}} W(I_L) && (5.4)\\
R_{\mathrm{ep}} &= \beta_{ep} T_e^{-0.7} N_e N_p && (5.5)\\
R_{\mathrm{at}} &= (\eta_2+\eta_3) N_e && (5.6)\\
R_{\mathrm{pd}} &= \frac{N_n \sigma_{\mathrm{O_2^-}} I_L}{\hbar\omega_0} && (5.7)
\end{aligned}$$

and $W(I_L)$ describes the probability of ionization calculated with the Perelomov, Popov, & Terent'ev (1966) (PPT) formula and I_L is the incident laser intensity. The terms in Equation (5.2) to Equation (5.7) account for collision ionization, avalanche ionization, probability of ionization, electron-ion recombination, attachment and photo-detachment respectively. In the collision ionization term, $\tau = 1/\nu_{en} = \left(10^{-13} N_{\mathrm{Mol}} \sqrt{T_{e,[\mathrm{eV}]}}\right)^{-1}$ is the inverse of the electron-neutral molecule collision frequency and the collision ionization rate α given by Fernsler *et al.* (1979) displays a very fast rise as a function of the temperature. All parameters are summarized in Table 5.1. According to (Zhao *et al.*, 1995), two- and three-body electron attachment to oxygen molecules respectively occur at rates

$$\begin{aligned}
\eta_2 &= 1.22 \cdot 10^8 \frac{N_{\mathrm{Mol}}}{N_0} \exp\left\{-\frac{42.3}{E_{\mathrm{at}}}\right\} && (5.8)\\
\eta_3 &= 10^8 \left(\frac{N_{\mathrm{Mol}}}{N_0}\right)^2 \frac{0.62 + 800E_{\mathrm{at}}^2}{1 + 1000E_{\mathrm{at}}^2\left[E_{\mathrm{at}}(1+0.03E_{\mathrm{at}}^2)\right]^{1/3}} \cdot \frac{T_{0,[\mathrm{eV}]} e^{\frac{0.052}{T_{0,[\mathrm{eV}]}}}}{T_{e,[\mathrm{eV}]} e^{\frac{0.052}{T_{e,[\mathrm{eV}]}}}} && (5.9)
\end{aligned}$$

where $E_{\mathrm{at}} = 3.34 \cdot 10^{-5} E/(N/N_0)$.

Similarly, the evolution of positive and negative ion densities are derived from Zhao *et al.* (1995) and Fernsler *et al.* (1979)

$$\frac{\mathrm{d}N_p}{\mathrm{d}t} = R_{\mathrm{col}} + R_{\mathrm{av}} + R_{\mathrm{ion}} - R_{\mathrm{ep}} - \beta_{np} N_n N_p \left(\frac{T_g}{T_0}\right)^{-1.5} \tag{5.10}$$

$$\frac{\mathrm{d}N_n}{\mathrm{d}t} = R_{\mathrm{at}} - R_{\mathrm{pd}} - \beta_{np} N_n N_p \left(\frac{T_g}{T_0}\right)^{-1.5} \tag{5.11}$$

The last term in Equation (5.10) and (5.11) accounts for ion-ion recombination, where T_g is the temperature of the heavy species and T_0 the ambient temperature of 300 K.

The total electron thermal energy evolves under Joule heating by the laser field and the external DC field, energy exchanges with the heavy species and the vibrational energy of air molecules, the excess energy in the ionization and photo-detachment processes, losses of kinetic energy due to collision and avalanche ionization, electron losses related to electron-ion recombination, attachment and transfer to molecules via impact excitation and is derived from Fernsler *et al.* (1979) and Papeer *et al.* (2014)

$$\begin{aligned}\frac{\mathrm{d}T_e}{\mathrm{d}t} &= \frac{2J_L}{3N_e k_B} + \frac{2q_e\mu_e E^2}{3k_B} - (T_e - T_v)\nu_{ev} - 2(T_e - T_g)\frac{m_e \nu_c}{M_{\mathrm{air}}} \\ &+ \left[R_{\mathrm{ion}} U_e + R_{pd} U_{e_{O_2^-}} - \left(R_{\mathrm{col}} + R_{\mathrm{av}}\right) U_{\mathrm{O_2}}\right] \cdot \frac{2}{3k_B N_e} \\ &- [R_{\mathrm{ep}} + (\eta_2 + \eta_3)]T_e - \frac{2N_{\mathrm{Tot}}}{3k_B} R_{\mathrm{imp}}\end{aligned} \tag{5.12}$$

where

$$R_{\mathrm{imp}} = k_{\mathrm{N_2,A}} U_{\mathrm{N_2,A}} + k_{\mathrm{N_2,B}} U_{\mathrm{N_2,B}} + k_{\mathrm{N_2,C}} U_{\mathrm{N_2,C}} + k_{\mathrm{O_2,a}} U_{\mathrm{O_2,a}} + k_{\mathrm{O_2,b}} U_{\mathrm{O_2,b}} \tag{5.13}$$

and μ_e is the electron mobility (Zhao *et al.*, 1995)

$$\mu_e = -\frac{N_0}{3N_{\mathrm{Tot}}} \left(\frac{5 \cdot 10^5 + E_0}{1.9 \cdot 10^4 + 26.7 \cdot E_0}\right)^{0.6} \left[\frac{\mathrm{m}^2}{\mathrm{V \cdot s}}\right] \tag{5.14}$$

N_0 being the molecule density at 1 atm and $E_0 = EN_0/N_{\mathrm{Tot}}$, as seen in Chapter 4.

The heating rate is given by Papeer *et al.* (2014)*

$$J_L = \frac{4\pi q_e^2 N_e \nu_{\mathrm{ei}}}{m_e c \varepsilon_0 \left(\omega_0^2 + \nu_{\mathrm{ei}}^2\right)} I_L \tag{5.15}$$

Similarly, the vibration and kinetic temperatures of the heavy species evolve as

$$\frac{\mathrm{d}E_v}{\mathrm{d}t} = \frac{3}{2} N_e k_B (T_e - T_v)\nu_{ev} - \frac{E_v - E_{v,0}}{\tau_{VT}} \tag{5.16}$$

$$\frac{\mathrm{d}T_g}{\mathrm{d}t} = 2(T_e - T_g)\frac{m_e \nu_c N_e}{M_{\mathrm{air}} N_{\mathrm{Tot}}} + \frac{2(E_v - E_{v,0})}{3\tau_{VT} k_B N_{\mathrm{Tot}}} \tag{5.17}$$

*Note that an ε_0 is missing in their definition of the Ohmic heating J_L on p. 7 of their work.

where the vibrational energy is given by Shneider *et al.* (2011)

$$E_v = \frac{N_{\mathrm{Tot}}(\hbar\omega_{\mathrm{vib,N_2}})}{\exp\left(\frac{\hbar\omega_{\mathrm{vib,N_2}}}{k_B T_v}\right) - 1} \tag{5.18}$$

and $E_{v,0}$ is its value for $T_v = T_0$, where T_0 is the ambient temperature. The cooling frequency ν_{ev} is given by Papeer *et al.* (2014)

$$\nu_{ev} = \frac{Q_c N_{\mathrm{Mol}}}{1.5 k_B T_e} \tag{5.19}$$

The electron-heavy species collision rate is the sum of the electron collision rates with molecules and positive ions (Papeer *et al.*, 2014)

$$\nu_c = 10^{-13} N_{\mathrm{Mol}} \sqrt{T_{e,[\mathrm{eV}]}} + 10^{-11} N_p T_{e,[\mathrm{eV}]}^{-1.5} \tag{5.20}$$

Finally, the vibrational-translational relaxation time τ_{VT} is given by Shneider *et al.* (2011)

$$\tau_{VT} = \left[N_{\mathrm{Mol}} \cdot \left(7 \cdot 10^{-16} \exp\left(-\frac{141}{T_g^{1/3}} \right) + 0.21 \cdot 5 \cdot 10^{-18} \exp\left(-\frac{128}{T_g^{0.5}} \right) \right) \right]^{-1} \tag{5.21}$$

Hydrodynamics as well as the spatial dynamics induced by the external DC field are not considered in this modeling.

5.2 Results and Discussion

5.2.1 Experiments

The impact of trains of three to four laser sub-pulses on the conductivity between the electrodes has been investigated at first. On Figure 5.2, the laser effect of a three-pulses laser train is shown and the laser sub-pulses relative intensities and temporal spacing are depicted in red. The pulse

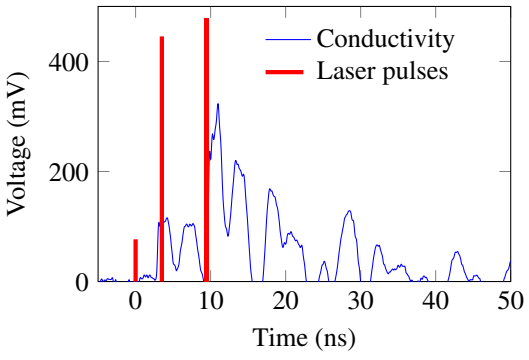

Figure 5.2: Train of three laser sub-pulses and its conductivity response. The laser pulse temporal spacing and relative intensity are depicted in red.

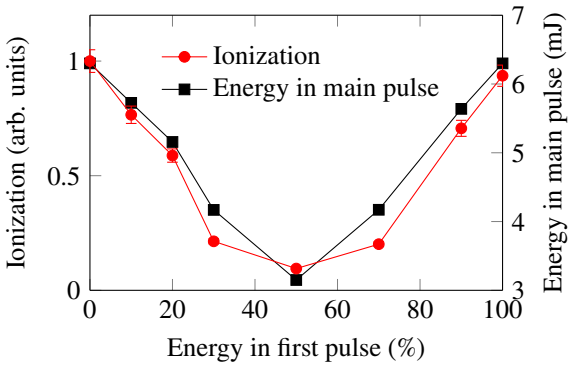

Figure 5.3: Effect of energy partitioning on the ionization yield. The delay between the two sub-pulses is 4 ns and the electrode gap is 3 cm.

Table 5.1: Notations and parameters of the model.

Symbol	Meaning	Value	Reference
α	Collision ionization coeff.		F. 1979
$W(I_L)$	Probability of ionization		P. 1966
k_B	Bolzmann's constant	$1.38 \cdot 10^{-23}$ J/K	
ω_0	Laser frequency		
I_L	Incident laser intensity		
T_0	Ambient temperature	300 K	
$T_{0,[eV]}$	Ambient temperature in eV	0.026 eV	
M_{air}	Average mass of air molecules	$4.7704 \cdot 10^{-26}$ kg	
N_0	Density of molecules (normal conditions)	$2.688 \cdot 10^{25}$ m^{-3}	
q_e	Electron charge	$1.6 \cdot 10^{-19}$ °C	
m_e	Electron mass	$9.1 \cdot 10^{-31}$ kg	
$\sigma_{O_2^-}$	Photodetachment cross section of O_2^-	$3.8 \cdot 10^{-23}$ m^2	B. 1958
β_{ep}	Electron-ion recombination coefficient	$1.138 \cdot 10^{-11}$ m^3/s	Z. 1995
β_{np}	Ion-ion recombination coefficient	$2.1792 \cdot 10^{-13}$ m^3/s	Z. 1995
η_2	2-body attachment coefficient	See Equation (5.8)	Z. 1995 & F. 1979
η_3	3-body attachment coefficient	See Eq. Equation (5.9)	F. 1979
$\hbar\omega_{\text{vib},N_2}$	Quantum of vibration of N_2	0.29 eV ($4.64 \cdot 10^{-20}$ J)	S. 2010
$U_{N_2,A}$	Energy of the $N_2(A^3_\Sigma)$ state	6.2 eV	F. 1979, p. 13
$U_{N_2,B}$	Energy of the $N_2(B^3_\pi)$ state	7.35 eV	V. 1997
$U_{N_2,C}$	Energy of the $N_2(C^3_\pi)$ state	11 eV	C. 1977
$U_{O_2,a}$	Energy of the $O_2(a^1_\Delta)$ state	1 eV	F. 1979, p. 14
$U_{O_2,b}$	Energy of the $O_2(b^1_\Sigma)$ state	1.6 eV	F. 1979, p. 14
k_X	Electron impact excitation to state X rate	F. 1979, Table II	F. 1979, p. 14
E	External DC field	10–14 kV	
μ_e	Electron mobility	See Equation (5.14)	Z. 1995
N_{Tot}	Heavy species density (initial molecule density)	$2.5 \cdot 10^{25}$ m^{-3}	
N_{Mol}	Neutral molecules density		
T_e	Electron temperature		
$T_{e,[eV]}$	Electron temperature in eV		
T_g	Heavy species temperature		P. 2014
T_v	Heavy species vibrational temperature		P. 2014

train consisted of a first pulse holding 7 % of the total energy; after 3.5 ns, a second pulse holding 44 % of the total energy was sent and finally the remaining 48 % energy were sent 6 ns later. The laser impact is clearly visible for the second and third laser sub-pulse. Although some conductivity is measurable when the laser energy is divided in three sub-pulses, the intensity reached is very close to the ionization threshold as the energy is insufficient to create a filament. Therefore, no analysis was performed on the data taken with three and four laser sub-pulses and the results will focus on the difference between one single pulse and two sub-pulses of variable intensities and delays between them.

As displayed on Figure 5.3, partitioning the pulse energy into a dual pulse reduces the ionization yield, regardless of the delay. In the power range of this experiment, the peak density of free electrons is governed by the power of the stronger pulse without significant contribution from the weaker one, that does not contain enough power to create a filament. The main action of the weaker pulse is to slightly heat up the gas. The small error bars were estimated from the variability of the electron yield with full laser power over a whole day. They are mainly due to the environmental changes in the laboratory (relative humidity and temperature) and to laser fluctuations.

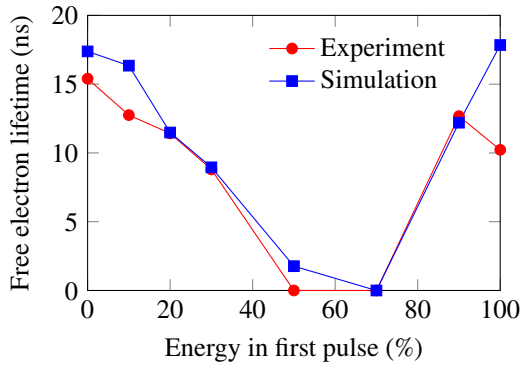

Figure 5.4: Free electron lifetime when excited by a double pulse (0.5 ns delay), as a function of the relative intensity between the two pulses, in a 3 cm gap under 15 kV.

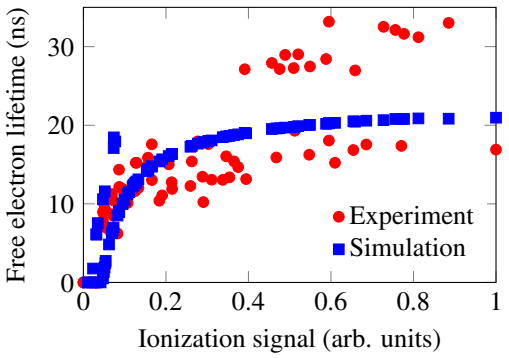

Figure 5.5: Free electron lifetime as a function of their initial density. The red dots are the experimental data points and the blue squares the simulation.

At energies below 3 mJ, the beam remains below the critical power, so no filamentation occurs any more and the intensity decreases. As the ionization is highly non-linear, the electron yield drastically drops below the detection threshold.

The effect of the pulse partitioning on the free electron lifetime (Figure 5.4) is to a large extent governed by the drop in the initial electron density, that results in hitting faster the streamer threshold. The asymmetry in the curve is due to the electron density threshold used to determine the free electron lifetime and to the second pulse being only 0.5 ns after the first one. At the energy levels measured here, this asymmetry disappears for delays between the pulses longer than 1 ns. Similar results are obtained over the whole range of investigated pulse delays, i.e. between 0.5 and 9.5 ns and for both electrode gaps (1 cm, 10 kV and 3 cm, 15 kV).

The photo-detachment and re-ionization by the second pulse do not compensate the less efficient ionization, as evidenced on Figure 5.5 where each point represents the data measured or simulated in one experimental condition, i.e. for a given energy ratio and delay between the pulses. The set of points covers all the energy ratio from 1:0 to 0:1 and delays from 0.5 to 9.5 ns. The bifurcation appearing close to zero ionization signal in the simulated data is an artifact due to the absolute threshold used to determine the free electron lifetime. Monitoring the contribution of the photo-detachment and re-ionization during the simulations confirm this interpretation. Furthermore, with an energy limited to a few mJ, the second pulse does not significantly heat the plasma.

More specifically, this free electron decay is governed by both electron attachment to oxygen molecules and electron recombination. The attachment rate is typically 23 ns, independent from the initial electron density as the reservoir of oxygen molecules is virtually infinite for the electron densities at play ($<2 \cdot 10^{15}$ cm^{-3}). This attachment rate, that strongly depends on temperature, is consistent with the values of a few tens of nanoseconds put forward by Zhao *et al.* (1995).

In contrast, recombination depends quadratically on the ionization yield. Its contribution increases for larger initial electron densities, and therefore reduces their lifetime. The typical recombination time amounts to 380 ns for an initial electron density of $2 \cdot 10^{13}$ cm^{-3}. Under these conditions, recombination is negligible. In contrast, the recombination time drops down to 10 ns for the highest initial electron densities relevant to this experiment ($1.6 \cdot 10^{15}$ cm^{-3}).

This competition between recombination and attachment also gives an estimate of the absolute

electron density in the experiment: an average free electron decay time of 7 ns at $1/e$ for a single pulse corresponds to $1.6 \cdot 10^{15}$ electrons/cm^3.

5.2.2 Simulations

As the laser intensity is a very sensitive parameter in the simulations, it can not be determined with sufficient accuracy from the laser energy and beam geometry, nor from numerical simulations of the pulse propagation. Therefore, the experimental conductivity data is used to calibrate it. This calibration of the electron density is used to evaluate the incident pulse intensity I_L for each pulse energy by inverting Equation (5.1) for the duration of the pulse. Based on this calibration, the model reproduces well the experimental data (Figure 5.4 and Figure 5.5).

Furthermore, the simulation illustrates the effect of splitting the pulse energy in the experiments. Figure 5.6a compares the simulated free electron lineic density for one single filamenting 6.3 mJ pulse and two 3.15 mJ sub-pulses. As observed in the experiment, splitting the energy in two pulses delayed with 3 ns only decreases the available electron density. On the other hand, increasing the total energy to 12.6 mJ by sending two pulses of each 6.3 mJ increases more than twice the electron density than for the single pulse and the free electron lifetime is approximately doubled, as observed by Polynkin & Moloney (2011). Figure 5.6b shows the gas temperature along the laser beam propagation axis for the same conditions. As for the free electron density, as soon as the energy in a pulse is sufficient to create a filament, the temperature rises significantly. As the heavy species have a long vibrational relaxation time, the gas temperature stays high for a very long time and leads to an expansion of the gas. This in turn allows the free electrons to travel unperturbed on a longer distance, increasing the discharge triggering efficiency as discussed by Vidal *et al.* (2000) and Papeer *et al.* (2014).

After validating the model against the experimental data at low energies, the model is used

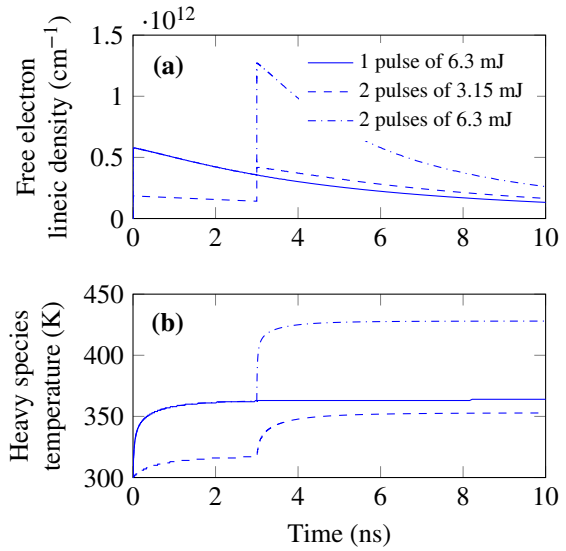

Figure 5.6: Free electron lineic density (a) and heavy species temperature (b) reached with respect to time for one laser pulse of 6.3 mJ or two laser pulses of respectively 3.15 and 6.3 mJ each.

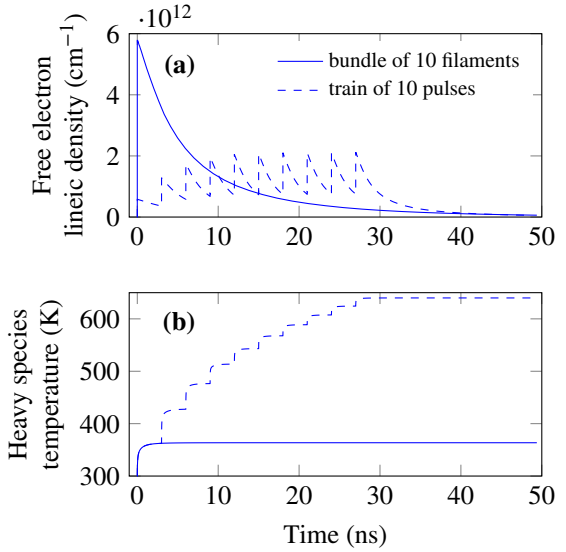

Figure 5.7: Free electron lineic density on the beam propagation axis (a) and heavy species temperature (b) with respect to time for a bundle of 10 filaments and a train of 10 sub-pulses spaced with 3 ns of 63 mJ total energy.

to investigate how the partitioning effect evolves for higher total energies. In particular, the simulations are performed with enough energy to create ten filaments that can be split either in time (train of pulses) or in space (multiple filaments bundle). Figure 5.7 shows the free electron lineic density created by a bundle of ten filaments and for a train of ten filaments with 3 ns delay between them and the corresponding gas temperature increase. As this work is dealing with atmospheric applications of laser filaments, the case of a collimated or loosely focused beam was considered. In this case, the individual filaments of the multiple filamentation pattern have similar properties, including ionization level, than a single filament as discussed by Chin *et al.* (2005), Couairon & Mysyrowicz (2007) and Bergé *et al.* (2007). This would not hold in the case of tightly focused beams, where the ionization and the energy deposition increases (see Théberge *et al.*, 2006, Point *et al.*, 2016). Such situation would require to include a detailed simulation of the propagation in three dimensions, which is well beyond the scope of this work.

It is very clear from Figure 5.7a that a bundle of filaments creates less free electrons at a given time but the free electron density is always higher than that of a single filament. The free electron lifetime is governed by the successive re-ionizations and is therefore comparable to the length of the pulse train. On the other hand, each sub-pulse creating one filament is depositing energy in the same parcel of gas, increasing its temperature, whereas the bundle of filaments deposits much less energy per unit volume in the gas. Therefore, a train of pulses with sufficient energy in each pulse to create a filament can be expected to be more favorable to trigger an electrical discharge, as the free electron density created is high and the streamer can propagate on longer distances thanks to the air rarefaction due to the heavy species temperature increase and their longer lifetime.

Note that a more precise evaluation of this effect would need to consider the cross-pulse influence via the ionization left behind by the pulses. For example, long pulses will influence the propagation of the subsequent pulses as shown by Béjot *et al.* (2011) but this is beyond the scope of this work.

5.3 Conclusion

As a conclusion, partitioning the energy of an ultrashort laser pulse of 6.3 mJ, 450 fs into trains of two to four pulses decreases the free electron yield. This is due to the high non-linearity of the ionization process that overrides plasma heating effects as well as photo-detachment and photo-ionization at low laser intensities. Accordingly, the plasma lifetime during which it keeps above the typical electron density of a leader decreases.

Trains of pulses are nevertheless efficient to increase the free electron lifetime if each sub-pulse carries enough energy to initiate a filament. Also, as the pulse trains are very efficient to heat the heavy species, this leads to a longer electron mean free path, which should help triggering electric discharges by allowing more electrons to travel along the streamer channel.

These results provide valuable information to dimension and optimize the pulse shape of future systems aimed at triggering high-voltage discharges and guiding them, especially over large scales.

In the following, the interactions of high-voltage electric discharges with laser filaments will be investigated.

Interactions of Laser Filaments with DC High-Voltage Sources 6

As discussed in the two previous chapters, lasers filaments being electrically charged, they can interact with an electric field applied between two electrodes. Already in 1974, Ball suggested that laser beams could be used as lightning rods (Ball, 1974).

According to Curran *et al.* (2000) and U.S. National Weather Service (2016), around 500 people get injured or killed due to lightning events in the USA each year and losses amount to over a bilion dollars per year, including e.g. forest fires, breakdown of electrical networks and aircraft damages. Therefore, preventing lightning damages is a very important topic. Since Benjamin Franklin invented the lightning rod in 1749, scientists have tried to improve his invention and find better ways to protect sensitive constructions from lightning. While the lightning rod itself was improved and is still the major protection for buildings in the world, it is not 100 % efficient (Gary, 2004, Rizk, 2010). Due to the ambient electric fields preceding a lightning strike, free charges – also called space charges or corona – can accumulate at the top of the lightning rod and shield it from the lightning strike. The strike can then hit within the area that is supposed to be protected by the rod (Bazelyan & Raizer, 2000a).

The rise of sensitive electronic systems asked for better protection of infrastructures. Indeed, a lightning rod on top of a building will protect it from direct effects of lightning, i.e. from burning down. It will however not shield the inside of the building from the indirect effects of the strong electromagnetic fields of the discharge that will cause damage to electronics within the building. The over-voltage level in a building stroke by lightning will be almost the same than for an unprotected one. Therefore, attracting the lightning strike with a rod is even counter-productive as the probability of getting hit by the strike is increased by the presence of the rod. Also, planes, as it can be expected, can not be grounded. The newer plane generations built with composite materials replacing most of the metal shield are poor Faraday cages while electronic commands sensitive to electromagnetic fields have replaced the mechanical ones in the cockpit.

One method to protect sensitive sites like airports, power plants, refineries, etc. is to divert the lightning strikes to another location. Since the 1960s, rockets followed by a grounded cable have been used to trigger lightning for experimental purposes. A rocket followed by a grounded conducting cable is sent towards a storm cloud at around 50 to 500 m from the ground to trigger a lightning strike that will follow the cable instead of hitting the ground at a random position. This technique needs a good experience from the rocket operator as if it is sent too early, no triggering will occur whereas if it is sent too late, a natural strike could occur. Also, one rocket can at most trigger one lightning strike (Gary, 2004).

Since it was discovered that high intensity laser beams could ionize the air and create a conductive plasma channel on their propagation path, scientists have tried replacing rockets by laser beams. Before the invention of ultrashort laser pulses, Koopman & Wilkerson proved already in 1971 that a high-power neodymium laser beam at 1 µm could guide an electrical

discharge (Koopman & Wilkerson, 1971). They guided the discharge over a distance up to 28 cm in a total electrical breakdown of 71 cm generated by a pulsed high-voltage Marx generator providing 350 kV at a total energy storage of 130 J. Miki *et al.* (1993) demonstrated that high-power 45 J CO_2 laser beams at 10 µm could produce "plasma beads" that could guide an electrical discharge over a 2 m gap between electrodes charged by an impulse generator providing 1 MV and a total 5 kJ energy storage. Uchida *et al.* (1999) and Apollonov *et al.* (2002) also showed that a high-power CO_2 laser beam at 10 µm, combined with other lasers in the case of Uchida *et al.* (1999), with energies in the Joule to kilojoule range could be used to improve guiding of lightning from clouds, respectively in field experiments or in a laboratory study with the artificial production of a charged cloud.

Bazelyan & Raizer (2000b) remind in their review that the high energies involved with such lasers allow to heat up significantly the air when focused to under a few meters. This reduces the gas density N_{Tot} along the beam path and therefore increases the collisional ionization by electrons, whose rate constant is controlled by the reduced field E_0/N_{Tot}. It also reduces the electron losses due to attachment and recombination of electrons with ions and altogether allows the triggering and guiding of electrical arcs by increasing the path conductivity via Paschen's law (Tirumala & Go, 2010).

The efficiency of this effect drops however for looser beam focusing as the density of deposited energy is much lower. The laser energies needed to trigger discharges with long laser pulses is tremendously important and the high density of plasma produced by those nanosecond high-power pulses is opaque to the laser light, which leads to a discontinuous chain of plasma beads. The invention of ultrashort laser pulses greatly improved the relevance of such techniques as the lower plasma density (typically $10^{20}-10^{23}$ m^{-3}) created by the sub-nanosecond pulses allowed the creation of continuous plasma channels a few hundred meters long (Durand *et al.*, 2013).

Comtois *et al.* (2000), La Fontaine *et al.* (2000), Rodríguez *et al.* (2002) and Gordon *et al.* (2003) among others showed that femtosecond near-infrared laser pulses could guide and even trigger electrical discharges over a few meters and that the electrical breakdown occurred at electric fields 30 % lower with the ultrashort laser beam as compared to the natural breakdown threshold. On the other hand, Zhao *et al.* (1995), Bazelyan & Raizer (2000b), Rambo *et al.* (2001) and Ionin *et al.* (2012), motivated by the much higher multi-photon ionization rate at shorter wavelengths, investigated the impact of ultraviolet laser filaments on electrical breakdown triggering and guiding, as it will be discussed in detail in Section 1.1.3. Laser filaments have also been used as a probe to investigate the dynamics of high-voltage discharges (Sugiyama *et al.*, 2009, 2010), streamers (Wang *et al.*, 2015) and leaders (Eto *et al.*, 2012, Schmitt-Sody *et al.*, 2015). Finally, Théberge *et al.* (2017) and others investigated recently the laser-induced plasma lifetime increase when coupling DC voltage sources to AC voltage sources.

Triggering lightning ultimately implies collecting the discharge by means of a classical lightning rod, with an adequate design and/or location to avoid indirect effects of lightning in the vicinity of the impact location. In contrast, preventing electrical arc breakdown by remotely unloading thunderclouds may offer a more efficient protection. In this chapter, after a short reminder of lightning mechanisms, it is demonstrated that laser filaments can neutralize DC high-voltage electrodes while preventing electrical arcs, even remotely. The remote unloading ability of laser filaments are then investigated in detail under conditions without any electrical breakdown. I personally contributed to the work presented in this chapter by designing the setup, collecting and processing the data. This work was published in Schubert *et al.* (2015) *, except for Section 6.2.3,

*A new explanation of the charge neutralization and arc suppression mechanisms is presented at the end of this

6.3.4 and 6.3.5, which are still unpublished.

6.1 Electrical Breakdown Steps

Townsend (1900) presented the first understanding of a mechanism important for the electrical arc propagation, that is the so-called *avalanche ionization*. In his case, a first electron is ejected from a cathode by a cosmic ray. This electron is accelerated between the cathode and the ground by the external electric field and ionizes an air molecule. If the field is sufficiently high, the new electron will in turn ionize more molecules and therefore the name of electron avalanche given to this phenomenon. The cloud of free charges created by the avalanche ionization is called *corona* and can be seen as a blueish glow forming for example at the tip of an electrode and flowing in direction of the opposite sign electrode. The avalanche ionization is however not sufficient to explain the electrical breakdown between two charged electrodes. Indeed, in this framework, lightning would only occur at electric fields as high as 3 MV/m whereas typical static electric fields at the ground level are more in the 10–15 kV/m according to Gary (2004).

Loeb (1936) and Meek (1940) then proposed that the electrons generated in the avalanche ionization distorted the electric field between the electrodes, allowing the ionization process to occur in lower external electric fields. This propagation was called a *streamer* propagation, where the streamer is an ionized channel forming in the corona cloud generated by the avalanche ionization. The fast attachment of free electrons to O_2 molecules in the streamer keeps the charge density relatively low, in a regime called *cold ionization*. The temperatures in this region are between 300 and 1500 K.

When the current in the streamer increases in the vicinity of a charged object, the streamer channel is heated by enery dissipation of charges in movement. When the temperature reaches 1500 K, the detachment rate becomes equal to the attachment rate of electrons to O_2 molecules and a conducting channel is created. In the *hot ionization* regime, the ionized channel is called a *leader*. The average speed propagation of streamers in air is around 10^5 m/s while leaders propagate at approximately 10^4 m/s in a natural discharge according to Pépin *et al.* (2001).

Finally, the streamers at the tip of the leader connect to the ground in the so-called *final jump*, initiating a positive leader at the ground that connects to the negative leader and initiate the *electric breakdown*, also called return stroke or lightning strike.

In the atmosphere, convective currents, with speeds up to 20 m/s (Gary, 2004) form thunderstorm clouds. The lower part of the cloud is formed with water drops whereas the top of it is made with ice crystals. Thermodynamical changes and shocks between particles (water drops and ice crystals) due to the winds within the cloud will charge those particles. Positively charged particles will migrate to the top of the cloud while the negatively charged ones will drift to the bottom. The precise mechanism involved to charge the different particles and separate them is still unclear (Pruppacher & Klett, 1978, Gary, 2004). The shape of the charged particles will enhance the electric field around them. The resulting static electric fields reach 10–15 kV/m at ground level and up to 50 kV/m some hundreds of meters above ground. These high fields initiate corona discharges, that under sufficient electric field and charge supply develop into streamers, and then ionized plasma channels, or leaders. The strong electric field in front of the leader ionizes the gas and creates new corona and streamers, which then allow the leader to "jump" forward. This is the reason of the erratic formation of an electric breakdown. In the end, the

chapter. An erratum of the article has been submitted for publication.

leader will attach to a streamer or leader coming from the ground and give rise to the lightning strike itself (Gary, 2004).

6.2 Remote Electrical Arc Suppression by Laser Filaments

In this section, it is demonstrated that laser filaments can suppress electrical breakdown between DC high-voltage electrodes, even when the filaments are far from the electrodes.

6.2.1 Experimental Setup

The experimental setup (Figure 6.1) relied on a DC high-voltage generator (100 kV, 200 µA maximum current) connected to spherical electrodes (1.2 cm diameter) that could be moved along and away from the filament. One electrode was grounded, while the other one was set to the potential of the high-voltage generator.

A Ti:Sapphire chirped pulse amplification system delivered 80 fs pulses of 14.5 mJ centered at 800 nm at 1 kHz repetition rate. This beam of initial 4 cm diameter was slightly focused ($f = 2$ m), generating 3 to 4 self-guided filaments. Due to the external focusing of the beam, the filament length was about 20 cm in this configuration.

The experiments have been performed at room temperature ($T = 20$ °C), at a relative humidity around 30 %. Correspondingly, the background resistivity of the air is about $3 \cdot 10^{14}\,\Omega\,\mathrm{m}$ according to Pawar *et al.* (2009).

6.2.2 Electrical Arc Suppression

Figure 6.2 clearly illustrates the electrical arc suppression by laser filaments. Applying 100 kV in a 12 cm gap between the electrodes, a value close to the threshold for natural breakdown, results in typically one electrical arc per second (Figure 6.2a). Switching on the laser in the vicinity of the electrodes fully suppresses the sparking within less than one second (Figure 6.2b). Instead, a glow discharge connects the electrodes to the filament, even if it is several centimeters away from them. Furthermore, the blueish glow of the filament, that is typical of the laser-generated plasma as discussed by Couairon & Mysyrowicz (2007) and Bergé *et al.* (2007), is much brighter in presence of the high-voltage than without it, evidencing increased avalanche ionization in the filament under the electric field.

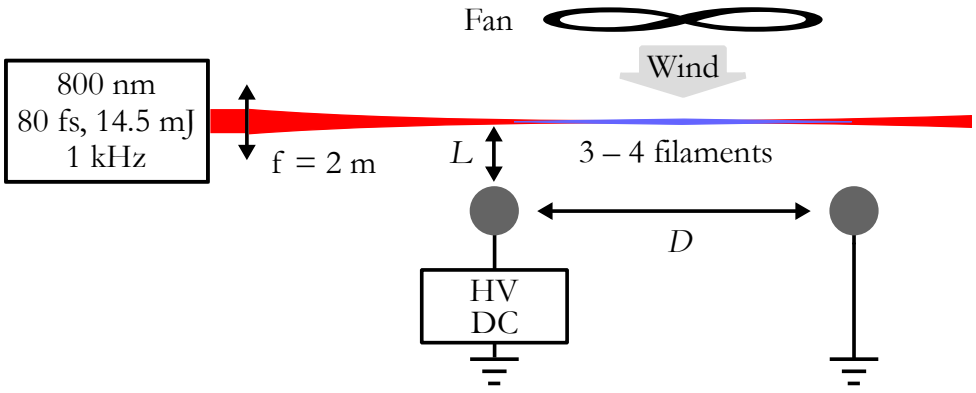

Figure 6.1: Experimental setup. 100 kV are applied on the HV electrode. The distances D and L can be varied and wind can optionally be blown by the fan at ~2 m/s in the filament–electrode plane.

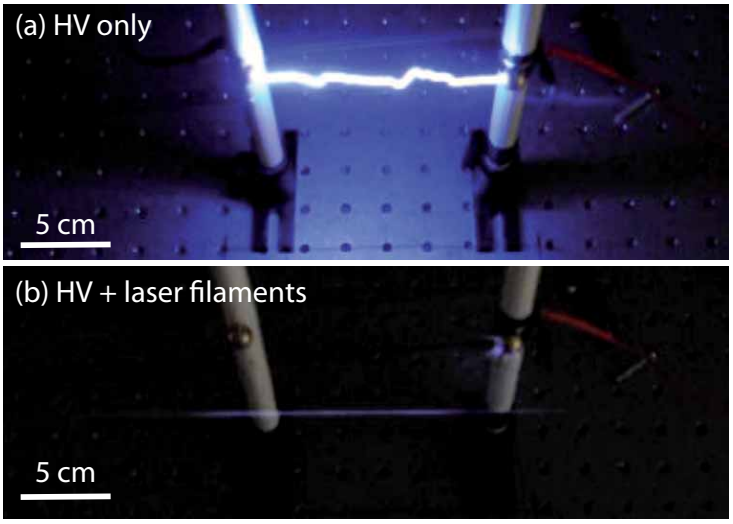

Figure 6.2: Electrical arc suppression by laser-induced neutralization under 100 kV. Electrical arc without laser (a) and arc inhibition when the laser is turned on (b).

6.2.3 Influence of Wind on Discharge Triggering

To better understand the mechanism behind this laser-induced electrical arc suppression, a fan was used to blow air perpendicular to the filament–electrode plane at approximately 2 m/s (see Figure 6.1). The wind from the fan was therefore fast enough to completely renew the air in the filament region between two pulses at 1 kHz. The 100 kV DC voltage was applied to the charged electrode roughly 5 cm away from the grounded electrode.

Figure 6.3a displays natural breakdown with neither laser filament nor wind involved. Electrical arcs form almost continuously between the two electrodes in this situation. The discharges attach to the electrodes at their nearest points. When the laser is propagated along the electrodes from right to left, the discharges stop, as displayed in Figure 6.3b. As discussed above, some corona, especially visible on the left electrode, links the electrodes to the laser filament which glows more than without the electric field. At such short distance between the electrodes, the laser

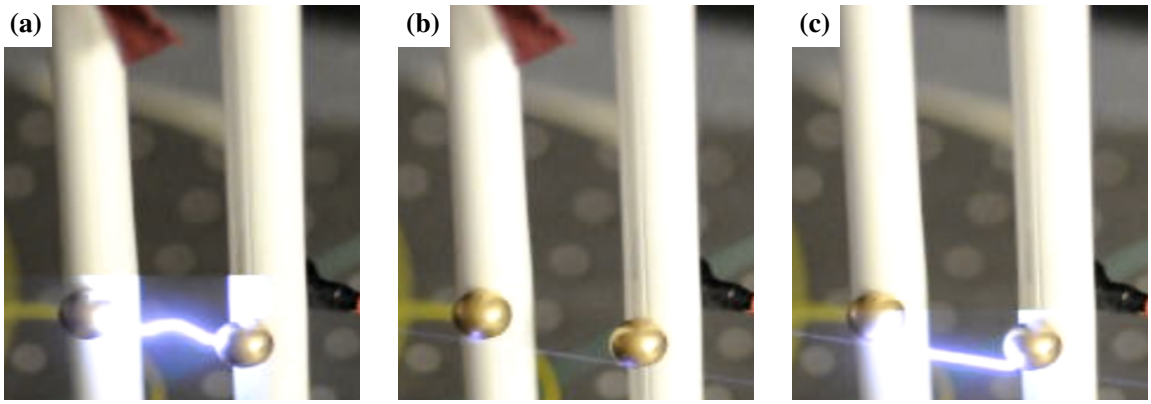

Figure 6.3: Influence of 1 kHz laser filament and wind on electrical breakdown. Natural 100 kV breakdown with neither laser filament nor wind (a). Electrical arc suppression when the 1 kHz moderate-power laser filament is propagated along the electrodes (b). Guided discharges along the laser filament when the fan is turned on (see the cloth at the top is blown away) (c).

filament needs around one second to fully neutralize the electric breakdown. After this time, no further breakdown is observed as long as the air stays still. Finally on Figure 6.3c, the fan is turned on (see the cloth at the top of the right electrode post) and electrical arcs form again. In this case, the discharges are guided along the laser filament instead of following the erratic path of a natural discharge.

Turning the fan on without the laser filament "blows" the natural discharges away, bending them by a few centimeters downwind. This shows that they occur where the ion density is high. As the bent discharge path is longer than that when no wind is applied, the discharges are somewhat less frequent in this configuration.

6.2.4 Discussion

In this section, an 800 nm, 14.5 mJ filament at 1 kHz efficiently suppressed electrical arcs between a charged electrode at 100 kV DC and the earth. The electrical arc was reestablished by blowing wind perpendicular to the electrodes, in the electrode–filament plane.

When no wind is blown, the high voltage applied on the electrode is strong enough to accelerate the charges created by the laser filament such as to create avalanche ionization and heating of the plasma channel, as discussed by Vidal *et al.* (2000). At 1 kHz repetition rate, the heat generated by the successive laser pulses accumulate, increasing the conductivity of the channel. The plasma channel is therefore similar to a leader and the charges flowing through it are sufficient to compete with the leader forming on the natural breakdown path between the electrodes.

The current density through each of those two competing channels leads to a voltage drop in the high-voltage supply. This inhibits the electrical breakdown as long as the filament is not too far from the electrodes, in this experiment less than 10 cm between the electrodes and the laser filament when the electrodes are 16 cm apart. Indeed, the conductivity between the filament and the electrodes is due to the ion density in this volume, which depends on the sub-microsecond recombination time of the ions created by the laser filaments. Inside the plasma channel, the charge density is high and the induced resistivity is around 0.1 Ω m a few hundreds of nanoseconds after the laser pulse propagation according to Ladouceur *et al.* (2001), much lower than the 10^{14} Ω m resistivity of air. The limiting factor for conducting current through the filament region is therefore the distance between the ionized filament region and the electrodes.

Blowing the wind perpendicular to the filament propagation direction fully renews the air in the filament volume between two laser pulses. Therefore, no cumulative heating of the air by multiple laser pulses can be obtained and the avalanche ionization through the cold channel is too weak to create a voltage drop in the power supply. Therefore, when the laser filament is close to the electrodes, an electric arc can be triggered and guided through the laser filament as shown by Vidal *et al.* (2000).

The next section will discuss in detail the impact of the laser filament when the plasma channel stays colder than the leader temperature.

6.3 Charge Neutralization by Laser Filaments

After discussing the interactions of laser filaments with high electric fields, experiments have been conducted without electrical breakdown to investigate the charge neutralization abilities of laser filaments at low electric fields.

This experiment consisted in evaluating the impact of the laser beam position, repetition rate and average power on the laser filament ability to unload a charged capacitor. The impact of the voltage sign and of wind on the charge neutralization will also be discussed.

6.3.1 Experimental Setup

The experimental setup used in this section is displayed in Figure 6.4. A Ti:Sapphire laser, already described in Section 6.2, delivered 80 fs pulses of 14.5 mJ at 1 kHz and centered at 800 nm. The beam of initial 4 cm diameter was focused with a $f = 2$ m lens and it created three to four filaments approximately 20 cm long.

The electrical setup relied on a DC high-voltage generator of 14 kV connected to a 10 nF capacitor to store charges. One electrode was attached to the capacitor while the other one was grounded, unless otherwise specified. The two electrodes could be moved along (D) and around (L) the laser filament from 2 mm, the minimum distance to avoid matter ablation on the electrodes, to 30 cm away.

After loading the capacitor, the generator was disconnected from the capacitor and the electrode to investigate the flow of a fixed charge Q between the electrodes and the associated unloading of the capacitor. The current flowing through the ground electrode was measured by monitoring the voltage on a 16.2 Ω resistor connecting the latter to the earthing. The signal was recorded on a 100 MHz bandwidth oscilloscope, synchronized with the laser pulses by a photodiode detecting the scattering of the beam on the beam dump, 2.2 m downstream of the interaction region. The discharge of the capacitor attached to the high-voltage electrode was investigated using a FLUKE 80K-40 high-voltage probe.

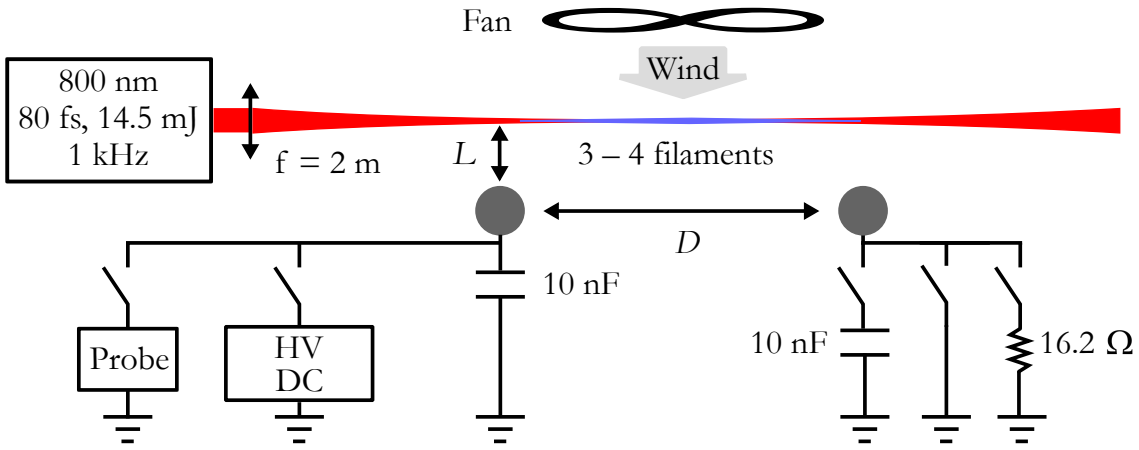

Figure 6.4: Experimental setup. The electrode with a capacitor is charged to 14 kV and the generator is then disconnected. After the laser has been shined, the residual voltage on the electrode is measured via a HV-probe. The distance D between the electrodes and the distance L from the electrodes to the filament can be varied. Unless otherwise specified, $D = 16$ cm and $L = 2$ mm.

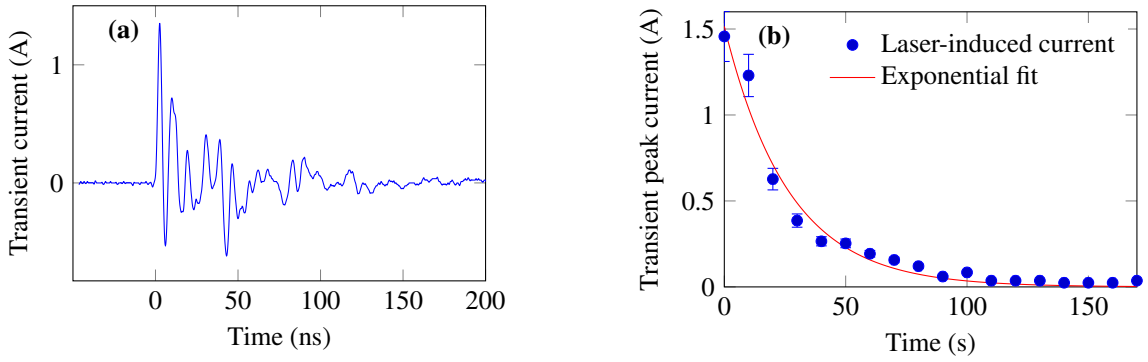

Figure 6.5: Laser unloading of a 10 nF capacitor initially loaded under +14 kV. The electrodes were placed at a distance $D = 16$ cm apart, at a lateral distance L of 2 mm from the laser beam. Laser-induced electronic polarization measured on a resistance $R = 16.2\,\Omega$ between the electrode and the ground (a); time zero corresponds to the laser pulse. Decay of the magnitude of the peak current, corresponding to the capacitor discharge (b).

Parameter changes such as the laser used, the electrode geometrical configuration or the addition of wind will be discussed for each relevant experiment below to improve readability.

The experiments have been performed in the same environmental conditions as in Section 6.2.

6.3.2 Spark-Free Neutralization

Without the laser, no measurable current flows between the electrodes, so that the capacitor keeps its load without measurable leak for over 20 hours. In contrast, each laser pulse results in a current burst on the resistance to the ground, proportional to the charge on the capacitor (Figure 6.5a). The time delay between the laser pulse and the initiation of the corresponding signal is shorter than the 5 ns time resolution of the detection system. It is therefore faster than the time required to establish a negative corona discharge, that lies in the 100 ns range according to Sugiyama *et al.* (2009).

The capacitor is progressively unloaded by the laser filament (Figure 6.5b), with a decay time $\tau = 25$ s, corresponding to 25 000 laser pulses.

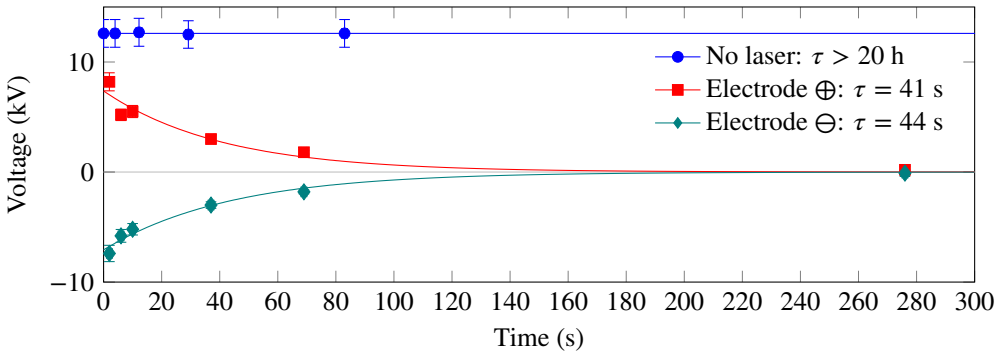

Figure 6.6: Simultaneous discharge of capacitors loaded under ±14 kV, with a 16 cm gap between the electrodes, placed at $L = 2$ mm from the laser. The lines display exponential fits, τ being the decay time.

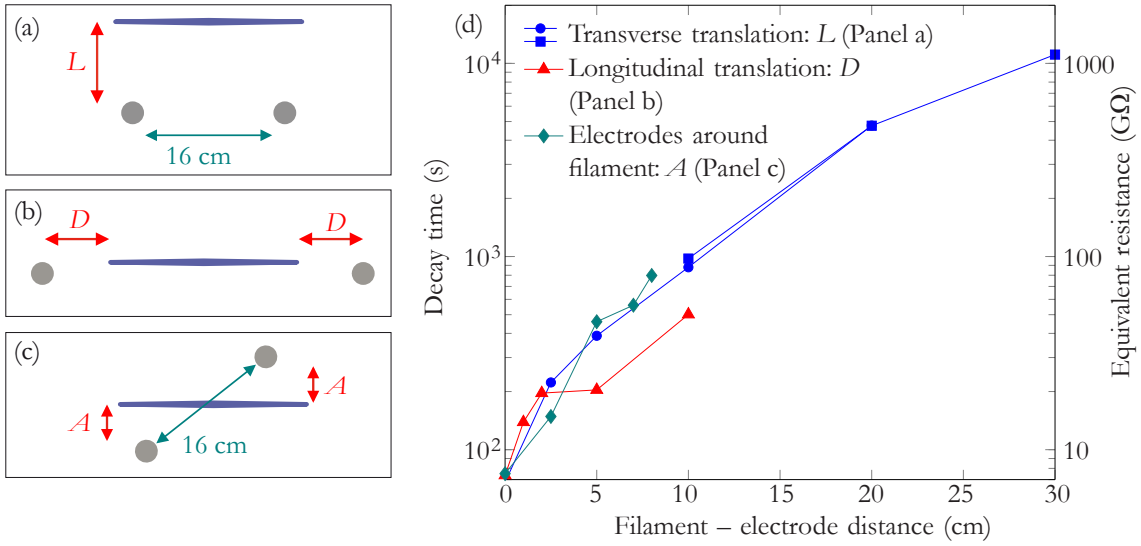

Figure 6.7: Effect of geometry on laser-induced neutralization. Geometrical configurations: transverse (a) and longitudinal (b) distances and filament crossing the electrode gap (c). The gray circles represent the electrodes and the blue line is the filament. Decay time of the charge as a function of the distance between the electrodes and the filaments (d).

The flow of charges from one electrode to the other is characterized by inserting an initially empty 10 nF capacitor between the ground electrode and the earth (see Figure 6.4). Under the laser influence, the high-voltage capacitor progressively discharges. This is the first time the loading of a capacitor by a laser filament without electrical breakdown is demonstrated. About one third of its charge reaches the empty capacitor. As a result, the charge of the latter reaches a maximum after 81 s, before decaying again. In contrast, when both 10 nF capacitors are simultaneously preloaded under +14 and −14 kV, respectively in a floating configuration, they unload symmetrically (Figure 6.6), independently from the electrode polarity.

6.3.3 Geometrical Considerations

The laser filaments can even neutralize the high-voltage remotely as shown in Figure 6.7. In a first geometrical configuration, the laser beam was moved away laterally from the electrodes and parallel to the gap (Figure 6.7a). In a second one, the electrodes were taken apart from one another, beyond the filament ends: the filament–electrode distance therefore increased longitudinally (Figure 6.7b). Finally, the electrodes were rotated around the filament while keeping a 16 cm distance between them (Figure 6.7c).

In these three configurations, the decay times are similar for identical distances between the electrodes and the filament (Figure 6.7d). Therefore, the distance between the filament and the electrodes governs the laser-induced neutralization, rather than the geometrical configuration. In particular, setting the filament parallel or perpendicular to the electrode gap results in similar laser-induced neutralization times.

The decay time of the initial charge of the capacitor $Q_0 = C \cdot V = 1.4 \cdot 10^{-4}$ C increases with the filament–electrode distance from 68 s at 0.2 cm to 3.1 h at 30 cm. This increase is linear up to a typical filament–electrode distance of 10 cm. Beyond this distance, the decay time tends to grow faster with the increasing filament–electrode distances, while the decay of the charges

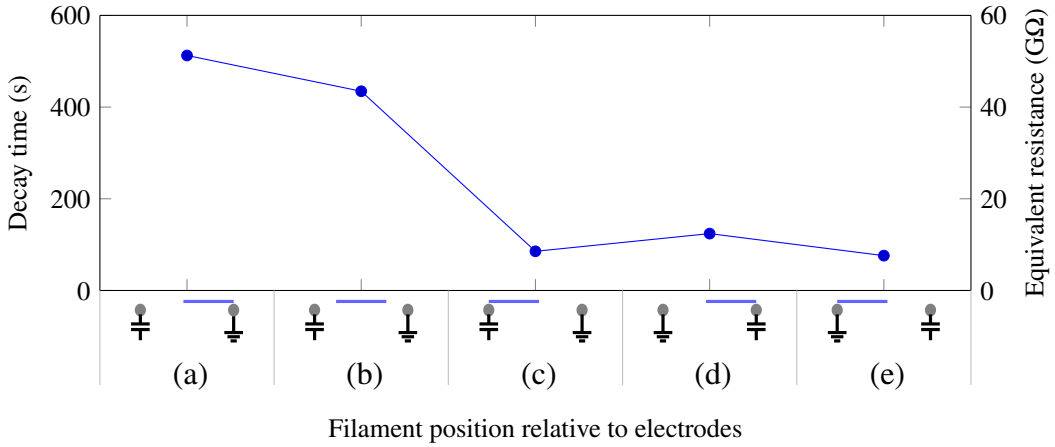

Figure 6.8: Charge decay time as a function of the relative position of the filament and the electrodes, located 2 mm away from the laser beam. On the symbols of the x-axis, the laser filament (straight blue line) propagates from left to right. Labels are for reference in the text. The capacitor is charged at +14 kV and the gap between the electrodes is 40 cm wide.

progressively deviates from the exponential trend, suggesting the occurrence of a new regime at long distances. However, even for a filament–electrode distance of 30 cm equal to twice the gap between the electrodes, the laser accelerates the unloading of the setup by one order of magnitude, illustrating the long-range effect of the laser filaments.

The exponential decay of the capacitor charge, together with its linear dependence with distance at least over the first 10 cm, are consistent with the simple picture of the discharge of an RC circuit. Within this rough, quasi-stationary description, the observed decay times correspond to effective resistances of 6.8 GΩ to 1 TΩ for distances from 0.2 to 30 cm, since $C = 10$ nF, as displayed on the right vertical axis of Figure 6.7. Note that, to keep reasonable experimental times, the measurement at 30 cm has been performed with a capacitor reduced to 200 pF and then renormalized to $C = 10$ nF. This procedure yields consistent results with the 10 nF capacitor for 10 and 20 cm distances (blue squares in Figure 6.7d).

For a given filament–electrode distance, the charge decays slightly faster when the beam passes close to the electrodes and the filament bridges part of the electrode gap (Figure 6.7b), as compared to the other configurations. This may be due to the longitudinal plasma density along the filament, that rises faster at the beginning of the filament than it falls down at its end according to Couairon & Mysyrowicz (2007) and Bergé *et al.* (2007). As a consequence, the end of the ionized region is not precisely defined and the distance to the electrodes may be overestimated.

This asymmetric behavior was further investigated by displacing the two electrodes 40 cm apart along the filament, changing therefore the distance between the charged electrode and the filament (see symbols on the x-axis of Figure 6.8). As a result of this longitudinal plasma density profile asymmetry in the filament, the charge decays 6.5 times faster when the high-voltage electrode is located 20 cm before the filament than at the same distance beyond it (Figure 6.8 labels (a) and (e) respectively). This illustrates the key role played by the high density of free charges released in the laser filament. In contrast, the neutralization is insensitive to the position of the grounded electrode, as well as to the longitudinal position of the electrodes within the filament.

Finally, it should be noticed that the unloading of a negative electrode facing a ground electrode

behaves similarly to a positive electrode facing a ground electrode.

6.3.4 Influence of the Average Power and Repetition Rate

To investigate the impact of the laser average power and repetition rate, two different setups were used here. The repetition rate of the laser setup used up to now and hereafter referred to as the moderate-power beam was varied from 10 to 1000 Hz. A second laser system of high average power, hereafter referred to as the high-power beam, was compared to it.

This high-power beam laser system was already described in Chapter 2. The central wavelength of the laser was 1030 nm and it delivered 100 mJ with 1.3 ps pulse duration. The repetition rate in this case was varied from 100 to 1000 Hz and it created three to four approximately 50 cm long filaments when focused with a 2 m focal length curved mirror.

The electrical setup used with the high-power beam is described in detail in Figure 1, variant 1 of Appendix B and the concept is the same as in Figure 6.4. A 1 nF capacitor and a 1:4000 voltage divider of 300 GΩ impedance and a follower amplifier (TL1169) were used in this case. The voltage on the capacitor was probed periodically by an ARDUINO-based device. The voltage applied in this case was 10 kV.

The spark-free neutralization of a charged capacitor investigated up to now at 1 kHz also occurs at repetition rates down to 10 Hz. As shown in (Figure 6.9a), the moderate-power beam is less efficient to neutralize the charges than the high-power beam. This is not surprising as the high-power beam is more energetic and the pulses last longer, which gives more time to charges to accumulate in the filament volume. As it can be expected, the high-voltage decay is faster at higher repetition rates.

However, an interesting feature emerges when the unloading time is converted to the capacitor unloading efficiency of one single pulse (Figure 6.9b). As the unloading capacity of a single pulse decreases with the repetition rate, pulses are not fully independent one from another.

A wavelength study in the near to mid-infrared has also shown interesting results. The full study of which I am a coauthor was published by Mongin *et al.* (2016b) and can be found in Appendix B. It demonstrates that although the charge density in the mid-infrared is lower than in the near-infrared, the total charges created during laser filamentation are similar. Indeed, mid-infrared laser filaments are three to six times larger in the mid-infrared than in the near-infrared

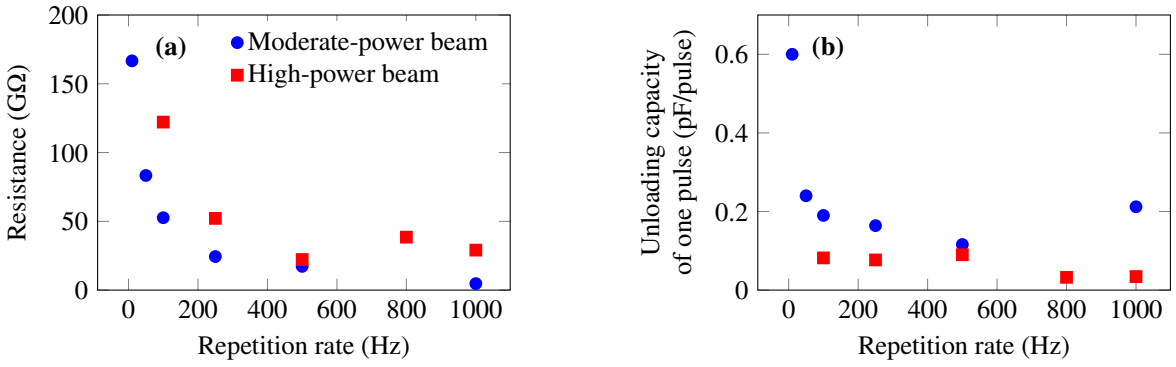

Figure 6.9: HV decay time (a) and unloading capacity of a single pulse (b) with respect to the repetition rate. $D = 16$ cm between the electrodes and $L = 0.5$ cm between the laser filament and the electrodes (see Figure 6.4).

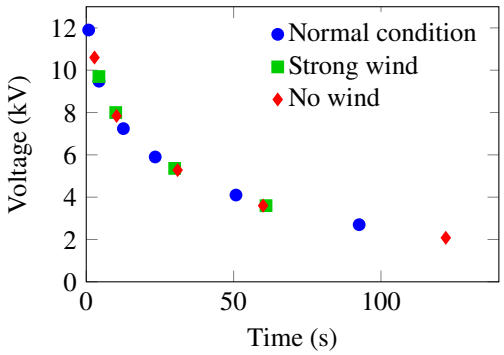

Figure 6.10: Induced capacitor unloading under different ventilation conditions with the electrodes $L = 2$ mm away from the filament and $D = 16$ cm apart.

and the ionized volume is therefore much larger. As the energy deposited is also lower in the mid-infrared, mid-infrared laser filaments are less able to trigger and guide high-voltage electric breakdown than their near-infrared counterparts.

6.3.5 Influence of Wind

As in Section 6.2.3, the influence of wind on the charge neutralization is investigated here by blowing wind with a fan perpendicular to the filament–electrode plane at approximately 2 m/s (see Figure 6.4). The wind from the fan was therefore fast enough to completely renew the air in the filament region between two pulses at 1 kHz.

As shown in Figure 6.10, the decay time of the charges from the capacitor is totally insensitive to changes in ventilation. The blue dots are the nominal experimental conditions, where the air conditioning blows from the ceiling, above the laser filament and electrodes. The laser filament was propagated $L = 2$ mm away from the electrodes, separated by $D = 16$ cm. In the condition with no wind, the air conditioning was turned off and air movements in the room were reduced to a minimum. In the strong wind condition, the air conditioning and the fan were turned on.

6.3.6 Discussion

In this section, it was shown that laser filaments in low electric fields can unload an initially charged capacitor, even when the laser filament propagates far from the capacitor. It was also proven that a capacitor could be loaded by a laser filament without creating an electrical arc between the electrodes. In contrast with the experiments described in Section 6.2, the electric field in this experiment is low and is not able to strongly heat the filament volume. Therefore, instead of creating a leader able to circulate a strong current, the heat is not able to accumulate and the filament acts more like a streamer of cold plasma in this case. This explains why the wind does not have any effect on the capacitor unloading time.

The free electron lifetime in the filament volume is shorter than 100 ns and most electrons will have recombined before arriving at the electrode as they travel at an average speed of $1.5 \cdot 10^4$ m/s in an electric field of 100 kV/m. Also, attachment of electrons to neutral molecules creates many negative ions (Figure 6.11). The decay time of the filament-induced ions is therefore mainly governed by ion-ion recombination, which is a second-order kinetics ($dN_{\text{ions}}/dt = -\beta_{np} N_{\text{ions}}^2$, see Equation (5.10) and (5.11)). This recombination rate is very large when the initial concentration of charges is high. After 10^{-7}–10^{-6} s, the positive and negative ion concentrations decay very slowly, almost forming a plateau at around $5 \cdot 10^{19}$ m^{-3} during a few milliseconds. This means that this high ion density lasts longer than the time between two pulses at 1 kHz. The successive

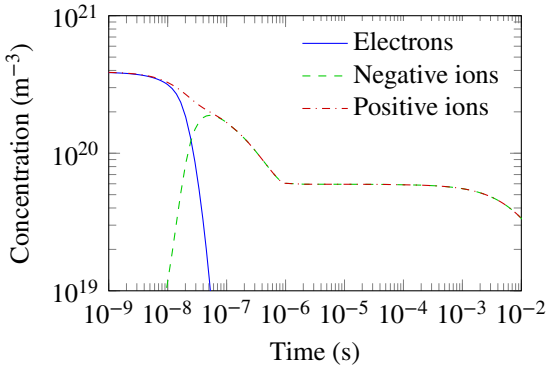

Figure 6.11: Charged particle concentrations after propagation of the laser filament.

plasma volumes created by the laser filaments drift towards the electrodes and create a continuous region of high ion density between each of the electrodes and the laser filament.

The current between the electrodes needs a relatively high charge density along the path between the electrodes and the filament to flow. The local resistivity is proportional to $1/N$, where N is the charge density. At high repetition rates, the charge density does not decay back to the background level between two laser pulses and the current becomes relatively independent of the repetition rate. It is therefore possible that above a certain charge density along the path, adding more charges by increasing the laser repetition rate does not improve the unloading capacity of each individual pulse.

However, the charge density created by the laser filament reduces while the charges travel from the filament to the electrodes. This is probably why the time needed by the laser filament to neutralize the charges on the capacitor increase more than linearly when the beam is far from the electrodes.

6.4 Conclusion

In this chapter, two distinct but related properties of laser filaments were studied. At first and in opposition with what has been observed until now, it has been shown that under certain conditions, electrical breakdown can be suppressed by laser filaments rather than triggered as it is usually reported. The breakdown suppression can even be observed when the laser filament is centimeters away from the charged electrodes. This phenomenon depends on the electric field ability to create a leader of hot plasma within the laser filament volume.

In the second part, the neutralization by the laser filament of charges stored in a capacitor was investigated at lower electric fields. In the cases investigated here, the neutralization time depends linearly on the distance between the electrodes and the filament as long as this distance smaller than half the distance between the two electrodes. When the distance between the laser filament and the electrodes is increased further, the neutralization time increases rapidly with the distance between the laser filament and the electrodes. The geometrical arrangement of the electrodes around the filament does not affect the neutralization time, neither does the sign and polarity of the electrodes.

Surprisingly, increasing the laser repetition rate does not reduce the neutralization time linearly. Indeed, the unloading capability of each single pulse is reduced when the laser repetition rate is increased. This could be linked to the spatial distribution of charges between the laser filament and the electrodes. As the electric field is low, the plasma created within the laser filament

channel remains cold and the wind speed, although being fast enough to prevent cumulative heating in the leader channel in Section 6.2 does not impact the capacitor unloading.

In the introduction of this chapter, it was mentioned that lasers in the ultraviolet range are very promising for discharge triggering and guiding. The next chapter will therefore focus on the triggering and guiding efficiencies of electrical discharges by ultraviolet laser pulses. Méjean *et al.* (2006) demonstrated that near-infrared laser pulses discharge triggering efficiencies could be improved by firing a nanosecond pulse of 532 nm with the ultrashort laser pulse and such scheme will be investigated in the case of ultraviolet ultrashort laser pulses.

Discharge Triggering with Ultraviolet Laser Filaments 7

In the previous chapter, the electric properties of near to mid-infrared laser sources have been investigated. In this chapter, laser triggered discharges at larger scales by laser filaments in the ultraviolet range (UV) will be discussed.

As already discussed in Chapter 1, ultraviolet laser filaments have a number of advantages over infrared radiation. Schwarz *et al.* (2000) and Tzortzakis *et al.* (2000a) demonstrated that ultraviolet filaments can be very stable on meter-long distances and that they are less prone to pulse splitting than infrared pulses. Multiphoton ionization is much more efficient in ultraviolet filaments than in the near-infrared as it only needs three photons at 266 nm instead of 8 – 11 at 800 to 1030 nm.

In the ultraviolet, Diels & Zhao filed a patent already in 1992 claiming that ultrashort laser pulses in the ultraviolet could trigger and guide lightning and that this effect could be improved by sending either longer pulses in the visible range or a train of longer ultraviolet pulses after the main ultrashort ultraviolet pulse. Zhao *et al.* (1995) and Miki & Wada (1996) proved already two decades ago that discharges could be guided in pure nitrogen and air by ultraviolet laser filaments. Rambo *et al.* (2001) then discussed the possibility to guide laser-triggered discharges in the ultraviolet over 10 m and concluded that one should add at least 5 J at 750 nm in about 10 µs to maintain the plasma density created by a 100 mJ, 800 fs 248.6 nm laser pulsed at 10 Hz. On the other hand, Zvorykin *et al.* (2015b) recently published results in which they showed discharge triggering and guiding with amplitude-modulated ultraviolet laser pulses of 100 ns at 248 nm.

Ten years ago, Méjean *et al.* (2006) have demonstrated experimentally that adding nanosecond pulses to an ultrashort laser beam improved the triggering of high-voltage (HV) electrical discharges with a near-infrared laser beam.

In the present work, a 266 nm, 200 ps pulsed laser beam is used to trigger discharges over 37 cm between two charged electrodes. The impact on the triggered electrical discharge of adding nanosecond pulses at 532 nm and 1030 nm to the ultraviolet laser beam is investigated. My contribution to the present work has been to contribute preparing the equipment and experimental setup and to record and treat the data, in a collaboration with the group of Professor J.-C. Diels in New Mexico (USA).

7.1 Material and methods

A laser system home-made by the group of Professor J.-C. Diels and described by Feng (2016) was used as the ultraviolet laser source for this experiment. The central wavelength of the laser was 266 nm and it worked at 0.8 Hz repetition rate. It delivered 200 ps long pulses and 270 mJ output energy. Two additional THALES SAGA 220 Nd:YAG lasers with a 10 ns pulse width were

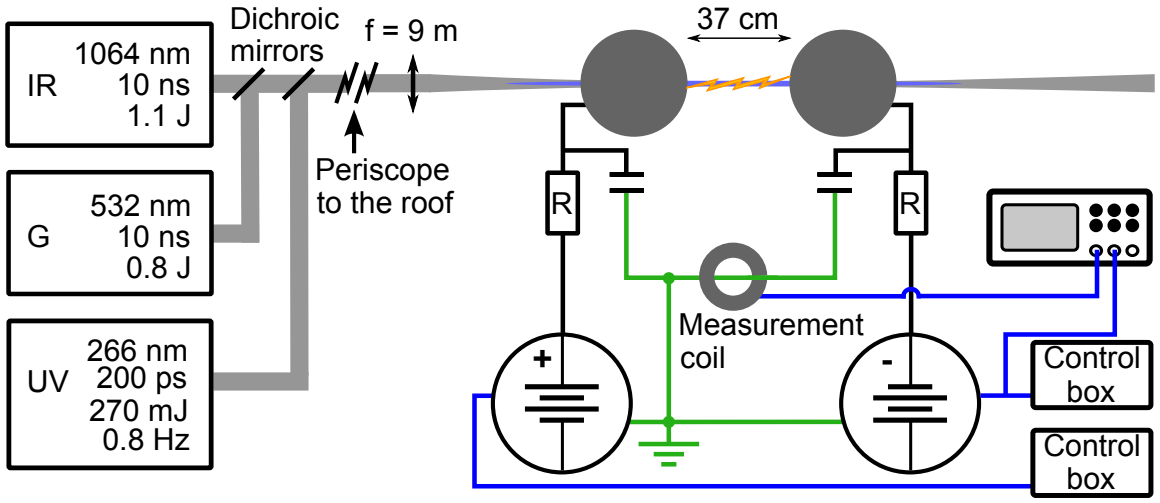

Figure 7.1: Experimental setup. The green (G) and infrared (IR) lasers are resized by a telescope (not shown) to match the ultraviolet (UV) beam diameter before being coupled with dichroic mirrors. In blue, the BNC connections to monitor the voltage delivered by the high voltage generators and the BNC to measure the current through the ground cable (in green).

used to investigate the impact of the heating and the photodetachment rate of O_2^- in the plasma channel created by the ultraviolet laser on the triggering of high-voltage discharges. One of the secondary lasers delivered 1.1 J at the fundamental wavelength of 1064 nm (IR) and the other was frequency-doubled at 532 nm (green) and delivered 650 mJ. The three beam diameters were matched with telescopes and combined in the laboratory, making sure the three beams were collinear (Figure 7.1). The three beams were then sent on the roof of the building through a periscope over about 30 m. Once on the roof, the beams were slightly focused by a 9 m focal length fused silica lens between the two high voltage (HV) 40 cm diameter spherical electrodes spaced 37 cm from one another in the middle of a Faraday cage. Each electrode is charged with the same DC voltage but with opposite polarities. Each capacitor bank consists of ten capacitors with an equivalent capacitance of 0.2 nF and a resistance of $R = 100\,\mathrm{M\Omega}$ chosen such as to minimize the inductance. In these experiments, the voltage has been varied from ± 125 to ± 170 kV, leading to an average applied electric field from 675 to 920 kV/m between the electrodes.

The high-voltage control boxes as well as the oscilloscope used to collect data were set outside of the Faraday cage and shielded from electromagnetic radiations in a grounded metal box. Cables were protected with metal mesh from the Faraday cage to the metal box. The temperature and humidity in the cage were monitored during the day and some ventilation with cool air was supplied to avoid overheat in the cage. A photodiode behind the last mirror triggered the oscilloscope. The effective ultraviolet energy available between the electrodes was approximately 70 % of the output pulse energy, i.e. $\sim$190 mJ. The current flow to the ground when a discharge occurred was recorded by induction through a magnetic coil around the ground cable and 150 to 250 laser shots were recorded for each data set, one to four data sets being recorded for each laser and voltage configuration. Finally, a camera was placed in the cage as far as possible from the electrodes to take pictures of the discharges. One out of three laser shot was recorded by this mean for electric fields under 850 kV, the camera trigger refusing to respond at higher electric fields.

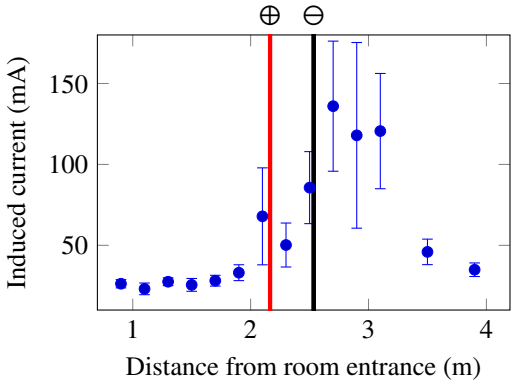

Figure 7.2: Induced current by the laser filament between two square 4 cm^2 plates as a probe with a 500 kV/m electric field between them (fast polarization signal). The red and black lines depict the respective positions of the positive and negative electrodes used in the high-voltage experiment.

To characterize the ultraviolet laser filaments, their conductivity was measured along the beam propagation axis with a capacitive probe. Two square plates of 4 cm^2 spaced with 2 cm were placed on either side of the filament and moved along the beam propagation axis as in Chapter 4. One plate was charged with 10 kV and the other one was connected to the ground, yielding an electric field of 500 kV/m. The current flow due to the laser filament was probed through a 10 Ω resistance on the cable to the ground.

The electrodes were positioned along the beam propagation axis by eye and by determining by ear where the filament was the loudest such as to insure that the filament would cross both electrodes. Figure 7.2 shows the induced current representative of the plasma density at different positions along the filament.

7.2 Faster Discharge Triggering with Nanosecond Lasers

At the electric fields used during this experiment, no discharge occurs without the laser. All the observed discharges are therefore laser-triggered. Figure 7.3 illustrates a fully-guided (a) and partly guided discharge (b) for the highest applied electric field (920 kV). Some discharges, although triggered by the laser, are not guided at all along the filament plasma channel. The guided length of the discharges on the recorded pictures was calculated as the number of white pixels along the beam propagation axis between the two electrodes.

Figure 7.4 shows the discharge probability for the ultraviolet filament alone and the subsequent

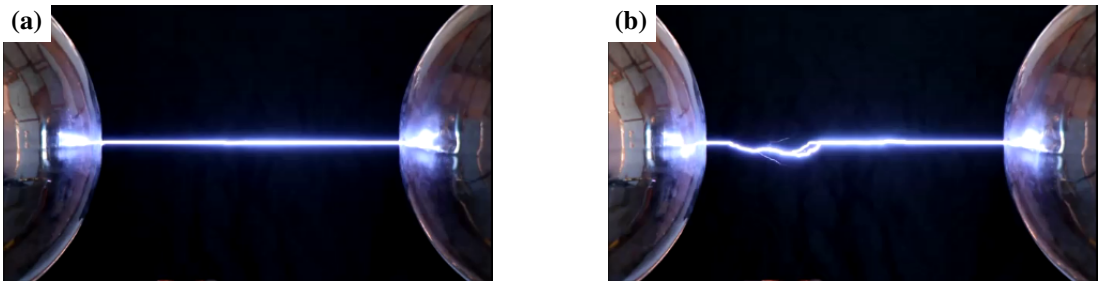

Figure 7.3: Laser triggered fully guided (a) and partly guided (b) electrical discharges. The gap is 37 cm wide and +170 kV and −170 kV are applied on each electrode, resulting in an electric field of approximately 920 kV/m. This picture is taken from the outside of the cage by the slightly opened door to allow light in the room.

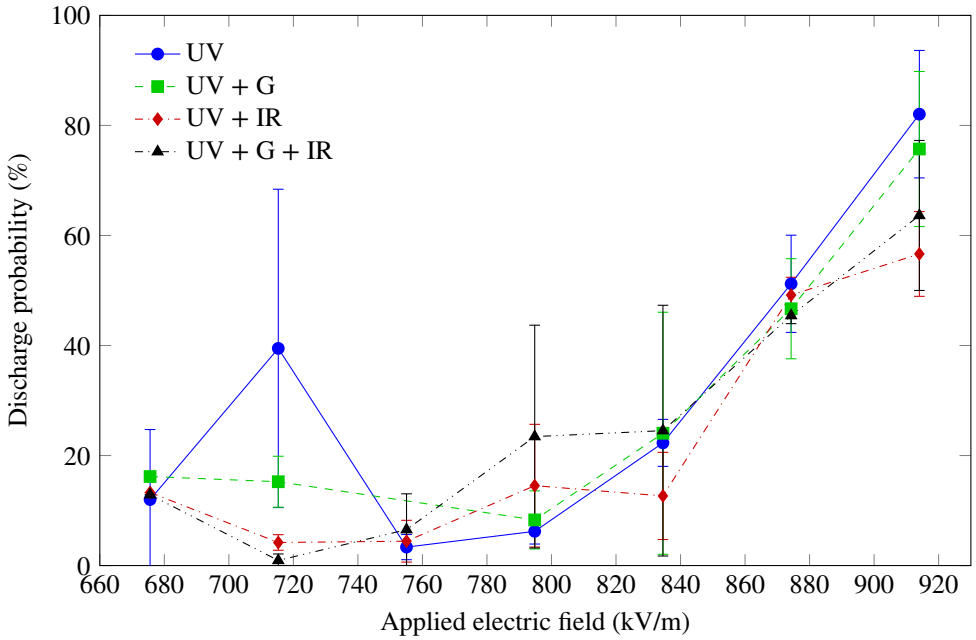

Figure 7.4: Discharge probability with respect to the applied electric field for all delays ≤50 ns between the ultraviolet (UV) and green (G) and/or infrared (IR) laser pulses. The error bars are the standard deviation over the different data sets.

addition of either the near-infrared beam, the green beam or both at the same time. The discharge probability at the highest electric field is of 80 % for the ultraviolet laser filament alone and the 50 % discharge probability is reached at around 875 kV/m. This is more than twice lower than the natural electrical breakdown voltage, according to Feng (2016) and taking into account the geometrical configuration of the electric field.

The error bars have been calculated as the standard deviation of the probabilities on each individual data set of 150 to 250 data points each for all data recorded with delays ≤50 ns between the nanosecond and the ultraviolet lasers. The large error bars at low electric fields on Figure 7.4 are due to some voltage generator instability. Monitoring the voltage of one electrode on the oscilloscope has shown that it sometimes randomly jumps to another value between two laser shots.

Méjean *et al.* (2006) demonstrated that a 532 nm nanosecond pulse could improve the 800 nm discharge triggering efficiency in an electric field of 750 kV/m. In the present experiment, Figure 7.4 shows that adding a 532 nm or 1064 nm nanosecond pulse to the 266 nm filament in an electric field from 670 to 920 kV/m has no significant impact on the discharge triggering probability , whatever delay is applied between the different laser beams. Indeed, the discharge triggering efficiency of the ultraviolet laser filament alone is as good as that obtained by Méjean *et al.* (2006) when they added the nanosecond laser to their 800 nm laser filament. In other words, the ultraviolet laser is actually more efficient than the near-infrared laser to trigger discharges and this is why no difference is noted on the discharge probability when the nanosecond pulses are added to the ultraviolet beam.

Although adding one or two ∼1 J pulses to the ultraviolet filament does not increase the discharge probability, it does impact the breakdown process as shown on Figure 7.5. The delay between the ultraviolet pulse alone and the electric breakdown with respect to the applied electric

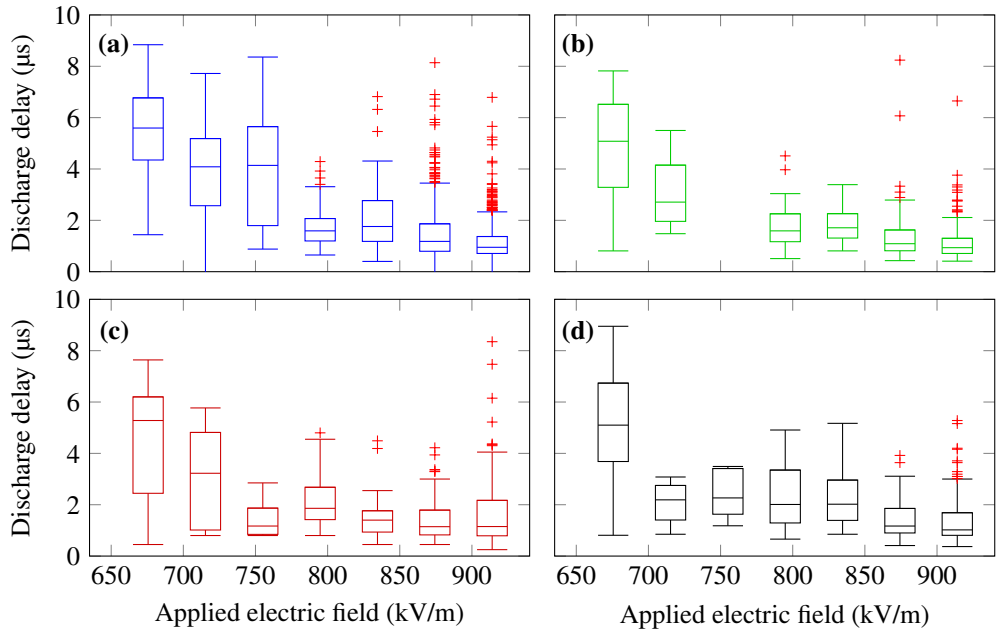

Figure 7.5: Time delay between the laser shot and the triggered discharge with respect to the applied electric field for the UV only (a) and the added 532 nm (b), 1064 nm (c) and both nanosecond lasers. 150 to 250 laser shots were recorded for each data set, corresponding to 10–426 electrical discharges. The red crosses depict outliers to the statistics.

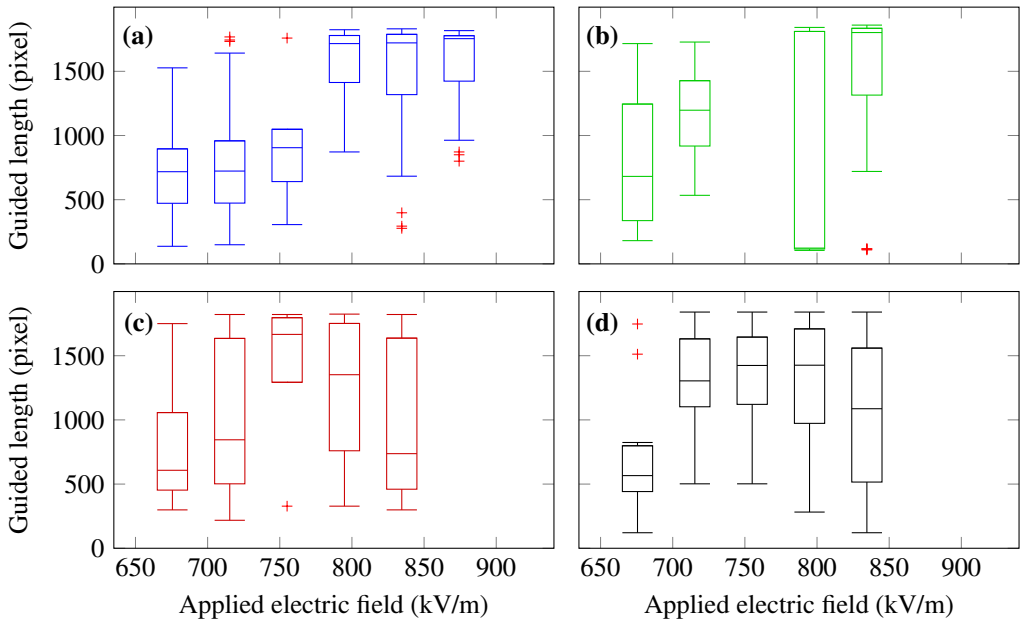

Figure 7.6: Guided length of electrical discharges on pictures for the UV only (a) and the added 532 nm (b), 1064 nm (c) and both nanosecond lasers. A third of the laser shots treated in Figure 7.5 are used for this statistics. The red crosses depict outliers to the statistics.

field is plotted on Figure 7.5a. At electric fields under 755 kV/m, the median delay time is around 5 µs. A threshold occurs at 755 kV/m and above this electric field, the median delay between the electric breakdown and the laser pulse is reduced to 2 µs. The threshold between the two delay ranges moves to lower electric fields when the near-infrared pulse is added to the ultraviolet pulse (Figure 7.5c). As a result, the delay between the laser and the discharge at 755 kV/m is divided by two when the 1064 nm nanosecond pulse is added to the ultraviolet pulse. As no data was recorded at 755 kV/m in Figure 7.5b when the 532 nm was added to the ultraviolet beam, it is difficult to say whether the green beam has an impact on the threshold. On the other hand, adding both 532 nm and 1064 nm to the 266 nm beam clearly moves the threshold further to low electric fields (Figure 7.5d), as the longer delay only occurs for the lowest electric field applied in this experiment.

This regime change coincides with the electric field for which the laser filament mainly guides the electric breakdown, as evidenced on Figure 7.6. A picture of every third laser shot was taken and the guided length of the discharges was calculated for each laser condition for data sets where no delay was applied between the laser beams. The guiding efficiency is especially well illustrated in the case of the ultraviolet beam alone (Figure 7.6a) and in the case of all three beams together (Figure 7.6d), which are also the best conditions to observe the threshold in triggering of the discharges on Figure 7.5.

This observation is consistent with La Fontaine *et al.* (2000) who report that guided leaders propagate approximately ten times faster than natural electric discharges ($\sim 10^6$ m/s vs $\sim 10^5$ m/s over a 2 m gap in 0.6 MV/m). They show that as soon as the leader is guided in the filament, its speed increases drastically. A longer guided path in this experiment therefore corresponds to a shorter time between the laser pulse and the induced current recorded on the oscilloscope.

This reduction of the laser-triggered breakdown time threshold may be explained by the interplay between the avalanche ionization and the electron-ion recombination rates calculated with the plasma evolution code presented in Chapter 5. While the avalanche rate increases by almost 50 % when both 532 nm and 1064 nm beams are added to the 266 nm beams, the electron-ion recombination only increases by at most 25 %. This leads to an increase in the electron concentration when the nanosecond pulses are added to the ultraviolet beam. In turn, this could help the discharge triggering at lower electric field, hence lower corona levels, but the effect being small, this does not show on the discharge probability. Between the green and the infrared nanosecond pulses, the infrared one is 40 % more efficient to increase the avalanche rate.

This shows that adding nanosecond pulses to an ultraviolet laser filament does accelerate the discharge speed and its guiding although it does not significantly change the discharge probability.

7.3 Conclusion

In this chapter, the very high electrical discharge triggering efficiency of ultraviolet filaments was demonstrated. As the discharge triggering is already as efficient with ultraviolet laser filaments alone than when a nanosecond pulse is added to the near-infrared filaments, adding pulses to heat up the ultraviolet filament induced electron plasma only improves the discharge speed and guiding. Two typical delay times between the laser pulse and the electrical breakdown were evidenced, corresponding to the guiding efficiency of the laser filament. The electrical breakdown is therefore approximately twice faster when the laser filaments guide the breakdown as when the electric arc follows a random path. The guiding efficiency is improved by adding two respectively green and infrared nanosecond pulses to the ultraviolet filaments, most of the discharges being

guided at electric fields 15 % lower than when the ultraviolet filaments are sent alone.

The main drawback of ultraviolet filaments is the difficulty to have powerful ultrashort laser sources in those wavelengths due to diffraction losses and absorption of ozone at 266 nm, leading to difficult beam propagation. This could also be problematic for real-scale experiments to trigger discharges from clouds but as the discharge triggering efficiency is very high, it could be worth pursuing in this direction. In particular, propagating trains of pulses in the ultraviolet as suggested in the near-infrared in Chapter 5 could therefore bring interesting results in the future as already hinted by the results of Zvorykin *et al.* (2015b) with amplitude-modulated ultraviolet laser filaments with pulsed high-voltage sources.

Conclusion

This work is focused on different applications of ultrashort laser pulses in atmospheric physics, from the propagation of laser filaments in the atmosphere to laser-induced aerosol formation and interactions between laser filaments and electric fields.

We have shown with the TERAMOBILE laser system that the laser beam intensity drives the geometrical pattern of multiple filaments propagating in the atmosphere and an analogy to gas-solid phase transition has be made, where the laser beam intensity plays the role of the pressure in solid state physics.

We investigated the effect of externally imposed and self-induced turbulence on the propagation of laser filaments in a collaboration with TRUMPF Scientific Lasers in Munich (DE). The self-induced turbulence from the laser filament appears to be a few orders of magnitude slower than the atmospheric turbulence. Moreover, these two timescales can be decoupled even for turbulences much stronger than that observed outdoors. Adaptive optics could thus compensate the self-induced turbulence. We also showed that high repetition rate lasers are very useful to clear a channel through a dense fog, much larger than the filament cross-section, by generating a shock wave that expels the cloud droplets from the beam propagation path. This is very promising for their use in free space communication or for lightning control.

Laser filaments have also been proven to generate aerosols upon which water can condensate. In collaboration with the group of Professor A. Baltuška in Vienna (AU), we have presented first results of laser-induced aerosol condensation with laser filaments in the mid-infrared, which are expected to be wider and propagate on distances much longer than their near-infrared counterparts. The condensation efficiency at 4 µm is surprisingly high as the photo-ionization and photo-dissociation processes dominant at 800 nm are too weak in the mid-infrared. The broad spectrum in the mid-infrared covers the C−H band around 3.3 to 3.6 µm in volatile organic compounds. The energy at these wavelengths could be sufficient to pump efficiently resonant excitations by ladder-climbing and ultimately photo-dissociate the C−H bonds. This could lead to formation of different hygroscopic species at 4 µm than at 800 nm. Further experiments are needed to assess the aerosol composition and confirm this hypothesis.

An analysis of the laser filaments electric characterization demonstrated that probing the ionic current flowing to the electrodes positioned perpendicular to the laser beam is very robust against misalignments. This technique is however not representative of the initial electron density, but rather proportional to the ion concentration, which lasts much longer. The free electron density in the filament volume can be better characterized by using electrodes in a longitudinal configuration. Linearity is however only valid for electric fields below 100 kV/m as avalanche ionization distorts the results at higher electric fields.

In order to improve the electric properties of laser filaments over longer timescales, we investigated the best energy partitioning available in a given laser pulse in a collaboration with

Amplitude Systèmes in Bordeaux (FR). We showed that trains of ultrashort pulses bearing each enough energy to create a single filament and separated by a few nanoseconds in time could be more efficient to create long lifetime plasma channels than if all the energy was sent in one single pulse, leading to a bundle of multiple filaments.

We demonstrated that at high repetition rates, the natural breakdown can be suppressed by the unloading of the electrodes by the laser filament. Also, at low electric fields, charges can be moved from one capacitor to another one without creating an electrical breakdown between them. The ability of a laser filament to unload a charged capacitor is surprisingly efficient, even when the electrode is several centimeters away from the laser filament. It would be very interesting to dimension the laser properties needed to achieve such arc suppression in real scale.

Finally, we proved in a collaboration with the group of Professor J.-C. Diels in New Mexico (USA) that discharge triggering and guiding by laser filaments of 270 mJ at 266 nm is much more efficient than in the near-infrared. We also demonstrated that adding 1.1 J of 1064 nm and 0.8 J of 532 nm nanosecond pulses to the ultraviolet ultrashort pulse was not sufficient to increase the discharge triggering probability. However, it increased significantly the guided length and the velocity of the electrical arc. A further study of the length increase with respect to the long pulse energy could indicate the energies needed for a long distance electrical arc triggering and guiding effect.

This work draws perspectives for extending the range and efficiency of laser-assisted condensation and lightning control.

Non-Linear Photochemical Pathways in Laser-Induced Atmospheric Aerosol Formation

A

www.nature.com/scientificreports

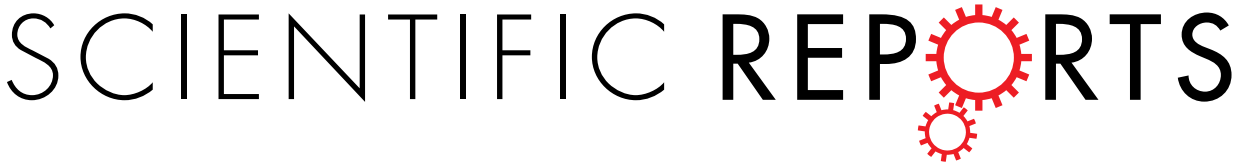

OPEN

Non-linear photochemical pathways in laser-induced atmospheric aerosol formation

Received: 22 June 2015
Accepted: 15 September 2015
Published: 09 October 2015

Denis Mongin[1], Jay G. Slowik[2], Elise Schubert[1], Jean-Gabriel Brisset[1,3], Nicolas Berti[1], Michel Moret[1], André S. H. Prévôt[2], Urs Baltensperger[2], Jérôme Kasparian[4] & Jean-Pierre Wolf[1]

We measured the chemical composition and the size distribution of aerosols generated by femtosecond-Terawatt laser pulses in the atmosphere using an aerosol mass spectrometer (AMS). We show that nitric acid condenses in the form of ammonium nitrate, and that oxidized volatile organics also contribute to particle growth. These two components account for two thirds and one third, respectively, of the dry laser-condensed mass. They appear in two different modes centred at 380 nm and 150 nm. The number concentration of particles between 25 and 300 nm increases by a factor of 15. Pre-existing water droplets strongly increase the oxidative properties of the laser-activated atmosphere, substantially enhancing the condensation of organics under laser illumination.

Self guided filamentation[1–5] of high-power femtosecond laser pulses results from a dynamic balance between the Kerr effect which tends to self-focus the laser beam on one side, and the plasma created by the strong electric field, as well as higher-order polarisation saturation effects[6,7] on the other. The resulting filaments can propagate beyond 100 m in the atmosphere[8], be created remotely[9], and withstand adverse atmospheric conditions like clouds[10] or turbulence[11,12]. This non-linear propagation regime is of particular interest for atmospheric applications[13] such as remote sensing[14], air lasing[15,16], triggering of high voltage discharges[17–19] and lightning control[20]. The most striking effect of laser filaments in the atmosphere is laser-induced condensation[21–26], where the plasma photochemistry induced by laser filaments leads to nucleation of new particles[27] and their subsequent growth[22,28].

Both laboratory and field studies have shown that laser-induced condensation is associated with the production of locally high ozone and NO_x concentrations in the gas phase. Furthermore, ion chromatography of laser-produced particles sampled on filters has shown substantial amounts of NO_3^- ions in the laser-condensed particles[22,29]. The formation of highly hygroscopic HNO_3 has therefore been identified as one major pathway to support laser-induced condensation of aerosol mass, for relative humidity (RH) in atmosphere higher than 70%[22]. Moreover, ppb-range traces of atmospheric SO_2 have also been shown to favour laser-induced nucleation of new particles, increasing the number concentration by typically one order of magnitude but without significant total aerosol mass increase. Conversely, laboratory experiments in a cloud chamber showed that ppb-range concentrations of volatile organic compounds (VOCs) lead to an increase in the concentration of laser-induced particles for sizes up to some hundreds nanometers, together with an increase of the condensed mass[27]. This suggests that they both contribute at least to the initial phases of the nucleation but that mostly organic compounds condense on bigger particles. However, very little was known to date about the actual composition of the laser-induced aerosol mass, which is needed to identify the physico-chemical pathways.

[1]Université de Genève, GAP-Biophotonics, Chemin de Pinchat 22, CH-1211 Geneva 4, Switzerland. [2]Paul Scherrer Institute, Laboratory of Atmospheric Chemistry, CH-5232 Villigen, Switzerland. [3]Max-Born-Institut, Max-Born-Strasse 2A, 12489 Berlin, Germany. [4]Université de Genève, GAP-Non-linear, Chemin de Pinchat 22, CH-1211 Geneva 4, Switzerland. Correspondence and requests for materials should be addressed to J.K. (email: jerome.kasparian@unige.ch)

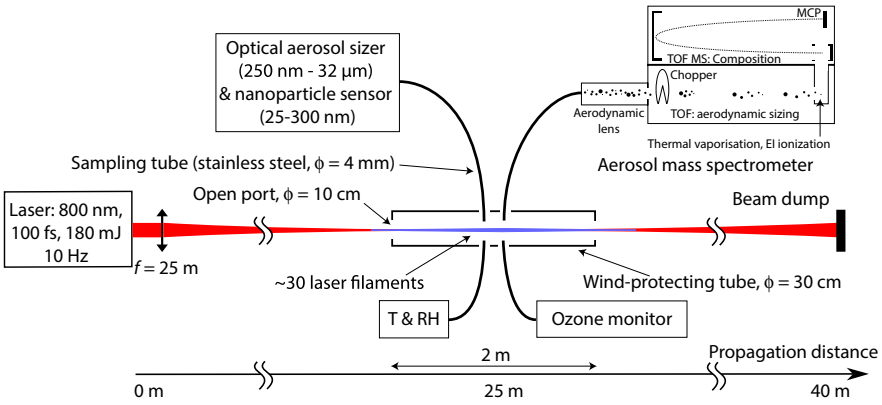

Figure 1. Experimental setup. TOF: Time of flight; MS: Mass spectrometer; EI: Electron impact; MCP: Micro-channel plate.

Here, we present a detailed chemical characterization of laser-induced aerosols in the real atmosphere. An aerosol mass spectrometer is used to investigate the influence of laser filamentation on ambient particle composition and size distributions. We show that condensation indeed occurs in the atmosphere under illumination by laser filaments, leading to an increase of the total aerosol mass and the appearance of a new size mode. Furthermore, we demonstrate the key contributions of ammonium nitrate (rather than nitric acid, as previously expected), and to a lesser extent, of organics, to the laser-condensed mass. Finally, we show that continuously spraying pre-existing water droplets into the laser beam strongly increases the oxidative properties of the laser-activated atmosphere, substantially enhancing the condensation of organics under laser illumination.

The experimental setup is sketched in Fig. 1. The Teramobile[29] Ti:sapphire laser delivers Fourier-limited, 180 mJ and 80 fs pulses centered at 800 nm at a repetition rate of 10 Hz. The pulses are loosely focused by an $f = 25$ m telescope into the atmosphere. At the focus, the beam has a waist of around 5 mm (HWHM) and contains ~30 filaments of about 100 μm in diameter each. The focal region is shielded from the wind by an open, galvanized iron tube of 30 cm diameter.

The atmosphere is monitored in the filamenting region at 1 cm side distance from the laser beam by an Aerodyne high-resolution time-of-flight aerosol mass spectrometer (AMS), an optical aerosol sizer, a nanoparticle sensor, and an ozone detector (see Materials and Methods). Additionally, temperature and RH were continuously monitored at the sampling location of these instruments. Unless otherwise specified, the relative humidity was between 80% and 100% during the measurements.

Each experiment consists of a series of 2 to 5 cycles of reference (laser off) and active (laser on) periods of about 15 minutes. The shielding tube is flushed with fresh air from the open atmosphere before each laser-on time period. Besides the nominal conditions described above, we investigated the effect of spraying water droplets in the experimental region using a nebuliser.

We aim at comparing the composition of the pre-existing atmospheric aerosols with those formed under the influence of the laser filaments. We therefore focused on steady-state situations, by averaging the measured size distributions and species concentrations over the active and reference periods. We corrected the measurement baseline for the slow drift of temperature and RH during the experiments. To avoid interference from the transient behaviours of both the instruments and the atmosphere just after starting or stopping the laser, we discarded the time interval of $\Delta t = 4$ min at the beginning of each period. This ensures that the average over the remaining time period is stable within 3 standard deviations of the mean. When needed, the effect of the laser was assessed by performing a Student test for the comparison of results from the active and reference periods. Significance is considered achieved for confidence levels of 99% or beyond ($\alpha \leq 0.01$).

Results

Aerosol mass increase. The presence of the laser filaments results in a clear increase of the total aerosol mass concentration. As displayed in Fig. 2(a), this increase reaches a factor of 14 in the case of the 25–300 nm particles (~80 nm median diameter). Simultaneously, the concentration of particulate matter with an optical diameter of 250 nm to 1 μm or 2.5 μm (PM1 and PM2.5, respectively) increases by almost 20%, while the AMS measures a 40% increase of the total dry mass (sum of sulfate, nitrate, organics, ammonium and chloride) for aerodynamic diameters between 60 and 600 nm. Such values are in line with previous measurements in the atmosphere[22]. This rise is quite evenly spread over the size classes ranging from 300 to 600 nm, with a statistically significant increase of up to 25% for 300 nm particles (Fig. 3(a)). The large error bars in Figs 2 and 3(c) are primarily due to fluctuations of the laser pulse energy (up to 20%, amplified by the non-linear propagation), the fluctuations of the atmosphere around

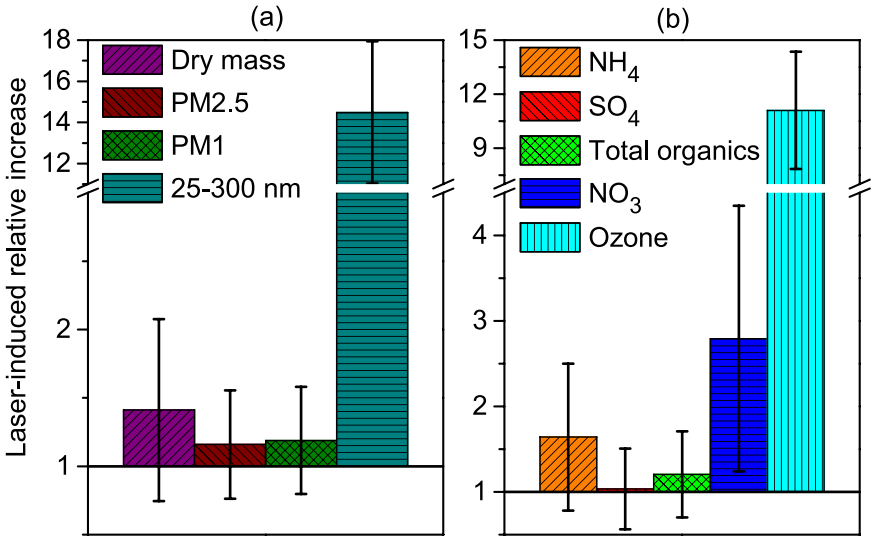

Figure 2. Laser-induced relative increase of (**a**) the aerosol dry mass concentration measured by the AMS (sum of sulfate, nitrate, organics, ammonium and chloride for vacuum aerodynamic diameters between 60 and 600 nm), the PM1 and PM2.5 mass concentration measured by the optical sizer and the number concentration of 25 to 300 nnm particles detected by the nanoparticle sensor, and (**b**) the mass concentration of several condensable components detected by the AMS, as well as atmospheric ozone concentration. Error bars correspond to the sum of the relative standard deviations of the values measured with and without laser.

the laser during the measurements, as well as air currents in the wind-protecting tube (See Fig. 1), which alter the efficiency with which laser-generated mass is sampled. Despite these, the results retain statistical significance. Note however that the error bars on the ratios are calculated as a worst-case scenario by adding the relative errors on each term, providing an upper limit to them.

Size distribution. By looking at the total mass detected by the AMS (sum of the nitrate, sulfate, organics, ammonium and chloride), one can see the appearance of a new mode (Aitken mode) centered around 150 nm in the dry particle size distribution when the laser is turned on (Fig. 3(c,d)). This mode could be formed either by nucleation or by growth of nanometric pre-existing particles. Simultaneously, the accumulation mode centered at 380 nm increases by 25%, as also observed in the total mass size distribution. In spite of their different particle sizes, both modes contribute about half of the total laser-induced mass condensation (Fig. 4(c)).

Chemical composition of laser-induced aerosols. Beyond the total particle mass and number concentrations, the aerosol mass spectrometer allows identifying and quantifying the main components that substantially contribute to the laser-induced condensation. The condensed mass of NO_3^- increases by a factor of 2.8, NH_4^+ by 60%, and organics by 20% (Fig. 2(b)). Considering their original mass fraction in the aerosols (Fig. 4(a), right column), these components contribute 50%, 20%, and 28% of the net laser-induced increase of the dry mass (Fig. 4(c), right column). These contributions to the laser-condensed mass are comparable in both size modes.

In contrast, no evidence for significant laser-induced SO_4^- condensation is observed, consistent with the concentration of SO_2 in the atmosphere during the experiment of 2 μg/m^3 (as measured by the Geneva city air quality monitoring network[30]).

Oxygenation of the organic fraction of the aerosols. The AMS allows detailed analysis of the organic aerosol composition. More specifically, oxygenated organic aerosol (OOA) can be described as highly oxygenated, low-volatility (LV-OOA), or less oxygenated semi-volatile OOA (SV-OOA)[32,33]. Considering the mass to charge (m/z) values of 44 (corresponding in particular to CO_2^+) and 43 (mainly $C_2H_3O^+$), as representative of these two categories respectively, we investigated their relative contributions, hereafter denoted $f44$ and $f43$, to the total organic mass condensed in the aerosols.

During the experiment, the laser condensed mass presents an $f44$ and $f43$ respectively 25% and 11% lower than in the pre-existing atmospheric aerosol (Fig. 5(a)). This oxygenation state of the laser-condensed organic mass is similar to typical ambient OOA[31,32].

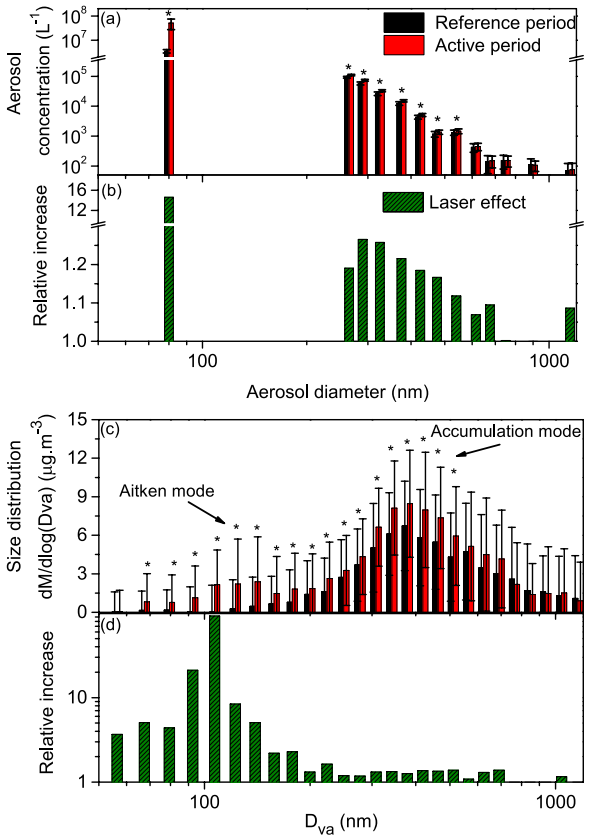

Figure 3. Evolution of the aerosol size distribution under laser illumination. (**a**) Aerosol size distribution between 250 and 900 nm during both reference and active periods measured by the Grimm optical particle sizer, and concentration of 25–300 nm particles measured by the Nanocheck (column centered at the mean diameter 80 nm); (**b**) Corresponding relative increase induced by the laser; (**c**) Dry particle size distribution (total mass detected by the AMS, calculated as the sum of nitrate, sulfate, organics, ammonium and chloride) during both reference and active periods and (**d**) Corresponding relative increase induced by the laser. D_{va} is the vacuum aerodynamic diameter. Stars denote size classes where the effect of the laser is statistically significant ($\alpha \leq 0.01$, see text for details). Error bars correspond to one standard deviation.

The laser produces highly oxidative conditions, with the generation of local concentrations of O_3 up to the 100 ppm range[33,34] (see also Fig. 2) and ppbs of $^{\bullet}OH$ radicals in the filaments[35]. These conditions produce OOA with a composition on the boundary of LV-OOA and SV-OOA from the gaseous organics within a few seconds.

Spraying water droplets to a low RH atmosphere. In an atmosphere with 50% RH, the laser doesn't condense any mass, and the ambient aerosol is mainly composed of organics (68%), SO_4 (19%), NH_4 (8%) and a small percentage of NO_3 (5%). Continuously spraying water particles close to the laser focus caused the laser to condense mass (as evidenced by a mass increase of 8%), mainly composed of organics (85%). Furthermore, the oxygenation of the laser-condensed organics is higher than the pre-existing ones in this case, as evidenced by the increase of the highly oxygenated organics (see *f*44 in Fig. 5(b)) while the less oxygenated organics (*f*43) simultaneously decrease. The huge amount of $^{\bullet}OH$ produced by the interaction of the water droplets with the laser filaments results in the production of LV-OOA, much more oxygenated than in the main experiment. Conversely, no condensation of hygroscopic species occurs despite the huge amount of water sprayed, indicating that the latter is not available for laser-induced condensation.

Influence of laser pulse energy. We investigated the effect of the laser pulse energy on the efficiency of laser-induced condensation. Reducing the laser pulse energy from 180 mJ to 110 mJ did not visibly alter the effect of the laser on ambient aerosol. In contrast, at 55 mJ per pulse no effect on the ambient aerosol (i.e. no production of aerosol mass) was observed.

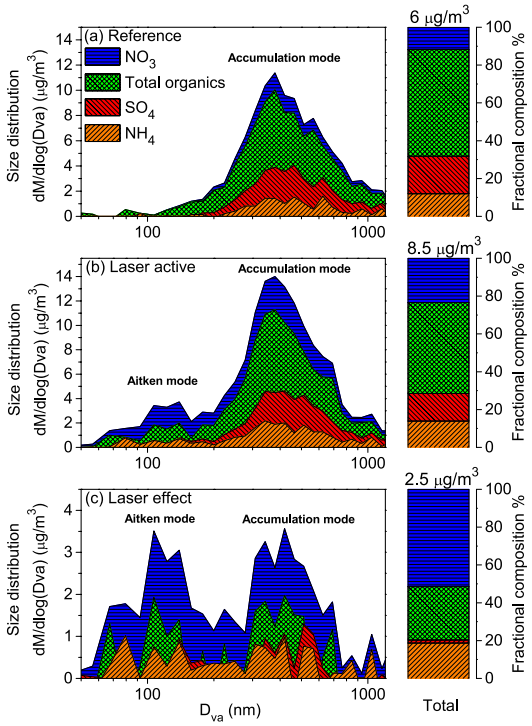

Figure 4. Mass distribution of the measured condensable species within the size distribution during (**a**) the reference period and (**b**) the laser active period. (**c**) Difference between the active and reference periods, displaying the condensation effect of the laser. D_{va} is the vacuum aerodynamic diameter.

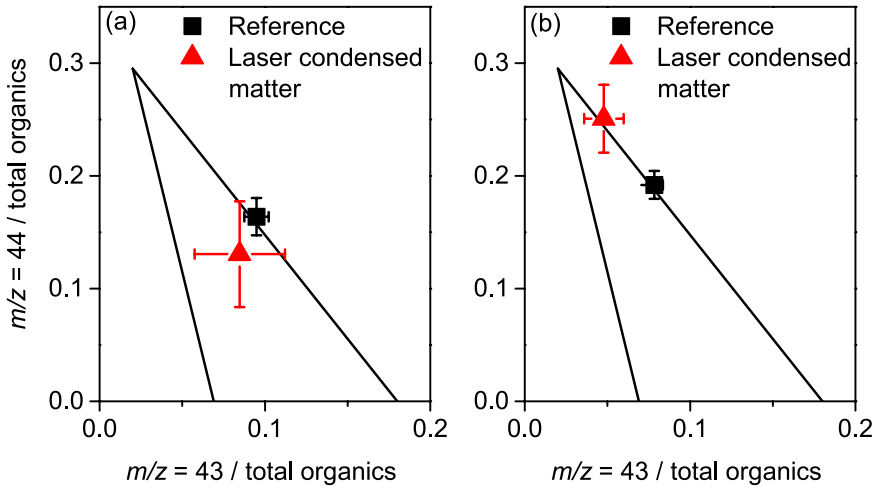

Figure 5. Fraction of highly ($m/z=44$, mainly CO_2^+) and less oxygenated ($m/z=43$, mainly $C_2H_3O^+$) organics among the total organics, in particles detected during the reference period (black) and the laser-condensed particles, that is the difference of measurement with and without the laser (red), for (**a**) the main experiment and (**b**) when spraying water in a low RH atmosphere (**b**). The two black lines encompass the region where most atmospheric data are found to date[31,32].

Discussion

Laser-induced condensation. The formation of a new Aitken mode accounting for 50% of the laser-condensed dry mass together with the increase of the pre-existing mode provides a clear evidence

of the condensation induced by the laser filaments in the atmosphere, an effect that had only been characterised before in laboratory conditions[27]. The formation of new particles by nucleation or growth of pre-existing nanometric particles, as opposed to shattering of larger particles, is confirmed by the increase of the total mass of aerosol detected during the experiment, by the change of chemical composition of their dry mass, and by the lower oxygenation level of the organics contained in the particles detected under laser illumination.

Condensation of ammonium nitrate. The concentration of NO_3 and NH_4 observed in the laser-induced aerosols (50% and almost 20% of the dry condensed mass, respectively, i.e., a total contribution close to 70%) sheds new light on the previously inferred binary water-HNO_3 condensation under laser illumination. The 0.31 mass ratio of NH_4 to NO_3 in the dry condensed mass (Fig. 4), in both the nucleation mode and accumulation modes, is consistent with that of NH_4NO_3. One can therefore expect that the hygroscopic HNO_3 previously identified to assist the condensation of water[22,28] is not condensed, as initially expected, as nitric acid in a binary mixture with water, but rather as hygroscopic ammonium nitrate through the reaction[36]

$$NH_3 + HNO_3 \rightleftharpoons NH_4NO_3 \quad (1)$$

NH_3 is typically available as background trace gas in the summer sub-urban atmosphere of the experiment location in amounts of several $\mu g/m^3$ [37]. This concentration is comparable with the laser-condensed mass of NH_4^+, suggesting that the laser-induced condensation relies on the condensation of pre-existing ammonia together with HNO_3. The latter is generated via the interaction of NO_x produced by the multi-photon ionisation of N_2 with O_3[33] or $^{\bullet}OH$ radicals[35], both produced by the multiphoton absorption and photolysis of O_2. The very low efflorescence of ammonium nitrate and the high quantities of NH_4NO_3 in the laser condensed mass suggest that there is always water in the laser induced aerosols. Besides, it validates a posteriori the *ad hoc* introduction of ammonium nitrate for modelling the growth of laser-induced particles[28].

Organics. Besides ammonium nitrate, the laser mainly condenses organics (28% of the dry mass). The amount of organics condensed by the laser seems to be driven by its ability to create an oxidative atmosphere. At normal atmospheric conditions and when RH is above 70%, the laser partly oxidises organics, resulting in the condensation of typical ambient LV/SV-OOA, slightly less oxygenated than the pre-existing organic aerosol during our experiment. This suggests that new aerosol mass is formed by the laser from the semi-volatile organics available in the gas phase, and not from the already condensed non-volatile species. The absolute amount slightly below $1\,\mu g/m^3$ of organics condensed by the laser constitutes a few percent of the total concentration of VOCs available in a typical urban atmosphere[38], confirming the VOC availability for laser-induced oxidation and condensation.

When water is sprayed around the laser filaments at an original RH lower than 70%, the proportion of organics in the dry mass drastically increases (80% of the dry mass). Given that no relative humidity change was observed when spraying water during this particular experiment, we attribute this effect to the interaction of the water droplets sprayed into the laser beam, with the laser filaments. Considering their high concentration during the experiment, about 100 water droplets interact with the laser filaments for each laser pulse. These water droplets then internally focus the incident laser light on a nanometric hot spot, where the extreme incident intensity (in the $10^{15}\,TW/cm^2$ range) will efficiently ionize water[39]. This ionization produces a concentration of $^{\bullet}OH$ radicals much higher than in normal atmospheric conditions, leading to efficient oxidization of the available organics. The resulting highly oxygenated, low volatility organics then efficiently condense onto particles with a high oxygenation state comparable to that of α-pinene particles after exposure to 500 ppb of O_3 during 13 hours[31,32,40]. This very fast oxidization illustrates again the extreme conditions locally produced by the laser filaments.

Our results evidence the dual role of organics in laser-induced condensation. While they had been shown to promote nucleation in a background-free atmosphere[27], we show that they also substantially contribute to the particle growth up to at least 600 nm in diameter (see Fig. 4).

Sulfate. Sulfuric acid is known to provide one of the main sources of condensation nuclei in the atmsophere[36]. In the case of laser-induced nucleation, experiments in a cloud chamber showed that sulfuric acid does not only drastically enhance the number density of nucleated particles, but also the total condensed mass[27]. The very low mass fraction of sulfate ions in the laser-induced condensed mass ($<2\%$) detected during our experiment can be explained by the low ambient SO_2 concentrations during the study. In this case, its role is restricted to the formation of small condensation nuclei, most probably together with oxidized organics[41].

Laser energy. The energy dependence of the efficiency of laser-induced condensation appears to display a threshold between 50 and 110 mJ. This suggests that the effect of the laser can be understood by considering the interplay between two phenomena.

On one side, the efficiency of the plasma photochemistry increases non-linearly with increasing incident laser pulse intensity. At 800 nm, the photolysis of O_2, its ionization, and that of N_2 respectively

require 4, 8, and 11 photons[3]. The associated efficiencies therefore depend on the corresponding powers of the laser input intensity, so that the condensation mechanisms initiated by these processes will successively come into play when the laser energy rises. This results in the observed dependence with the pulse energy. On the other side, however, particle formation and growth requires the availability of condensable species in the volume swept by the high intensity laser, or at reach within a reasonable transport time. As this transport mainly occurs by diffusion, which is very slow for distances beyond the mm-range, diffusion constitutes the limiting factor to condensation when the laser pulse energy is further increased.

This finding illustrates that increasing the magnitude of the laser effect requires to increase the activated volume, by either increasing the beam diameter, or by steering the beam dynamically.

Conclusion

We simultaneously measured the size distribution and the quantitative size resolved aerosol composition by mass spectrometry during laser-induced condensation in the real atmosphere. We obtained direct evidence of laser-assisted condensation in real atmosphere, with a 40% increase of aerosol total mass and a 15-fold increase in the particle number concentration between 25 and 300 nm. Furthermore, we observed the condensation of hygroscopic NH_4NO_3 accounting for two thirds of the laser-condensed mass. This abundance shows that NO_3 condenses as ammonium nitrate, rather than as nitric acid as previously expected. The rest of the laser-condensed dry mass is mainly provided by organics, accounting for as much as 28%, evidencing their role in the particle growth. The presence of these two components (ammonium nitrate and organics) can be attributed to two main condensation mechanisms related to the production of nitrogen oxides, ozone and $^{\bullet}OH$ radicals by the interaction of the filaments with the atmosphere. The first one consists of the generation of HNO_3, which then condenses in a ternary system together with NH_3 and water to form NH_4NO_3 in the laser-induced particles. The second one is the oxidation of volatile organics by $^{\bullet}OH$ radicals and O_3 into less volatile organics which condense on the pre-existing particles. Moreover, the oxidation as well as the degree of oxygenation of organics can be strongly increased by the presence of pre-existing water droplets because of increased $^{\bullet}OH$ radical concentrations due to internal focusing of the laser light within the droplets. Our work therefore offers a global picture of the complex mechanisms at play in laser-induced condensation.

Methods

Teramobile laser. The Teramobile[30] is a Ti:sapphire laser delivering 80 fs pulses of 180 mJ, at a repetition rate of 10 Hz with a wavelength centered at 800 nm. The beam is sent horizontally into the open atmosphere, 120 cm above ground. It has an initial diameter of 7.5 cm and is loosely focused by an $f = 25$ m telescope. The beam at the focus has a waist of around 5 mm (HWHM) and contains ~30 filaments. The beam is blocked by a screen after a further 15 m of propagation to avoid any interference by particles ablated from this beam dump.

Wind-protecting tube. The region around the focus is shielded from wind by a 2 m long, 30 cm diameter galvanized iron tube. It is open at each end, with 10 cm diameter ports letting both the laser beam get through and exchanges with the free atmosphere to occur. The detection instruments continuously monitored the atmosphere at 1 cm distance from the laser beam close to the filaments, via 1.5 m-long, 4 mm inner diameter copper sampling tubes connected to the center of this shielding tube.

AMS. Size-resolved non-refractory particle composition was measured using an Aerodyne high-resolution time-of-flight aerosol mass spectrometer (AMS)[42,43]. Briefly, the AMS continuously samples particles from ambient air (0.8 L/min) through a 100 μm critical orifice into an aerodynamic lens (2 torr). Here the particles are focused into a narrow beam and accelerated to a velocity that is inversely related to their vacuum aerodynamic diameter. The particle beam can be either alternately blocked and unblocked (yielding ensemble mass spectra of the incident aerosol), or modulated by a spinning chopper wheel (150 Hz), yielding size-resolved mass spectra at the cost of lower sensitivity. The particle ionisation on a resistively heated surface (600 °C, 10^{-7} torr), where the non-refractory components flash vaporize, are ionized by electron impact (70 eV) and are detected by time-of-flight mass spectrometry. The AMS can detect most atmospherically-relevant species except for black carbon and mineral dust, while water is not quantitatively detected due to high instrument backgrounds and uncertainty over the fraction of water that evaporates in the aerodynamic lens. The lens has unit transmission efficiency for particles with vacuum aerodynamic diameters between 100 and 600 nm, and approximately 10% transmission of 50 and 1000 nm particles[44]. Mass spectra are analyzed and quantitatively split into e.g. nitrate, sulfate, ammonium, and organics using the standard fragmentation table-based analysis of Allan *et al.*[45]. Depending on the experiment, the AMS was operated with either 1 min or 20 sec time resolution.

Particle sizer. The aerosol sizer is a Grimm 1.109 measuring the aerosol size distribution by optical scattering in 31 classes ranging from 250 nm to 30 μm. This instrument samples 1.5 L/min and provides measurement at a temporal resolution of 6 s, although the overall reaction time of the instrument and the associated sampling tube can be estimated to lie in the 8 s range. It also integrates the size distribution up to 1 and 2.5 μm diameter, respectively, to estimate the PM1 and PM2.5 mass concentration in air.

Nanoparticle sensor. A nanoparticle sensor (Grimm Nanocheck 1.365) measures the 25–300 nm particle number density. Sampling flow and temporal resolution are the same as the above particle sizer.

Ozone detector. The ozone detector is a Horiba APOA-350E and sampled the atmosphere at a rate of 2 L/min, measuring ozone concentration with a temporal resolution of 20 s.

Temperature and RH probe. The device monitoring temperature and RH is a Testo 635-2 device. Its probe is located at the same place as the other instruments.

Nebuliser. The nebuliser used to spray water is a TSI 3076 nebuliser equipped with a 3074B air filter. The corresponding size distribution was centred around 1.5 μm, with a geometric standard deviation smaller than 2.

References

1. Kelley, P. Self-focusing of optical beams. *Phys. Rev. Lett.* **15,** 1005–1008 (1965).
2. Braun, A. *et al.* Self-channeling of high-peak-power femtosecond laser pulses in air. *Opt. Lett.* **20,** 73–75 (1995).
3. Couairon, A. & Mysyrowicz, A. Femtosecond filamentation in transparent media. *Phys. Rep.* **441,** 47–189 (2007).
4. Bergé, L., Skupin, S., Nuter, R., Kasparian, J. & Wolf, J. Ultrashort filaments of light in weakly-ionized, optically-transparent media. *Rep. Prog. Phys.* **70,** 1633–1713 (2007).
5. Chin, S. L. *et al.* The propagation of powerful femtosecond laser pulses in optical media: physics, applications, and new challenges. *Can. J. Phys.* **83,** 863–905 (2005).
6. Béjot, P. *et al.* Higher-order kerr terms allow ionization-free filamentation in gases. *Phys. Rev. Lett.* **104,** 103903 (2010).
7. Béjot, P. *et al.* Transition from plasma- to kerr-driven laser filamentation. *Phys. Rev. Lett.* **106,** 243902 (2011).
8. La Fontaine, B. *et al.* Filamentation of ultrashort pulse laser beams resulting from their propagation over long distances in air. *Phys. Plasmas* **6,** 1615–1621 (1999).
9. Rodriguez, M. *et al.* Kilometer-range nonlinear propagation of femtosecond laser pulses. *Phys. Rev. E* **69,** 036607 (2004).
10. Méjean, G. *et al.* Multifilamentation transmission through fog. *Phys. Rev. E* **72,** 026611 (2005).
11. Chin, S. L. *et al.* Filamentation of femtosecond laser pulses in turbulent air. *Appl. Phys. B* **74,** 67–76 (2002).
12. Salamé, R., Lascoux, N., Salmon, E., Kasparian, J. & Wolf, J. Propagation of laser filaments through an extended turbulent region. *Appl. Phys. Lett.* **91,** 171106–171106 (2007).
13. Kasparian, J. & Wolf, J.-P. Physics and applications of atmospheric nonlinear optics and filamentation. *Opt. Express* **16,** 466–493 (2008).
14. Kasparian, J. *et al.* White-light filaments for atmospheric analysis. *Science* **301,** 61–64 (2003).
15. Dogariu, A., Michael, J. B., Scully, M. O. & Miles, R. B. High-Gain Backward Lasing in Air. *Science* **331,** 442–445 (2011).
16. Yao, J. *et al.* High-brightness switchable multiwavelength remote laser in air. *Phys. Rev. A* **84,** 051802 (2011).
17. Zhao, X., Diels, J., Wang, C. & Elizondo, J. Femtosecond ultraviolet laser pulse induced lightning discharges in gases. *IEEE J. Quantum Electron.* **31,** 599–612 (1995).
18. Pépin, H. *et al.* Triggering and guiding high-voltage large-scale leader discharges with sub-joule ultrashort laser pulses. *Phys. Plasmas* **8,** 2532–2539 (2001).
19. Kasparian, J. *et al.* Megavolt discharges triggered and guided with laser filaments. *Opt. Lett.* **27,** 772–774 (2002).
20. Kasparian, J. *et al.* Electric events synchronized with laser filaments in thunderclouds. *Opt. Express* **16,** 5757–5763 (2008).
21. Rohwetter, P. *et al.* Laser-induced water condensation in air. *Nature Photon.* **4,** 451–456 (2010).
22. Henin, S. *et al.* Field measurements suggest the mechanism of laser-assisted water condensation. *Nature Comm.* **2,** 456 (2011).
23. Kasparian, J., Rohwetter, P., Wöste, L. & Wolf, J. Laser-assisted water condensation in the atmosphere: a step towards modulating precipitation? *J. Phys. D: Appl. Phys.* **45,** 293001 (2012).
24. Leisner, T. *et al.* Laser-induced plasma cloud interaction and ice multiplication under cirrus cloud conditions. *Proc. Nat. Acad. Sci.* **110,** 10106–10110 (2013).
25. Sun, H. *et al.* Laser filamentation induced air-flow motion in a diffusion cloud chamber. *Opt. Express* **21,** 9255–9266 (2013).
26. Ju, J. *et al.* Laser-induced supersaturation and snow formation in a sub-saturated cloud chamber. *Appl. Phys. B* **117,** 1001–1007 (2014).
27. Saathoff, H. *et al.* Laser filament-induced aerosol formation. *Atmos. Chem. Phys.* **13,** 4593–4604 (2013).
28. Rohwetter, P., Kasparian, J., Wöste, L. & Wolf, J. Modelling of HNO_3-mediated laser-induced condensation: A parametric study. *J. Chem. Phys.* **135,** 134703 (2011).
29. Wolf, J.-P. *et al.* Teramobile: a mobile femtosecond-terawatt laser and detection system. *Eur. Phys. J. - Appl. Phys.* **20,** 183–190 (2002).
30. Transalp' AIR. Indice de qualité de l'air. URL www.transalpair.eu. Date of access 24/08/2015.
31. Ng, N., Canagaratna, M., Zhang, Q., Jimenez, J. & Tian, J. E. A. Organic aerosol components observed in northern hemispheric datasets from aerosol mass spectrometry. *Atmos. Chem. Phys.* **10,** 4625–4641 (2010).
32. Ng, N. *et al.* Changes in organic aerosol composition with aging inferred from aerosol mass spectra. *Atmos. Chem. Phys.* **11,** 6465–6474 (2011).
33. Petit, Y., Henin, S., Kasparian, J. & Wolf, J. Production of ozone and nitrogen oxides by laser filamentation. *Appl. Phys. Lett.* **97,** 021108 (2010).
34. Camino, A., Li, S., Hao, Z. & Lin, J. Spectroscopic determination of NO_2, NO_3, and O_3 temporal evolution induced by femtosecond filamentation in air. *Appl. Phys. Lett.* **106,** 021105 (2015).
35. Matthews, M. *et al.* Cooperative effect of ultraviolet and near-infrared beams in laser-induced condensation. *Appl. Phys. Lett.* **103,** 264103 (2013).
36. Seinfeld, J. & Pandis, S. *Atmospheric Chemistry and Physics—From Air Pollution to Climate Change* (Hoboken, 2006), 2nd edition.
37. Thöni, L., Brang, P., Braun, S., Seitler, E. & Rihm, B. Ammonia monitoring in Switzerland with passive samplers: patterns, determinants and comparison with modelled concentrations. *Env. Monitoring Assess.* **98,** 93–107 (2004).
38. Derwent, R. G. *et al.* Twenty years of continuous high time resolution volatile organic compound monitoring in the United Kingdom from 1993 to 2012. *Atmos. Env.* **99,** 239–247 (2014).
39. Hill, S. C. *et al.* Enhanced backward-directed multiphoton-excited fluorescence from dielectric microspheres. *Phys. Rev. Lett.* **85,** 54–57 (2000).
40. Shilling, J. *et al.* Particle mass yield in secondary organic aerosol formed by the dark ozonolysis of α-pinene. *Atmos. Chem. Phys.* **8,** 2073–2088 (2008).

41. Riccobono, F. *et al.* Oxidation products of biogenic emissions contribute to nucleation of atmospheric particles. *Science* **344,** 717–721 (2014).
42. DeCarlo, P., Kimmel, J., Trimborn, A., Northway, M., Jayne, J., Aiken, A., Gonin, M., Fuhrer, K., Horvath, T., Docherty, K., Worsnop, D. & Jimenez, J. Field-deployable, high-resolution, time-of-flight aerosol mass spectrometer. *Anal. Chem.* **78,** 8281–8289 (2006).
43. Canagaratna, M. *et al.* Chemical and microphysical characterization of ambient aerosols with the Aerodyne aerosol mass spectrometer. *Mass Spec. Rev.* **26,** 185–222 (2007).
44. Liu, P. *et al.* Transmission efficiency of an aerodynamic focusing lens system: Comparison of model calculations and laboratory measurements for the aerodyne aerosol mass spectrometer. *Aerosol Sci. Technol.* **41,** 721–733 (2007).
45. Allan, J. *et al.* A generalised method for the extraction of chemically resolved mass spectra from Aerodyne aerosol mass spectrometer data. *J. Aerosol Sci.* **35,** 909–922 (2004).

Acknowledgements

D. Mongin acknowledges S. Hermelin for his permanent help and fruitful discussions. This research was supported by the ERC advanced grant "Filatmo", the FP7 ITN network "JMAP" and the SNSF starting grant "BSSGI0 155846".

Author Contributions

J.P.W., U.B., A.P. and J.K. designed the experiment; D.M., J.S., E.S. and M.M. designed and set up the experimental setup; D.M., J.S., E.S., J.G.B., N.B. and J.K. carried out the experiments; D.M., J.S. and J.K. designed and carried out the data analysis; D.M., J.S. and J.K. wrote the paper; All authors reviewed the manuscript.

Additional Information

Competing financial interests: The authors declare no competing financial interests.

How to cite this article: Mongin, D. *et al.* Non-linear photochemical pathways in laser-induced atmospheric aerosol formation. *Sci. Rep.* **5**, 14978; doi: 10.1038/srep14978 (2015).

Conductivity and Discharge Guiding Properties of Mid-Infrared Laser Filaments

B

Conductivity and Discharge Guiding Properties of Mid IR Laser Filaments

D. Mongin, E. Schubert, J. Kasparian, J.P. Wolf

GAP-Biophotonics, University of Geneva 22, ch. de Pinchat, 1211 Geneva 4, Switzerland

V. Shumakova, S. Alisauskas, A. Pugzlys, A. Baltuska

Photonics Institute, Vienna University of Technology, Guhausstrae 27/387, 1040 Vienna, Austria

November 7, 2016

Abstract

The electric properties of mid-IR filaments in air have been investigated in comparison to their more traditional near IR counterparts. Although the number of ions left after the pulse is similar for both spectral regions, filaments at 3.9 µm produce lower electron densities and lower pressure depression, which prevent them in the present conditions (25 mJ, 90 fs) to trigger or guide HV discharges (130 kV over 12 cm). We conclude that mid-IR filaments require significantly higher energy/power levels than their near IR counterparts for applications related to lightning control and for fully taking advantage of their unique propagation properties (single, large diameter filaments over long distances).

1 Introduction

Femtosecond mid infrared (2-10 µm) filaments have recently attracted much attention because of their unique properties as compared to their more traditional counterparts in the visible and near infrared spectral range. More precisely, mid-IR filaments appear insensitive to spatial break-up into multiple filaments, and are expected to produce single millimeter sized optical pillars bearing very high intensities over hundreds of meters [1–3]. The difference in the filamentation process between the near-IR and the mid-IR regimes relates, to a large extent, to the λ^2 dependence of the critical power: while $P_c \approx 3.3$ GW [4] at 800 nm and 5.3 GW [5] at 1030 nm, P_c reaches 150 GW at 3.9 µm [1]. The first experimental observation of mid-IR filaments in gases was achieved in high pressure Argon [6] using advanced optical parametric chirped pulse amplification (OPCPA) technologies at 3.9 µm [7]. Thanks to further development of this unique system, reaching now the sub-TW level, mid-IR filaments could

be produced in atmospheric air for the first time [1]. Significant work is currently carried out for developing mid-IR multi-TW sources, including scaling up OPCPAs and ultrashort laser seeded high pressure CO2 amplifiers [8–10]. The atmospheric applications of such intense and long-distance spanning single filaments are numerous, ranging from remote sensing of multiple pollutants to lightning control. For the latter application, investigating the electrical properties of these mid-IR waveguides is essential. In this letter, we present the first measurements of plasma density, electric conductivity, HV-discharge guiding properties and neutralization capability [11] of intense mid-IR filaments in air, and compare the results to near IR wavelengths, namely 800 nm and 1030 nm.

2 Experimental setup

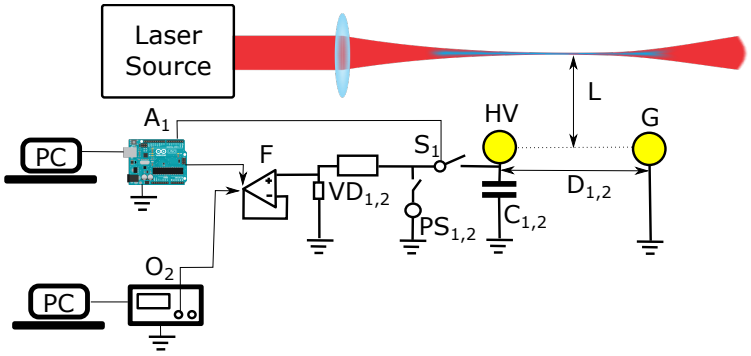

Figure 1: Experimental setup for investigation of conductivity (1) and discharge guiding (2) properties of NIR and MIR filaments. HV - high voltage electrode, G - grounded electrode, PC - computer, A_1 - Arduino acquisition and control of switch S_1, O - oscilloscope acquisition, F – follower circuit, VD_1 and VD_2 - voltage divider correspondingly 1:4000 divider of 300 GΩ impedance and 1:20000 divider of 400 GΩ impedance, PS_1 and PS_2 - correspondingly 10 kV and 130 kV power supplies, C_1 and C_2 - correspondingly 1 nF and 250 pF capacitors, D_1 and D_2 – distance between the electrodes of 16 cm and 12 cm respectively, L - lateral displacement of filament with respect to the electrodes.

Three different setups were used in the present work. The filament conductivity measurement, whose results are discussed in Section 3.2, relied on the setup 1 described in Fig.1 with subscripts 1. It is based on a 10 kV, 7 mA DC generator (PS_1) connected to spherical electrodes (diameter 1.2 cm), which could be placed arbitrarily on either side of the laser beam, at various axial and longitudinal positions. One electrode was grounded (G), while the other (HV), separated by a distance $D_1 = 16$ cm, was set to the potential of the high-voltage generator (PS_1) and attached to a 1 nF capacitor (C_1). In order to investigate the unloading of the capacitor due to the laser induced filament, the generator (PS_1) was disconnected and the voltage on the HV electrode was monitored through a voltage divider probe with a 300 GΩ impedance and a follower amplifier (TL1169). To avoid constant leakage from the capacitor

through the voltage probe, a contact between the HV electrode and the probe was periodically established by an Arduino-based device (A_1 in Fig.1).

The discharge/guiding measurements described in section 3.3 relied on the setup 2 (Fig.1 with subscripts 2). It relied on a 130 kV, 200 µA maximum current DC generator (PS_2). One electrode was connected to the potential and attached to a 250 pF capacitor (C_2), while the ground electrode was at a distance $D_2 = 12$ cm. The potential on the HV electrode was monitored through by a 1:20000 voltage divider of 400 GΩ impedance.

The setup 3 is used for the plasma density measurement, to which we will refer as capacitive probe measurement. It consists in the measurement of the positive current swing due to the flow of ionic species between two parallel flat electrodes polarized by a voltage 10 kV (Fig. 3(b)). It is important to notice that the two first setups have their electrodes along the filament propagation, whereas the capacitive probe measurement have the electrodes above and below the filament.

High peak power ultrashort mid-infrared pulses were delivered by a hybrid OPA/OPCPA system described in detail in [12]. In brief, the system consists of a femtosecond Yb:CaF_2 chirped pulse amplifier (CPA), a three-stage optical parametric amplifier (OPA), a grating/prism (GRISM) stretcher, a picosecond 20 Hz Nd:YAG pump laser, a three-stage OPCPA system, and a grating compressor for mid-infrared pulses. 200 fs pulses from the Yb:CaF_2 CPA are used to pump the white light seeded OPA based on type-II KTP crystals and operating at 1460 nm central wavelength. The generated 1460 nm signal pulses are subsequently stretched in a GRISM stretcher and used as a seed for a three-stage OPCPA system based on type II KTA crystals and pumped by 100-ps Nd:YAG laser pulses with energies of respectively, 50, 250, and 700 mJ. The 3.9 µm idler pulses are picked up in the 2nd OPCPA-stage and after amplification in the 3rd stage are compressed to 90 fs with a diffraction gratings based compressor. The energy of the compressed 3.9 µm pulses exceeds 25 mJ.

Data obtained with the high peak power ultrashort mid-infrared pulses were compared with data acquired by using two different near IR laser systems: namely a 1030 nm Yb:CaF2 CPA generating 220 fs 110 mJ pulses at 50 Hz repetition rate [7] and a Ti:Sapphire CPA operating at 800 nm central wavelength and delivering 14 mJ 60 fs pulses at a variable repetition rate from 20 Hz to 1 kHz (Coherent Legend).

The experiments with all three laser systems were performed in similar conditions, at a room temperature of 20°C and relative humidity of 30%, which corresponds to a background resistivity of air of about $3.10^{14}\Omega$.m; filamentation in all three cases was assisted by 1 m focusing while electric parameters were kept identical.

The filament side luminescence was recorded with digital photo cameras. The settings of the camera, such as f-number, exposure time and sensitivity, were set in order to avoid saturation of the CMOS-sensor. As it can be seen in Fig.2c, the spectral sensitivity of the cameras, used in the experiments, overlaps with the red side of the plasma emission spectrum .

3 Results and Discussion

3.1 Plasma density along the filament

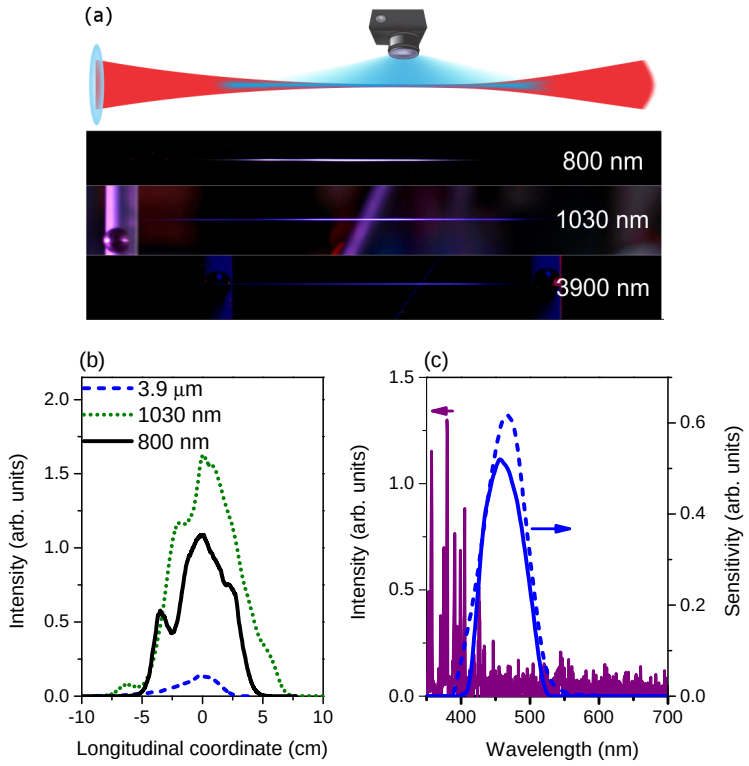

Figure 2: (a) Photographs of the filaments generated at different wavelengths (indicated in the panels) recorded by a digital photo camera; (b) relative amplitudes of extracted spatial luminescence distribution shown in (a). (c) Side-luminescence spectrum of a filament generated by the 3.9 µm driver recorded with a spectrometer and spectral sensitivity curves of the blue channels of Canon (400D) (solid line) and Nikon (70D) (dashed line) photo cameras [13].

Plasma emission was recorded at comparable peak powers for all 3 lasers: 14 mJ pulse energy, ∼0.23 TW peak power for the 800 nm Ti:Sapphire laser, 36 mJ pulse energy, ∼0.16 TW peak power for the 1030 nm Yb:CaF2 laser and 26 mJ pulse energy, ∼0.28 TW peak power for the mid IR OPCPA.

As already reported from numerical simulations for the 3.9 µm driver [1, 2] and visual observations for the 800 nm driver [14] , the visible part of the filaments represents only a fraction of the plasma channel recorded by a transverse electrical probe. Therefore, to assess the plasma density distribution along the filaments more quantitatively, we measured the positive current swing due to the flow of ionic species thanks to the setup 3 described in Fig. 3(b). The results were analysed according to [14] and [15], and provide a good estimate of

the total number of positive and negative O_2 ions generated in a filament. The use of the dipole induced by the electrons and parent ions just after ionization for the assessment of the initial electron density remains controversial [16].

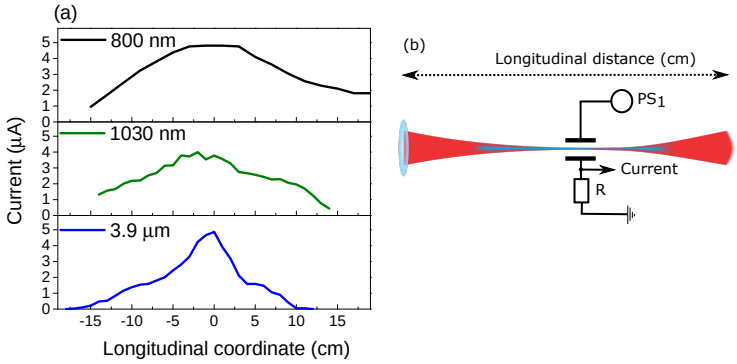

Figure 3: (a) Measured ionic current induced by the filaments at 3 different driving wavelengths (indicated in the panels); (b) schematics of the measurement

The measurements show that the maximum recorded current, and thus the maximum number of ions (positive and negative) per filament length unit (and per pulse) that reach the electrodes is similar for the three wavelengths and correspond roughly to $\sim 10^9$ elementary charges per cm. However, consistently with the plasma emission presented in Fig.2, the length of the plasma column is twice longer at 800 nm than at 3.9 µm, leading to a longer conductive path.

The diameters of the filaments also differ significantly: from 100-200 um in the NIR [4,17] to 600-800 µm FWHM at 3.9 µm, as estimated from the width of the luminescent plasma line on a side image. It is therefore reasonable to conclude that the maximum ion density is lower by more than one order of magnitude for the mid IR plasma channel as compared to the NIR. However, a direct link between the initial electron densities and ionic densities after travelling several centimeters in hundreds of microseconds is not straightforward [18–20].

Since the peak powers of the laser pulses in all three cases are comparable ($\sim 0.16 - 0.28$ TW), the number of critical powers reached in the case of mid IR pulses is significantly lower ($\sim 2-3$ P_c(3.9µm)) than for the two NIR lasers ($\sim 20 - 30$ P_c(NIR)). This might be a cause for the 3.9 µm filament being shorter as compared to near-IR filaments: the balance between self-focusing and defocusing is more critical and more sensitive to losses when the laser pulse peak power is close to the threshold of P_c. In the case when peak power of mid IR pulses exceeds P_c by more than an order of magnitude a novel regime of filament formation and propagation recently was predicted by numerical modeling [2].

A final indication of the lower gas ionization in the mid-IR is the total energy loss of the beam after filamentation, ranging from 7% at 3.9 µm to 12% at 800 nm.

3.2 Conductivity of mid-IR filaments

In a recently published work, it was shown that 800 nm filaments were able to unload charged capacitors without air breakdown [11]. This allows to determine an equivalent resistance R_{equ} of the conductive path between the HV electrode and the ground electrode, from the measured decay time constant $\tau = R_{equ}C_1$, C_1 being the capacity attached to the high-voltage electrode, that gets emptied by the current flow.

We presently investigated the equivalent conductivity of mid-IR filaments thanks to this technique using the setup 1 described in Fig. 1, and compare it to the 800 nm and 1030 nm cases at comparable peak powers. The advantage of this method is that it includes all the effects related to the filamentation process, including charge density, charge continuity and space charges, field lines distortion, acceleration by the HV field, shock waves inducing pressure gradients [17], etc.

Fig.4(a) shows the filament induced neutralization of a $C_1 = 1$ nF capacitor loaded at 10 kV, attached to a spherical electrode separated by 16 cm from the ground electrode. The filament propagated parallel to the line connecting the centers of the electrodes with the lateral distance L between the filament and electrodes being varied from 0 to 10 cm (Fig.1).

For the minimal lateral distance (filament grazing to the electrodes) the resistance of the mid-IR filament amounts to 700 GΩ over the 16 cm gap, while for the 1030 nm and 800 nm drivers it was 190 GΩ and 150 GΩ respectively. Here we should note that the repetition rate of the 1030 nm laser was 50 Hz as compared to 20 Hz in the case of 3.9 µm OPCPA system. Fig.4(a) reveals that as the lateral distance increases, the fraction of the filamenting path over the whole path decreases, and the overall equivalent resistance increases accordingly, up to the value of neutral air.

In order to take into account the difference in repetition rates, we normalized the conductance through the repetition rate ν of the laser. The resulting quantity $C = 1/(R_{equ}\nu)$, homogeneous in units of a capacity, could be interpreted as a fraction of the capacity that could be fully extracted, under the considered experimental conditions, by a single laser pulse.

As displayed in Fig. 4(b), the 800 nm laser filament is the most efficient neutralizer in this configuration, with the capacitance being C(800 nm) $\sim$ 0.2 pF, then C(1030 nm) $\sim$ 0.12 pF and C(3.9 um) $\sim$ 0.07 pF for the filaments grazing on the electrodes. The observed spectral dependence is consistent with the plasma density measurements. Although each of the three lasers can remotely discharge our capacitor without grazing the electrodes. Over lateral distances of several cm, resistance between the electrodes and the filament is mainly due to air resistivity and each three laser have the same neutralizing capability. We can thus say that 800 nm filament neutralizing capacity have a wider lateral extend than the 1030 nm and 3.9 µm ones.

Surprisingly, laser pulses at 800 nm are more efficient to neutralize the charged capacitor when the repetition rate is lower. This counter-intuitive effect will be addressed in future work.

It is interesting to notice that three filaments in our conditions can remove a capacity of the order of 0.1∼pF per shot, which corresponds to the neutralization of typically 6×10^9 carriers for the first laser shot with the initial charge in the capacitor corresponding to 6.25×10^{13} carriers. Based on the recorded currents

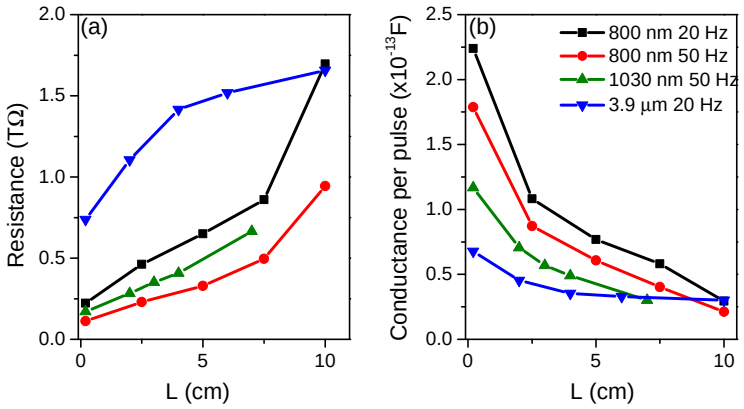

Figure 4: (a) Filament-induced capacitor unloading : Equivalent resistance R_{equ} of the path for the 800 nm, 1030 nm and 3.9 µm filaments, as a function of the lateral displacement L (see Fig.1) of the filament relative to the electrodes; (b) normalized filament conductance (see text), as a function of lateral distance L

presented in Fig. 3, we estimated the resistance of a pathway through the filament at each wavelength. We assume that the current is proportional to the number of carriers per unit length of filament, and that the resistivity is inversely proportional to this carrier density. The resistance of the filaments at each wavelength can then be compared by integrating the inverse signals shown in Fig.3 along the gap between the electrodes. This estimation yields the difference by a factor of 1.4 between the resistances of 1030 nm and 3.9 μm filaments, and by a factor of 2 between the 800 nm and 3.9 µm filament. Those ratios are consistent with the wavelength dependence of the filament conductance (Fig. 4(b)). The difference in conductance between the respective wavelengths is therefore due to the different longitudinal charge distributions over the gap between the electrodes.

3.3 Discharge triggering/guiding

Charging electrodes separated by 12 cm with 130 kV DC allows investigating a very different action of filaments (setup 2 described in Fig. 1). At such high electric field densities, corona effects around the electrodes and impact ionization by electrons are leading to avalanche ionization and heating of the plasma channel, which then become the dominant processes [18,21]. Breakdown without laser was observed when the distance between electrodes was reduced to 10 cm.

A striking difference was observed when the NIR and the MIR filaments were ignited grazing to the charged electrodes (see Fig. 5): as the 1030 nm and 800 nm filaments efficiently triggered (as evidenced by the synchronization of the discharges with the laser shots) with more than 50% efficiency and guided the HV discharges, neither triggering nor guiding was induced by the mid-IR filament.

Guiding of discharges mainly relies on the creation of a low pressure channel

Bibliography

ABDOLLAHPOUR, D., SUNTSOV, S., PAPAZOGLOU, D., & TZORTZAKIS, S. 2011, Measuring easily electron plasma densities in gases produced by ultrashort lasers and filaments. *Optics express* **19** (18), 16866–16871 [see pp. 43 and 52]

ACKERMANN, R., MÉJEAN, G., KASPARIAN, J., YU, J., SALMON, E., & WOLF, J.-P. 2006, Laser filaments generated and transmitted in highly turbulent air. *Optics Letters* **31**, 86–88 [see pp. 19 and 25]

AKTURK, S., ZHOU, B., FRANCO, M., COUAIRON, A., & MYSYROWICZ, A. 2009, Generation of long plasma channels in air by focusing ultrashort laser pulses with an axicon. *Optics Communications* **282** (1), 129–134 [see p. 43]

ALIŠAUSKAS, S., KARTASHOV, D. V., PUGŽLYS, A., VORONIN, A., ZHELTIKOV, A. M., PETRARCA, M., BÉJOT, P., KASPARIAN, J., & BALTUŠKA, A. 2012, Mid-infrared femtosecond filament and three octaves continuum generation in gases. In *Ultrafast phenomena 2012*, Lausanne, Suisse, poster [see p. 39]

ALSHERSHBY, M., REN, Y., QIN, J., HAO, Z., & LIN, J. 2013, Diagnosis of femtosecond plasma filament by channeling microwaves along the filament. *Applied Physics Letters* **102** (20), 204101 [see p. 43]

ANDRIUKAITIS, G., BALČIŪNAS, T., ALIŠAUSKAS, S., PUGŽLYS, A., BALTUŠKA, A., POPMINTCHEV, T., CHEN, M.-C., MURNANE, M. M., & KAPTEYN, H. C. 2011, 90 GW peak power few-cycle mid-infrared pulses from an optical parametric amplifier. *Optics letters* **36** (15), 2755–2757 [see p. 38]

ANDRIUKAITIS, G., KAKSIS, E., POLONYI, G., FÜLÖP, J., BALTUSKA, A., & PUGZLYS, A. 2015, 220-fs 110-mJ Yb:CaF_2 cryogenic multipass amplifier. In *CLEO: Science and Innovations*, SM1P–7, Optical Society of America [see p. 10]

APOLLONOV, V. V., VASILYAK, L. M., VERESHCHAGIN, I. P., GLAZKOV, V. V., GERASIMOV, D. N., KONONOV, I. G., ORLOV, A. V., POLYAKOV, D. N., SINKEVICH, O. A., SOKOLOVA, M. V., TEMNIKOV, A. G., & FIRSOV, K. N. 2002, Experimental simulation of a laser lightning-protection system on a device with an artificial cloud of charged aqueous aerosol. *Quantum Electronics* **32** (6), 523 [see p. 64]

BALL, L. M. 1974, The laser lightning rod system: thunderstorm domestication. *Applied Optics* **13** (10), 2292–2296 [see p. 63]

BATCHELOR, G. K. 1982, *The Theory of Homogeneous Turbulence*. Cambridge University Press, Cambridge [see p. 20]

BAZELYAN, E. M. & RAIZER, Y. P. 2000a, *Lightning physics and lightning protection*. CRC Press [see p. 63]

BAZELYAN, E. M. & RAIZER, Y. P. 2000b, The mechanism of lightning attraction and the problem of lightning initiation by lasers. *Physics - Uspekhi* **43**, 701 [see p. 64]

BÉJOT, P., BONACINA, L., EXTERMANN, J., MORET, M., WOLF, J.-P., ACKERMANN, R., LASCOUX, N., SALAMÉ, R., SALMON, E., KASPARIAN, J., BERGÉ, L., CHAMPEAUX, S., GUET, C., BLANCHOT, N., BONVILLE, O., BOSCHERON, A., CANAL, P., CASTALDI, M., HARTMANN, O., LEPAGE, C., MARMANDE, L., MAZATAUD, E., MENNERAT, G., PATISSOU, L., PREVOT, V., RAFFESTIN, D., & RIBOLZI, J. 2007, 32 terawatt atmospheric white-light laser. *Applied Physics Letters* **90**, 151106–151106 [see pp. 12 and 14]

BÉJOT, P., HERTZ, E., KASPARIAN, J., LAVOREL, B., WOLF, J.-P., & FAUCHER, O. 2011, Transition from plasma-driven to Kerr-driven laser filamentation. *Physical Review Letters* **106** (24), 243902 [see p. 61]

BELKHELFA, Y. 2008, *Etude du comportement dynamique et du transfert de matière et de chaleur entre des particules sphériques et un écoulement laminaire ou turbulent*. Ph.D. thesis, Institut national des sciences appliquées de Rouen [see p. 30]

BENDERSKY, S., KOMEIKA, N. S., & BLAUNSTEIN, N. 2004, Atmospheric optical turbulence over land in middle east coastal environments: prediction modeling and measurements. *Applied Optics* **43** (20), 4070–4079 [see p. 21]

BERGÉ, L., GOUÉDARD, C., SCHJODT-ERIKSEN, J., & WARD, H. 2003, Filamentation patterns in Kerr media vs. beam shape robustness, nonlinear saturation and polarization states. *Physica D: Nonlinear Phenomena* **176** (3-4), 181–211 [see p. 12]

BERGÉ, L., SCHMIDT, M. R., RASMUSSEN, J. J., CHRISTIANSEN, P. L., & RASMUSSEN, K. Ø. 1997, Amalgamation of interacting light beamlets in Kerr-type media. *J. Opt. Soc. Am. B* **14** (10), 2550–2562 [see pp. 12 and 16]

BERGÉ, L., SKUPIN, S., NUTER, R., KASPARIAN, J., & WOLF, J.-P. 2007, Ultrashort filaments of light in weakly ionized, optically transparent media. *Reports on progress in physics* **70** (10), 1633 [see pp. 5, 33, 54, 61, 67, and 73]

BERLIEN, H.-P., BREUER, H., MÜLLER, G. J., KRASNER, N., OKUNATA, T., & SLINEY, D. 2012, *Applied laser medicine*. Springer Science & Business Media [see p. 1]

BERNHARDT, J., LIU, W., THÉBERGE, F., XU, H., DAIGLE, J., CHÂTEAUNEUF, M., DUBOIS, J., & CHIN, S. L. 2008, Spectroscopic analysis of femtosecond laser plasma filament in air. *Optics Communications* **281** (5), 1268–1274 [see p. 43]

BODROV, S., BUKIN, V., TSAREV, M., MURZANEV, A., GARNOV, S., ALEKSANDROV, N., & STEPANOV, A. 2011, Plasma filament investigation by transverse optical interferometry and terahertz scattering. *Optics express* **19** (7), 6829–6835 [see p. 43]

BOHREN, C. F. & HUFFMAN, D. R. 1983, *Absorption and Scattering of Light by Small Particles*. Wiley [see pp. 26, 27, and 28]

BOYD, R. W. 2008, *Nonlinear Optics*. 3rd edn., Academic Press, Boston [see p. 5]

BRAUN, A., KORN, G., LIU, X., DU, D., SQUIER, J., & MOUROU, G. 1995, Self-channeling of high-peak-power femtosecond laser pulses in air. *Optics Letters* **20** (1), 73–75 [see pp. 2 and 5]

BURCH, D. S., SMITH, S. J., & BRANSCOMB, L. M. 1958, Photodetachment of O_2^-. *Physical Review* **112** (1), 171–175 [see pp. 53 and 58]

CARTWRIGHT, D., CHUTJIAN, A., TRAJMAR, S., & WILLIAMS, W. 1977, Electron impact excitation of the electronic states of N_2. I. differential cross sections at incident energies from 10 to 50 eV. *Physical Review A* **16** (3), 1013 [see p. 58]

CENTURION, M., PU, Y., LIU, Z., PSALTIS, D., & HÄNSCH, T. W. 2004, Holographic recording of laser-induced plasma. *Optics letters* **29** (7), 772–774 [see p. 43]

CHENG, Y.-H., WAHLSTRAND, J. K., JHAJJ, N., & MILCHBERG, H. 2013, The effect of long timescale gas dynamics on femtosecond filamentation. *Optics express* **21** (4), 4740–4751 [see pp. 9, 20, and 22]

CHIAO, R. Y., GARMIRE, E., & TOWNES, C. H. 1964, Self-trapping of optical beams. *Physical Review Letters* **13** (15), 479–482 [see p. 5]

CHICHKOV, B. N., MOMMA, C., NOLTE, S., VON ALVENSLEBEN, F., & TÜNNERMANN, A. 1996, Femtosecond, picosecond and nanosecond laser ablation of solids. *Applied Physics A* **63** (2), 109–115 [see p. 53]

CHIN, S. L., HOSSEINI, S. A., LIU, W., LUO, Q., THÉBERGE, F., AKÖZBEK, N., BECKER, A., KANDIDOV, V. P., KOSAREVA, O. G., & SCHRÖDER, H. 2005, The propagation of powerful femtosecond laser pulses in optical media: physics, applications, and new challenges. *Canadian Journal of Physics* **83**, 863–905 [see p. 61]

CHIN, S. L., PETIT, S., LIU, W., IWASAKI, A., NADEAU, M. C., KANDIDOV, V. P., KOSAREVA, O. G., & ANDRIANOV, K. Y. 2002, Interference of transverse rings in multifilamentation of powerful femtosecond laser pulses in air. *Optics Communications* **210** (3-6), 329–341, 10.1016/S0030-4018(02)01808-4 [see p. 14]

CHIN, S. L., WANG, T.-J., MARCEAU, C., WU, J., LIU, J., KOSAREVA, O., PANOV, N., CHEN, Y., DAIGLE, J.-F., YUAN, S., *et al.* 2012, Advances in intense femtosecond laser filamentation in air. *Laser Physics* **22** (1), 1–53 [see p. 5]

CHIWA, M., KONDO, H., EBIHARA, N., & SAKUGAWA, H. 2008, Atmospheric concentrations of nitric acid, sulfur dioxide, particulate nitrate and particulate sulfate, and estimation of their dry deposition on the urban-and mountain-facing sides of Mt. Gokurakuji, Western Japan. *Environmental monitoring and assessment* **140** (1-3), 349–360 [see p. 35]

CHRYSSOLOURIS, E. 2013, *Laser machining: theory and practice*. Springer Science & Business Media [see p. 1]

COMTOIS, D., CHIEN, C. Y., DESPAROIS, A., GÉRIN, F., JARRY, G., JOHNSTON, T. W., KIEFFER, J. C., FONTAINE, B. L., MARTIN, F., MAWASSI, R., PÉPIN, H., RIZK, F. A. M., VIDAL, F., COUTURE, P., MERCURE, H. P., POTVIN, C., BONDIOU-CLERGERIE, A., & GALLIMBERTI, I. 2000, Triggering and guiding leader discharges using a plasma channel created by an ultrashort laser. *Applied physics Letters* **76** (7), 819–821 [see p. 64]

COUAIRON, A. & MYSYROWICZ, A. 2007, Femtosecond filamentation in transparent media. *Physics reports* **441** (2), 47–189 [see pp. 5, 6, 7, 10, 11, 33, 61, 67, and 73]

COURVOISIER, F., BOUTOU, V., KASPARIAN, J., SALMON, E., MÉJEAN, G., YU, J., & WOLF, J.-P. 2003, Ultraintense light filaments transmitted through clouds. *Applied Physics Letters* **83**, 213–215 [see pp. 8 and 26]

DE LA CRUZ, L., SCHUBERT, E., MONGIN, D., KLINGEBIEL, S., SCHULTZE, M., METZGER, T., MICHEL, K., KASPARIAN, J., & WOLF, J.-P. 2016, High repetition rate ultrashort laser cuts a path through fog. *Applied Physics Letters* **109** (25), 251105 [see p. 19]

CURRAN, E. B., HOLLE, R. L., & LÓPEZ, R. E. 2000, Lightning casualties and damages in the United States from 1959 to 1994. *Journal of Climate* **13** (19), 3448–3464 [see p. 63]

D'ASARO, E., HEIDARI-BATENI, S., PASQUAZI, A., ASSANTO, G., GONZALO, J., SOLIS, J., & AFONSO, C. N. 2009, Interaction of self-trapped beams in high index glass. *Optics Express* **17** (19), 17150–17155 [see p. 12]

DECUSATIS, C. 2013, *Handbook of fiber optic data communication: a practical guide to optical networking*. Academic Press [see p. 1]

DEMTRÖDER, W. 2013, *Laser spectroscopy: basic concepts and instrumentation*. Springer Science & Business Media [see p. 1]

DERGACHEV, A. A., IONIN, A. A., KANDIDOV, V. P., SELEZNEV, L. V., SINITSYN, D. V., SUNCHUGASHEVA, E. S., & SHLENOV, S. A. 2013, Filamentation of IR and UV femtosecond pulses upon focusing in air. *Quantum Electronics* **43** (1), 29 [see p. 11]

DIELS, J.-C. & ZHAO, X. M. 1992, Discharge of lightning with ultrashort laser pulses. US Patent 5175664 [see pp. 3, 53, and 79]

DRISCOLL, T. A., HALE, N., & TREFETHEN, L. N. 2014, *Chebfun Guide*. Pafnuty Publications [see p. 16]

DURAND, M., HOUARD, A., PRADE, B., MYSYROWICZ, A., DURÉCU, A., MOREAU, B., FLEURY, D., VASSEUR, O., BORCHERT, H., DIENER, K., SCHMITT, R., THÉBERGE, F., CHATEAUNEUF, M., DAIGLE, C., JEAN-FRAN & DUBOIS, J. 2013, Kilometer range filamentation. *Optics Express* **21** (22), 26836–26845 [see pp. 2, 8, and 64]

EISENMANN, S., PENANO, J., SPRANGLE, P., & ZIGLER, A. 2008, Effect of an energy reservoir on the atmospheric propagation of laser-plasma filaments. *Physical Review Letters* **100** (15), 155003–4 [see p. 8]

ETO, S., ZHIDKOV, A., OISHI, Y., MIKI, M., & FUJII, T. 2012, Quenching electron runaway in positive high-voltage-impulse discharges in air by laser filaments. *Optics letters* **37** (6), 1130–1132 [see p. 64]

ETTOUMI, W., KASPARIAN, J., & WOLF, J.-P. 2015a, Laser filamentation as a new phase transition universality class. *Physical Review Letters* **114** (6), 063903 [see pp. 11 and 12]

ETTOUMI, W., KASPARIAN, J., & WOLF, J.-P. 2015b, Spin-glass model governs laser multiple filamentation. *Physical Review Letters* **115** (3), 033902 [see pp. 11, 12, and 49]

FACCIO, D., LOTTI, A., MATIJOSIUS, A., BRAGHERI, F., DEGIORGIO, V., COUAIRON, A., & TRAPANI, P. D. 2009, Experimental energy-density flux characterization of ultrashort laser pulse filaments. *Optics Express* **17** (10), 8193–8200 [see p. 18]

FACCIO, D., PORRAS, M. A., DUBIETIS, A., BRAGHERI, F., COUAIRON, A., & DI TRAPANI, P. 2006, Conical emission, pulse splitting, and X-wave parametric amplification in nonlinear dynamics of ultrashort light pulses. *Physical Review Letters* **96** (19), 193901 [see p. 18]

FEIT, M. & FLECK JR, J. 1974, Effect of refraction on spot-size dependence of laser-induced breakdown. *Applied Physics Letters* **24** (4), 169–172 [see p. 7]

FENG, C. 2016, *Sub-nanosecond UV filaments and their applications for remote spectroscopy and high-voltage discharges*. Ph.D. thesis, University of New Mexico [see pp. 79 and 82]

FERNSLER, R. F., ALI, A. W., GREIG, J. R., & VITKOVITSKY, I. M. 1979, The NRL CHMAIR code: a disturbed sea level air chemistry code. Tech. rep., DTIC Document [see pp. 55, 56, and 58]

GARY, C. 2004, *La foudre. Nature, histoire, risques et protection*. Dunod, Paris [see pp. 1, 63, 65, and 66]

GEINTS, Y. & ZEMLYANOV, A. 2014, Single and multiple filamentation of multi-terawatt CO_2-laser pulses in air: numerical simulations. *JOSA B* **31** (4), 788–797 [see pp. 2 and 10]

GEINTS, Y. E., ZEMLYANOV, A. A., IONIN, A. A., MOKROUSOVA, D. V., SELEZNEV, L. V., SINITSYN, D. V., & SUNCHUGASHEVA, E. S. 2015, Comparative analysis of post-focal filamentation of focused UV and IR laser pulses in air. *Quantum Electronics* **45** (4), 321 [see p. 11]

GORDON, D., TING, A., HUBBARD, R., BRISCOE, E., MANKA, C., SLINKER, S., BARONAVSKI, A., LADOUCEUR, H., GROUNDS, P., & GIRARDI, P. 2003, Streamerless guided electric discharges triggered by femtosecond laser filaments. *Physics of Plasmas (1994-present)* **10** (11), 4530–4538 [see p. 64]

HABERBERGER, D., TOCHITSKY, S., & JOSHI, C. 2010, Fifteen terawatt picosecond CO_2 laser system. *Optics express* **18** (17), 17865–17875 [see p. 10]

HENIN, S. 2013, *Laser Filament-induced Aerosol Generation in the Atmosphere*. Ph.D. thesis, Université de Genève [see pp. 5, 8, 34, and 37]

HENIN, S., PETIT, Y., KASPARIAN, J., WOLF, J.-P., JOCHMANN, A., KRAFT, S. D., BOCK, S., SCHRAMM, U., SAUERBREY, R., NAKAEMA, W. M., STELMASZCZYK, K., ROHWETTER, P., WÖSTE, L., SOULEZ, C.-L., MAUGER, S., BERGÉ, L., & SKUPIN, S. 2010, Saturation of the filament density of ultrashort intense laser pulses in air. *Applied Physics B* **100**, 77 [see pp. 12, 13, 14, and 15]

HENIN, S., PETIT, Y., KISELEV, D., KASPARIAN, J., & WOLF, J.-P. 2009, Contribution of water droplets to charge release by laser filaments in air. *Applied Physics Letters* **95**, 091107, poster, S. Henin [see p. 43]

HENIN, S., PETIT, Y., ROHWETTER, P., STELMASZCZYK, K., HAO, Z., NAKAEMA, W., VOGEL, A., POHL, T., SCHNEIDER, F., KASPARIAN, J., *et al.* 2011, Field measurements suggest the mechanism of laser-assisted water condensation. *Nature communications* **2**, 456 [see pp. 2, 33, 41, and 42]

HERCHER, M. 1964, Laser-induced damage in transparent media **54** (4), 563 [see p. 5]

HOSSEINI, S. A., LUO, Q., FERLAND, B., LIU, W., AKÖSBEK, N., ROY, G., & CHIN, S. L. 2003, Effective length of filaments measurement using backscattered fluorescence from nitrogen molecules. *Applied Physics B* **77**, 697–702 [see pp. 9 and 43]

HOSSEINI, S. A., LUO, Q., FERLAND, B., LIU, W., CHIN, S. L., KOSAREVA, O. G., PANOV, N. A., AKÖZBEK, N., & KANDIDOV, V. P. 2004a, Competition of multiple filaments during the propagation of intense femtosecond laser pulses. *Physical Review A* **70**, 033802–033802 [see p. 12]

HOSSEINI, S. A., YU, J., LUO, Q., & CHIN, S. L. 2004b, Multi-parameter characterization of the longitudinal plasma profile of a filament: a comparative study. *Applied Physics B* **79**, 519–523 [see p. 43]

HOUARD, A., JUKNA, V., POINT, G., ANDRÉ, Y.-B., KLINGEBIEL, S., SCHULTZE, M., MICHEL, K., METZGER, T., & MYSYROWICZ, A. 2016, Study of filamentation with a high power high repetition rate ps laser at 1.03 μm. *Optics Express* **24** (7), 7437 [see pp. 10, 11, 22, 23, 30, and 43]

IHADDADENE, M. A. & CELESTIN, S. 2015, Increase of the electric field in head-on collisions between negative and positive streamers. *Geophysical Research Letters* **42** (13), 5644–5651 [see p. 55]

IONIN, A. A., KUDRYASHOV, S. I., LEVCHENKO, A. O., SELEZNEV, L. V., SHUTOV, A. V., SINITSYN, D. V., SMETANIN, I. V., USTINOVSKY, N. N., & ZVORYKIN, V. D. 2012, Triggering and guiding electric discharge by a train of ultraviolet picosecond pulses combined with a long ultraviolet pulse. *Applied Physics Letters* **100** (10), 104105–104105–3 [see p. 64]

IONIN, A. A., KUDRYASHOV, S. I., MOKROUSOVA, D. V., SELEZNEV, L. V., SINITSYN, D. V., & SUNCHUGASHEVA, E. S. 2014, Plasma channels under filamentation of infrared and ultraviolet double femtosecond laser pulses. *Laser Physics Letters* **11** (1), 016002 [see p. 43]

JASAPARA, J., NAMPOOTHIRI, A. V. V., RUDOLPH, W., RISTAU, D., & STARKE, K. 2001, Femtosecond laser pulse induced breakdown in dielectric thin films. *Physical Review B* **63** (4), 045117 [see p. 53]

Jhajj, N., Larkin, I., Rosenthal, E., Zahedpour, S., Wahlstrand, J., & Milchberg, H. 2016, Spatiotemporal optical vortices. *Physical Review X* **6** (3), 031037 [see pp. 12, 16, and 18]

Jhajj, N., Rosenthal, E., Birnbaum, R., Wahlstrand, J., & Milchberg, H. 2014, Demonstration of long-lived high-power optical waveguides in air. *Physical Review X* **4** (1), 011027 [see pp. 9, 20, 26, 29, and 30]

Joly, P., Petrarca, M., Vogel, A., Pohl, T., Nagy, T., Jusforgues, Q., Simon, P., Kasparian, J., Weber, K., & Wolf, J.-P. 2013, Laser-induced condensation by ultrashort laser pulses at 248 nm. *Applied Physics Letters* **102** (9), 091112–091112 [see pp. 11, 41, and 42]

Ju, J., Leisner, T., Sun, H., Sridharan, A., Wang, T.-J., Wang, J., Wang, C., Liu, J., Li, R., Xu, Z., & Chin, S. L. 2014, Laser-induced supersaturation and snow formation in a sub-saturated cloud chamber. *Applied Physics B* **117** (4), 1001–1007 [see p. 33]

Ju, J., Liu, J., Wang, C., Sun, H., Wang, W., Ge, X., Li, C., Chin, S. L., Li, R., & Xu, Z. 2012, Laser-filamentation-induced condensation and snow formation in a cloud chamber. *Optics Letters* **37** (7), 1214–1216 [see pp. 2 and 42]

Kartashov, D., Ališauskas, S., Pugžlys, A., Voronin, A., Zheltikov, A., Petrarca, M., Béjot, P., Kasparian, J., Wolf, J.-P., & Baltuška, A. 2012, White light generation over three octaves by femtosecond filament at 3.9 μm in argon. *Optics letters* **37** (16), 3456–3458 [see p. 10]

Kasparian, J., Rohwetter, P., Wöste, L., & Wolf, J.-P. 2012, Laser-assisted water condensation in the atmosphere: a step towards modulating precipitation? *Journal of Physics D: Applied Physics* **45** (29), 293001 [see p. 33]

Kasparian, J., Sauerbrey, R., & Chin, S. L. 2000, The critical laser intensity of self-guided light filaments in air. *Applied Physics B* **71** (6), 877–879 [see pp. 8, 51, and 54]

Kasparian, J. & Wolf, J.-P. 2008, Physics and applications of atmospheric nonlinear optics and filamentation. *Optics Express* **16**, 466–493 [see p. 5]

Keldysh, L. 1965, Ionization in the field of a strong electromagnetic wave. *Soviet Physics JETP* **20**, 1307–1314 [see p. 7]

Kheifets, S., Simha, A., Melin, K., Li, T., & Raizen, M. G. 2014, Observation of brownian motion in liquids at short times: instantaneous velocity and memory loss. *science* **343** (6178), 1493–1496 [see p. 41]

Klingebiel, S., Schultze, M., Teisset, C., Bessing, R., Haefner, M., Prinz, S., Gorjan, M., Sutter, D., Michel, K., Barros, H., Major, Z., Krausz, F., & Metzger, T. 2015, 220 mJ ultrafast thin-disk regenerative amplifier. In *CLEO: 2015, OSA Technical Digest (online)*, Paper STu4O.2, Optical Society of America, 2015 [see p. 21]

Kolesik, M. & Moloney, J. V. 2004, Self-healing femtosecond light filaments. *Optics Letters* **29** (6), 590–592 [see pp. 8 and 26]

KOLESIK, M., WRIGHT, E. M., & MOLONEY, J. V. 2004, Dynamic nonlinear X-waves for femtosecond pulse propagation in water. *Physical Review Letters* **92** (25), 253901–253901 [see p. 18]

KOLMOGOROV, A. N. 1941a, Dissipation of energy in locally isotropic turbulence. In *Dokl. Akad. Nauk SSSR*, vol. 32, 16–18, JSTOR [see p. 20]

KOLMOGOROV, A. N. 1941b, The local structure of turbulence in incompressible viscous fluid for very large Reynolds numbers. In *Dokl. Akad. Nauk SSSR*, vol. 30, 301–305, JSTOR [see p. 20]

KOOPMAN, D. W. & WILKERSON, T. 1971, Channeling of an ionizing electrical streamer by a laser beam. *Journal of Applied Physics* **42** (5), 1883–1886 [see pp. 2, 63, and 64]

KOSTERLITZ, J. M. & THOULESS, D. J. 1973, Ordering, metastability and phase transitions in two-dimensional systems. *Journal of Physics C: Solid State Physics* **6** (7), 1181 [see p. 12]

KULMALA, M., LAAKSO, L., LEHTINEN, K., RIIPINEN, I., MASO, M. D., ANTTILA, T., KERMINEN, V.-M., HORRAK, U., VANA, M., & TAMMET, H. 2004, Initial steps of aerosol growth. *Atmospheric Chemistry and Physics* **4** (11/12), 2553–2560 [see p. 37]

KWOK, H. S., ROSSI, T. M., LAU, W. S., & SHAW, D. T. 1988, Enhanced transmission in $C0_2$-laser-aerosol interactions. *Optics Letters* **13**, 192–195 [see pp. 19 and 26]

LA FONTAINE, B., COMTOIS, D., CHIEN, C. Y., DESPAROIS, A., GÉRIN, F., JARRY, G., JOHNSTON, T. W., KIEFFER, J. C., MARTIN, F., MAWASSI, R., PÉPIN, H., RIZK, F. A. M., VIDAL, F., POTVIN, C., COUTURE, P., & MERCURE, H. P. 2000, Guiding large-scale spark discharges with ultrashort pulse laser filaments. *Journal of Applied Physics* **88** (2), 610–615 [see pp. 2, 64, and 84]

LA FONTAINE, B., VIDAL, F., JIANG, Z., CHIEN, C., COMTOIS, D., DESPAROIS, A., JOHNSTON, T., KIEFFER, J.-C., PÉPIN, H., & MERCURE, H. 1999, Filamentation of ultrashort pulse laser beams resulting from their propagation over long distances in air. *Physics of Plasmas (1994-present)* **6** (5), 1615–1621 [see pp. 8, 33, and 43]

LADOUCEUR, H., BARONAVSKI, A., LOHRMANN, D., GROUNDS, P., & GIRARDI, P. 2001, Electrical conductivity of a femtosecond laser generated plasma channel in air. *Optics communications* **189** (1), 107–111 [see pp. 43 and 69]

LAHAV, O., LEVI, L., ORR, I., NEMIROVSKY, R. A., NEMIROVSKY, J., KAMINER, I., SEGEV, M., & COHEN, O. 2014, Long-lived waveguides and sound-wave generation by laser filamentation. *Physical Review A* **90** (2), 021801 [see pp. 9, 20, 22, 26, and 30]

LANGMUIR, I. 1947, Growth of particles in smokes and clouds and the production of snow from supercooled clouds. *Scienc* **106**, 505 [see p. 1]

LASSONDE, P., THIRÉ, N., ARISSIAN, L., ERNOTTE, G., POITRAS, F., OZAKI, T., LARAMEÉ, A., BOIVIN, M., IBRAHIM, H., LÉGARÉ, F., *et al.* 2015, High gain frequency domain optical parametric amplification. *IEEE Journal of Selected Topics in Quantum Electronics* **21** (5), 1–10 [see p. 10]

Leisner, T., Duft, D., Möhler, O., Saathoff, H., Schnaiter, M., Henin, S., Stelmaszczyk, K., Petrarca, M., Delagrange, R., Hao, Z., *et al.* 2013, Laser-induced plasma cloud interaction and ice multiplication under cirrus cloud conditions. *Proceedings of the National Academy of Sciences* **110** (25), 10106–10110 [see p. 33]

Liu, W., Théberge, F., Arévalo, E., Gravel, J.-F., Becker, A., & Chin, S. L. 2005, Experiment and simulations on the energy reservoir effect in femtosecond light filaments. *Optics Letters* **30** (19), 2602–2604 [see pp. 8 and 26]

Liu, X., Lu, X., Liu, X., Xi, T., Liu, F., Ma, J., & Zhang, J. 2010, Tightly focused femtosecond laser pulse in air: from filamentation to breakdown. *Optics Express* **18** (25), 26007–26017 [see p. 43]

Loeb, L. B. 1936, The problem of the mechanism of static spark discharge. *Reviews of Modern Physics* **8** (3), 267 [see p. 65]

Lu, X., Chen, S.-Y., Ma, J.-L., Hou, L., Liao, G.-Q., Wang, J.-G., Han, Y.-J., Liu, X.-L., Teng, H., Han, H.-N., *et al.* 2015, Quasi-steady-state air plasma channel produced by a femtosecond laser pulse sequence. *Scientific reports* **5** [see pp. 43 and 53]

Ma, Y. Y., Lu, X., Xi, T. T., Gong, Q. H., & Zhang, J. 2008, Filamentation of interacting femtosecond laser pulses in air. *Applied Physics B: Lasers and Optics* **93** (2), 463–468, 10.1007/s00340-008-3236-7 [see p. 12]

Maiman, T. H. 1960, Stimulated optical radiation in ruby. *Nature* **187** (4736), 493–494 [see p. 1]

Marburger, J. 1975, Self-focusing: theory. *Progress in Quantum Electronics* **4**, 35–110 [see p. 7]

Marburger, J. H. & Dawes, E. L. 1968, Dynamical formation of a small-scale filament. *Physical Review Letters* **21** (8), 556–558 [see p. 5]

Marro, J. & Dickman, R. 2005, *Nonequilibrium phase transitions in lattice models*. Cambridge University Press [see p. 12]

Matthews, M., Henin, S., Pomel, F., Théberge, F., Lassonde, P., Daigle, J.-F., Kieffer, J.-C., Kasparian, J., & Wolf, J.-P. 2013, Cooperative effect of ultraviolet and near-infrared beams in laser-induced condensation. *Applied Physics Letters* **103** (26), 264103 [see p. 11]

Measures, R. M. 1984, *Laser remote sensing - Fundamentals and applications*. Wiley Interscience [see pp. 9 and 43]

Méchain, G., D'Amico, C., André, Y.-B., Tzortzakis, S., Franco, M., Prade, B., Mysyrowicz, A., Couairon, A., Salmon, E., & Sauerbrey, R. 2005, Range of plasma filaments created in air by a multi-terawatt femtosecond laser. *Optics Communications* **247**, 171–180 [see pp. 12 and 14]

Meek, J. 1940, A theory of spark discharge. *Physical Review* **57** (8), 722 [see p. 65]

MÉJEAN, G., ACKERMANN, R., KASPARIAN, J., SALMON, E., YU, J., WOLF, J.-P., RETHMEIER, K., KALKNER, W., ROHWETTER, P., STELMASZCZYK, K., *et al.* 2006, Improved laser triggering and guiding of megavolt discharges with dual fs-ns pulses. *Applied physics letters* **88** (2), 021101 [see pp. 53, 77, 79, and 82]

MÉJEAN, G., KASPARIAN, J., YU, J., SALMON, E., FREY, S., WOLF, J.-P., SKUPIN, S., VINÇOTTE, A., NUTER, R., CHAMPEAUX, S., *et al.* 2005, Multifilamentation transmission through fog. *Physical review E* **72** (2), 026611 [see pp. 12, 14, and 19]

MEYZONNETTE, J. & LÉPINE, T. 2001, *Bases de radiométrie optique, 2ème édition*. Cépaduès-Éditions [see p. 25]

MIKI, M., AIHARA, Y., & SHINDO, T. 1993, Development of long gap discharges guided by a pulsed CO_2 laser. *Journal of physics D : Applied physics* **26**, 1244–1252 [see pp. 2 and 64]

MIKI, M. & WADA, A. 1996, Guiding of electrical discharges under atmospheric air by ultraviolet laser-produced plasma channel. *Journal of applied physics* **80** (6), 3208–3214 [see p. 79]

MILLS, M. S., KOLESIK, M., & CHRISTODOULIDES, D. N. 2013, Dressed optical filaments. *Optics Letters* **38** (1), 25–27 [see p. 8]

MINARDI, S., GOPAL, A., COUAIRON, A., TAMOAŠUSKAS, G., PISKARSKAS, R., DUBIETIS, A., & DI TRAPANI, P. 2009, Accurate retrieval of pulse-splitting dynamics of a femtosecond filament in water by time-resolved shadowgraphy. *Optics Letters* **34** (19), 3020–3022 [see p. 43]

MITROFANOV, A., VORONIN, A., MITRYUKOVSKIY, S., SIDOROV-BIRYUKOV, D., PUGŽLYS, A., ANDRIUKAITIS, G., FLÖRY, T., STEPANOV, E., FEDOTOV, A., BALTUŠKA, A., *et al.* 2015, Mid-infrared-to-mid-ultraviolet supercontinuum enhanced by third-to-fifteenth odd harmonics. *Optics letters* **40** (9), 2068–2071 [see pp. 2, 10, 11, and 38]

MONGIN, D., SCHUBERT, E., BERTI, N., KASPARIAN, J., & WOLF, J.-P. 2016a, Gas-solid phase transition in laser multiple filamentation. *Submitted to PRL* [see p. 49]

MONGIN, D., SHUMAKOVA, V., ALIŠAUSKAS, S., SCHUBERT, E., PUGŽLYS, A., KASPARIAN, J., WOLF, J.-P., & BALTUŠKA, A. 2016b, Conductivity and discharge guiding properties of mid-IR laser filaments. *Applied Physics B* **122** (10), 267 [see pp. 11, 22, 41, 42, 43, and 74]

MONGIN, D., SLOWIK, J. G., SCHUBERT, E., BRISSET, J.-G., BERTI, N., MORET, M., PRÉVÔT, A. S., BALTENSPERGER, U., KASPARIAN, J., & WOLF, J.-P. 2015, Non-linear photochemical pathways in laser-induced atmospheric aerosol formation. *Scientific reports* **5** [see pp. 33 and 41]

PANAGIOTOPOULOS, P., WHALEN, P., KOLESIK, M., & MOLONEY, J. V. 2015, Super high power mid-infrared femtosecond light bullet. *Nature Photonics* **9** (8), 543–548 [see pp. 2, 10, 42, and 43]

PAPEER, J., BOTTON, M., GORDON, D., SPRANGLE, P., ZIGLER, A., & HENIS, Z. 2014, Extended lifetime of high density plasma filament generated by a dual femtosecond–nanosecond laser pulse in air. *New Journal of Physics* **16** (12), 123046 [see pp. 53, 56, 57, 58, and 60]

PAPEER, J., GORDON, D., SPRANGLE, P., BOTTON, M., & ZIGLER, A. 2013, Temporal evolution of femtosecond laser induced plasma filament in air and N_2. *Applied Physics Letters* **103** (24), 244102 [see p. 43]

PAWAR, S. D., MURUGAVEL, P., & LAL, D. M. 2009, Effect of relative humidity and sea level pressure on electrical conductivity of air over Indian Ocean. *Journal of Geophysical Research: Atmospheres* **114** (D2), D02205 [see p. 67]

PÉPIN, H., COMTOIS, D., VIDAL, F., CHIEN, C. Y., DESPAROIS, A., JOHNSTON, T. W., KIEFFER, J. C., FONTAINE, B. L., MARTIN, F., RIZK, F. A. M., POTVIN, C., COUTURE, P., MERCURE, H. P., BONDIOU-CLERGERIE, A., LALANDE, P., & GALLIMBERTI, I. 2001, Triggering and guiding high-voltage large-scale leader discharges with sub-joule ultrashort laser pulses. *Physics of plasmas* **8** (5), 2532–2539 [see p. 65]

PERELOMOV, A., POPOV, V., & TERENT'EV, M. 1966, Ionization of atoms in an alternating electric field. *Sov. Phys. JETP* **23** (5), 924–934 [see pp. 7, 55, and 58]

PETIT, Y., HENIN, S., KASPARIAN, J., & WOLF, J.-P. 2010, Production of ozone and nitrogen oxides by laser filamentation. *Applied Physics Letters* **97** (2), 021108–021108 [see pp. 33 and 34]

PETIT, Y., HENIN, S., KASPARIAN, J., WOLF, J.-P., ROHWETTER, P., STELMASZCZYK, K., HAO, Z., NAKAEMA, W., WOSTE, L., VOGEL, A., *et al.* 2011a, Influence of pulse duration, energy, and focusing on laser-assisted water condensation. *Applied Physics Letters* **98** (4), 041105–041105 [see p. 2]

PETIT, Y., HENIN, S., NAKAEMA, W. M., BÉJOT, P., JOCHMANN, A., KRAFT, S. D., BOCK, S., SCHRAMM, U., STELMASZCZYK, K., ROHWETTER, P., KASPARIAN, J., SAUERBREY, R., WÖSTE, L., & WOLF, J. 2011b, 1-J white-light continuum from 100-TW laser pulses. *Physical Review A* **83** (1), 013805 [see pp. 12 and 49]

PETRARCA, M., HENIN, S., STELMASZCZYK, K., BOCK, S., KRAFT, S., SCHRAMM, U., VANEPH, C., VOGEL, A., KASPARIAN, J., SAUERBREY, R., WEBER, K., WÖSTE, L., & WOLF, J.-P. 2011, Multijoule scaling of laser-induced condensation in air. *Applied Physics Letters* **99** (14), 141103–141103–3 [see pp. 12, 41, and 42]

POINT, G., THOUIN, E., MYSYROWICZ, A., & HOUARD, A. 2016, Energy deposition from focused terawatt laser pulses in air undergoing multifilamentation. *Optics express* **24** (6), 6271–6282 [see p. 61]

POLYANSKIY, M. N., BABZIEN, M., & POGORELSKY, I. V. 2015, Chirped-pulse amplification in a CO_2 laser. *Optica* **2** (8), 675–681 [see p. 10]

POLYNKIN, P. 2012, Mobilities of O_2^+ and O_2^- ions in femtosecond laser filaments in air. *Applied Physics Letters* **101** (16), 164102 [see pp. 43, 46, and 52]

POLYNKIN, P. & MOLONEY, J. V. 2011, Optical breakdown of air triggered by femtosecond laser filaments. *Applied Physics Letters* **99** (15), 151103 [see pp. 53 and 60]

PRUPPACHER, H. R. & KLETT, J. D. 1978, *Microphysics of clouds and precipitation*. Riedel Publishing Company [see pp. 26, 34, and 65]

PUSTOVALOV, V. & KHORUNZHII, I. 1992, Thermal and optical processes in shattering water aerosol droplets by intense optical radiation. *Int J. Heat Mass Transf.* **35**, 583–589 [see pp. 19 and 26]

QIU, J. & CRESSEY, D. 2008, Meteorology: Taming the sky. *Nature* **453** (7198), 970–974 [see p. 1]

RAMBO, P., SCHWARZ, J., & DIELS, J.-C. 2001, High-voltage electrical discharges induced by an ultrashort-pulse UV laser system. *Journal of Optics A: Pure and Applied Optics* **3** (2), 146 [see pp. 64 and 79]

RAYLEIGH, J. W. S. B. 1871, *On the scattering of light by small particles* [see p. 27]

REN, C., HEMKER, R. G., FONSECA, R. A., DUDA, B. J., & MORI, W. B. 2000, Mutual attraction of laser beams in plasmas: braided light. *Physical review letters* **85** (10), 2124–2127 [see p. 12]

RIZK, F. A. 2010, Analysis of space charge generating devices for lightning protection: performance in slow varying fields. *Power Delivery, IEEE Transactions on* **25** (3), 1996–2006 [see p. 63]

RODRIGUEZ, G., VALENZUELA, A. R., YELLAMPALLE, B., SCHMITT, M. J., & KIM, K.-Y. 2008, In-line holographic imaging and electron density extraction of ultrafast ionized air filaments. *Journal of the Optical Society of America B* **25** (12), 1988 [see p. 43]

RODRIGUEZ, M., BOURAYOU, R., MÉJEAN, G., KASPARIAN, J., YU, J., SALMON, E., SCHOLZ, A., STECKLUM, B., EISLÖFFEL, J., LAUX, U., *et al.* 2004, Kilometer-range nonlinear propagation of femtosecond laser pulses. *Physical Review E* **69** (3), 036607 [see pp. 2 and 8]

RODRÍGUEZ, M., SAUERBREY, R., WILLE, H., WOESTE, L., FUJII, T., ANDRÉ, Y.-B., MYSYROWICZ, A., KLINGBEIL, L., RETHMEIER, K., KALKNER, W., *et al.* 2002, Triggering and guiding megavolt discharges by use of laser-induced ionized filaments. *Optics letters* **27** (9), 772–774 [see p. 64]

ROGERS, T. M. & DESAI, R. C. 1989, Numerical study of late-stage coarsening for off-critical quenches in the Cahn-Hilliard equation of phase separation. *Phys. Rev. B* **39**, 11956–11964 [see p. 12]

ROHWETTER, P. 2011, *Investigations of atmospheric condensation induced by femtosecond laser filaments*. Ph.D. thesis, Freien Universität Berlin [see pp. 34 and 37]

ROHWETTER, P., KASPARIAN, J., STELMASZCZYK, K., HAO, Z., HENIN, S., LASCOUX, N., NAKAEMA, W. M., PETIT, Y., QUEISSER, M., SALAMÉ, R., *et al.* 2010, Laser-induced water condensation in air. *Nature Photonics* **4** (7), 451–456 [see pp. 2 and 33]

ROHWETTER, P., KASPARIAN, J., WÖSTE, L., & WOLF, J.-P. 2011, Modelling of HNO_3-mediated laser-induced condensation: A parametric study. *The Journal of chemical physics* **135**, 134703 [see p. 33]

ROSENTHAL, E. W., JHAJJ, N., WAHLSTRAND, J. K., & MILCHBERG, H. M. 2014, Collection of remote optical signals by air waveguides. *Optica* **1** (1), 5–9 [see p. 20]

SAATHOFF, H., HENIN, S., STELMASZCZYK, K., PETRARCA, M., DELAGRANGE, R., HAO, Z., LÜDER, J., MÖHLER, O., PETIT, Y., ROHWETTER, P., *et al.* 2013, Laser filament-induced aerosol formation. *Atmospheric Chemistry and Physics* **13** (9), 4593–4604 [see pp. 33 and 35]

SALAMÉ, R., LASCOUX, N., SALMON, E., KASPARIAN, J., & WOLF, J.-P. 2007, Propagation of laser filaments through an extended turbulent region. *Applied Physics Letters* **91**, 171106–171106 [see p. 19]

SALEEBY, S. M., COTTON, W. R., & FULLER, J. D. 2011, The cumulative impact of cloud droplet nucleating aerosols on orographic snowfall in Colorado. *Journal of Applied Meteorology and Climatology* **50** (3), 604–625 [see p. 1]

SATTMANN, R., STURM, V., & NOLL, R. 1995, Laser-induced breakdown spectroscopy of steel samples using multiple Q-switch Nd:YAG laser pulses. *Journal of Physics D: Applied Physics* **28** (10), 2181 [see p. 53]

SCHAEFER, V. J. 1950, Localized effects induced by seeding supercooled clouds with dry ice and silver iodide. *Science* **112**, 447–56 [see p. 1]

SCHELLER, M., MILLS, M. S., MIRI, M.-A., CHENG, W., MOLONEY, J. V., KOLESIK, M., POLYNKIN, P., & CHRISTODOULIDES, D. N. 2014, Externally refuelled optical filaments. *Nature Photonics* **8** (4), 297–301 [see p. 8]

SCHILLINGER, H. & SAUERBREY, R. 1999, Electrical conductivity of long plasma channels in air generated by self-guided femtosecond laser pulses. *Applied Physics B: Lasers and Optics* **68** (4), 753–756 [see p. 43]

SCHMITT-SODY, A., FRENCH, D., WHITE, W., LUCERO, A., ROACH, W. P., & HASSON, V. 2015, The importance of corona generation and leader formation during laser filament guided discharges in air. *Applied Physics Letters* **106** (12), 124101 [see p. 64]

SCHUBERT, E., BRISSET, J.-G., MATTHEWS, M., COURJAUD, A., KASPARIAN, J., & WOLF, J.-P. 2016a, Optimal laser-pulse energy partitioning for air ionization. *Physical Review A* **94** (3), 033824 [see p. 54]

SCHUBERT, E., DE LA CRUZ, L., MONGIN, D., KLINGEBIEL, S., SCHULTZE, M., METZGER, T., MICHEL, K., KASPARIAN, J., & WOLF, J.-P. 2016b, Dual-scale turbulence in filamenting laser beams at high average power. *Physical Review A* **94** (4), 043808 [see p. 19]

SCHUBERT, E., MONGIN, D., KASPARIAN, J., & WOLF, J.-P. 2015, Remote electrical arc suppression by laser filamentation. *Optics express* **23** (22), 28640–28648 [see p. 64]

SCHWARZ, J., RAMBO, P., DIELS, J.-C., KOLESIK, M., WRIGHT, E. M., & MOLONEY, J. V. 2000, Ultraviolet filamentation in air. *Optics Communications* **180** (4), 383–390 [see pp. 10, 11, 33, and 79]

SEINFELD, J. H. & PANDIS, S. N. 2006, *Atmospheric chemistry and physics: from air pollution to climate change*. John Wiley & Sons [see pp. 26, 28, 34, 35, and 37]

SHEN, Y. R. 1984, *The principles of nonlinear optics*. John Wiley & Sons [see p. 53]

Shim, B., Schrauth, S. E., Gaeta, A. L., Klein, M., & Fibich, G. 2012, Loss of phase of collapsing beams. *Physical Review Letters* **108** (4), 043902 [see p. 12]

Shim, B., Schrauth, S. E., Hensley, C. J., Vuong, L. T., Hui, P., Ishaaya, A. A., & Gaeta, A. L. 2010, Controlled interactions of femtosecond light filaments in air. *Physical Review A* **81** (6), 061803 [see p. 12]

Shneider, M., Zheltikov, A., & Miles, R. 2010, Long-lived laser-induced microwave plasma guides in the atmosphere: self-consistent plasma-dynamic analysis and numerical simulations. *Journal of Applied Physics* **108** (3), 033113 [see p. 58]

Shneider, M., Zheltikov, A., & Miles, R. 2011, Tailoring the air plasma with a double laser pulse. *Physics of Plasmas (1994-present)* **18** (6), 063509 [see p. 57]

Skupin, S., Bergé, L., Peschel, U., Lederer, F., Méjean, G., Yu, J., Kasparian, J., Salmon, E., Wolf, J.-P., Rodriguez, M., Wöste, L., Bourayou, R., & Sauerbrey, R. 2004a, Filamentation of femtosecond light pulses in the air: Turbulent cells versus long-range clusters. *Physical Review E* **70**, 046602–046602 [see pp. 12 and 14]

Skupin, S., Bergé, L., Peschel, U., & Luderer, F. 2004b, Interaction of femtosecond light filaments with obscurants in aerosols. *Physical Review Letters* **93** (2), 023901–023901 [see pp. 8 and 26]

Smetanin, I. V., Levchenko, A. O., Shutov, A. V., Ustinovskii, N. N., & Zvorykin, V. D. 2016, Role of coherent resonant nonlinear processes in the ultrashort KrF laser pulse propagation and filamentation in air. *Nuclear Instruments and Methods in Physics Research Section B: Beam Interactions with Materials and Atoms* **369**, 87–91 [see p. 11]

Stelmaszczyk, K., Rohwetter, P., Méjean, G., Yu, J., Salmon, E., Kasparian, J., Ackermann, R., Wolf, J.-P., & Wöste, L. 2004, Long-distance remote laser-induced breakdown spectroscopy using filamentation in air. *Applied Physics Letters* **85** (18), 3977 [see p. 14]

Stelmaszczyk, K., Rohwetter, P., Petit, Y., Fechner, M., Kasparian, J., Wolf, J.-P., & Wöste, L. 2009, White-light symmetrization by the interaction of multifilamenting beams. *Physical Reveiw A* **79**, 053856 [see p. 12]

Strickland, D. & Mourou, G. 1985, Compression of amplified chirped optical pulses. *Optics Communications* **56**, 219–219 [see pp. 1 and 5]

Sugiyama, K., Fujii, T., Miki, M., Yamaguchi, M., Zhidkov, A., Hotta, E., & Nemoto, K. 2009, Laser-filament-induced corona discharges and remote measurements of electric fields. *Optics letters* **34** (19), 2964–2966 [see pp. 64 and 71]

Sugiyama, K., Fujii, T., Miki, M., Zhidkov, A., Yamaguchi, M., Hotta, E., & Nemoto, K. 2010, Submicrosecond laser-filament-assisted corona bursts near a high-voltage electrode. *Physics of Plasmas (1994-present)* **17** (4), 043108 [see p. 64]

Sun, H., Liu, J., Wang, C., Ju, J., Wang, Z., Wang, W., Ge, X., Li, C., Chin, S. L., Li, R., & Xu, Z. 2013, Laser filamentation induced air-flow motion in a diffusion cloud chamber. *Optics Express* **21** (8), 9255–9266 [see p. 33]

THÉBERGE, F., DAIGLE, J.-F., KIEFFER, J.-C., VIDAL, F., & CHÂTEAUNEUF, M. 2017, Laser-guided energetic discharges over large air gaps by electric-field enhanced plasma filaments. *Scientific Reports* **7** [see p. 64]

THÉBERGE, F., LIU, W., SIMARD, P. T., BECKER, A., & CHIN, S. L. 2006, Plasma density inside a femtosecond laser filament in air: Strong dependence on external focusing. *Physical Review E* **74** (3), 036406 [see p. 61]

TIRUMALA, R. & GO, D. B. 2010, An analytical formulation for the modified Paschen's curve. *Applied Physics Letters* **97** (15), 151502 [see p. 64]

TOWNSEND, J. 1900, The conductivity produced in gases by the motion of negatively-charged ions. *Nature* **62**, 340–341 [see p. 65]

TZORTZAKIS, S., FRANCO, M. A., ANDRÉ, Y.-B., CHIRON, A., LAMOUROUX, B., PRADE, B. S., & MYSYROWICZ, A. 1999, Formation of a conducting channel in air by self-guided femtosecond laser pulses. *Physical Review E* **60** (4), R3505–R3507 [see p. 43]

TZORTZAKIS, S., MOUSTAIZIS, S. D., LAMOUROUX, B., CHIRON, A., FRANCO, M., PRADE, B., & MYSYROWICZ, A. 2000a, Nonlinear propagation of subpicosecond UV laser pulses in air. *Optics Letters* **25** (17), 1270–1272 [see pp. 10 and 79]

TZORTZAKIS, S., PRADE, B., FRANCO, M., & MYSYROWICZ, A. 2000b, Time evolution of the plasma channel at the trail of a self-guided IR femtosecond laser pulse in air. *Optics Communications* **181**, 123–127 [see p. 43]

UCHIDA, S., SHIMADA, Y., YASUDA, H., MOTOKOSHI, S., YAMANAKA, C., YAMANAKA, T., KAWASAKI, Z., & TSUBAKIMOTO, K. 1999, Laser-triggered lightning in field experiments. *Journal of Optical Technology* **66** (3), 199–202 [see pp. 2 and 64]

U.S. NATIONAL WEATHER SERVICE 2016, Thunderstorms, tornadoes, lightning... a preparedness guide. NOAA website, http://www.lightningsafety.noaa.gov/resources/ttl6-10.pdf, last verified 01/2017 [see p. 63]

VALDIVIA, J. A. 1997, *The physics of high altitude lightning*. Ph.D. thesis, University of Maryland College Park [see p. 58]

VIDAL, F., COMTOIS, D., CHIEN, C.-Y., DESPAROIS, A., LA FONTAINE, B., JOHNSTON, T. W., KIEFFER, J.-C., MERCURE, H. P., PÉPIN, H., & RIZK, F. A. 2000, Modeling the triggering of streamers in air by ultrashort laser pulses. *Plasma Science, IEEE Transactions on* **28** (2), 418–433 [see pp. 9, 26, 30, 43, 46, 60, and 69]

VOROBYEV, A. Y. & GUO, C. 2005, Enhanced absorptance of gold following multipulse femtosecond laser ablation. *Physical Review B* **72** (19), 195422 [see p. 53]

VUJICIC, N., SKENDEROVIC, H., BAN, T., AUMILER, D., & PICHLER, G. 2006, Low-density plasma channels generated by femtosecond pulses. *Applied Physics B-Lasers and Optics* **82** (3), 377–382 [see p. 43]

WANG, C., JIANG, L., WANG, F., LI, X., YUAN, Y. P., & TSAI, H. L. 2011, First-principles calculations of the electron dynamics during femtosecond laser pulse train material interactions. *Physics Letters A* **375** (36), 3200–3204 [see p. 53]

WANG, T.-J., WEI, Y., LIU, Y., CHEN, N., LIU, Y., JU, J., SUN, H., WANG, C., LU, H., LIU, J., *et al.* 2015, Direct observation of laser guided corona discharges. *Scientific reports* **5** [see p. 64]

WEITKAMP, C. 2006, *Lidar: range-resolved optical remote sensing of the atmosphere*, vol. 102. Springer Science & Business [see p. 1]

WILLE, H., RODRIGUEZ, M., KASPARIAN, J., MONDELAIN, D., YU, J., MYSYROWICZ, A., SAUERBREY, R., WOLF, J.-P., & WÖSTE, L. 2002, Teramobile: a mobile femtosecond-terawatt laser and detection system. *European Physical Journal - Applied Physics* **20** (3), 183–190 [see p. 13]

XI, T. T., LU, X., & ZHANG, J. 2006, Interaction of light filaments generated by femtosecond laser pulses in air. *Physical Review Letters* **96** (2), 025003 [see p. 12]

XU, S., SUN, X., ZENG, B., CHU, W., ZHAO, J., LIU, W., CHENG, Y., XU, Z., & CHIN, S. L. 2012, Simple method of measuring laser peak intensity inside femtosecond laser filament in air. *Optics Express* **20** (1), 299–307 [see p. 9]

YANG, J., ZENG, T., LIN, L., & LIU, W. 2015, Beam wandering of femtosecond laser filament in air. *Optics Express* **23** (20), 25628 [see pp. 20, 22, and 24]

YU, J., MONDELAIN, D., KASPARIAN, J., SALMON, E., GEFFROY, S., FAVRE, C., BOUTOU, V., & WOLF, J.-P. 2003, Sonographic probing of laser filaments in air. *Applied Optics* **42** (36), 7117–7117 [see pp. 9 and 43]

ZHANG, Z., LU, X., LIANG, W.-X., HAO, Z.-Q., ZHOU, M.-L., WANG, Z.-H., LIU, X., & ZHANG, J. 2009, Triggering and guiding HV discharge in air by filamentation of single and dual fs pulses. *Optics Express* **17** (5), 3461–3468 [see p. 53]

ZHAO, X. M., DIELS, J.-C., WANG, C. Y., & ELIZONDO, J. M. 1995, Femtosecond ultraviolet laser pulse induced lightning discharges in gases. *Quantum Electronics, IEEE Journal of* **31** (3), 599–612 [see pp. 2, 10, 43, 46, 48, 55, 56, 58, 59, 64, and 79]

ZHOU, B., AKTURK, S., PRADE, B., ANDRÉ, Y.-B., HOUARD, A., LIU, Y., FRANCO, M., D'AMICO, C., SALMON, E., HAO, Z.-Q., *et al.* 2009, Revival of femtosecond laser plasma filaments in air by a nanosecond laser. *Optics Express* **17** (14), 11450–11456 [see p. 53]

ZIPFEL, W. R., WILLIAMS, R. M., & WEBB, W. W. 2003, Nonlinear magic: multiphoton microscopy in the biosciences. *Nature biotechnology* **21** (11), 1369–1377 [see p. 1]

ZUEV, V. E., ZEMLYANOV, A. A., KOPYTIN, Y. D., & KUZIKOVSKII, A. V. 1984, *High-power laser radiation in atmospheric aerosols*. D. Reidel Publishing Company, Dordrecht / Boston / Lancaster [see p. 26]

Zvorykin, V. D., Ionin, A. A., Levchenko, A. O., Seleznev, L. V., Shutov, A. V., Sinitsyn, D. V., Smetanin, I. V., & Ustinovskii, N. N. 2015a, Multiple filamentation of supercritical UV laser beam in atmospheric air. *Nuclear Instruments and Methods in Physics Research Section B: Beam Interactions with Materials and Atoms* **355**, 227–231 [see p. 11]

Zvorykin, V. D., Ionin, A. A., Levchenko, A. O., Seleznev, L. V., Sinitsyn, D. V., Smetanin, I. V., Ustinovskii, N. N., & Shutov, A. V. 2015b, Extended plasma channels created by UV laser in air and their application to control electric discharges. *Plasma Physics Reports* **41** (2), 112–146 [see pp. 79 and 85]

Index

A

Absorption 26
Aerosols 35
  Accumulation mode 36
  Aitken mode 36
  Coarse mode 36
  Nucleation mode 36
Avalanche ionization 65

C

C_n^2 20
Capacitive probe 81
Capacity unloading 70
Carbon 35
Charge neutralization 70
Chirped pulse amplification (CPA) 1, 5
Cloud condensation nuclei (CCN) 37
Cloud seeding 1
Cluster 36
Cold ionization 65
Condensation nucleus (CN) 36
Corona 65
Critical power P_{cr} 7
Current measurement
  Electronic current 45, 46, 54
  Ionic current 45, 46
  Polarization response 45

D

Discharge probability 81
Discharge suppression 67
Discharge triggering 79

E

Eddy 20
Efficiency 27
electric breakdown 65
Electrical breakdown 65, 67
Electron
  Concentration 55
  Temperature 56
Electronic current signal 45, 50, 51
Energy reservoir 8
Equation of continuity 20
Extinction 27
Extinction paradox 28

F

Fast polarization signal 45, 49, 51
Filament 2, 5
Final jump 65

H

Heating rate 56
Hot ionization 65

I

Intensity clamping 8
Ionic current 45, 47, 51
Ionization
  Multi-photon 7
  Tunnel 7
Ions
  Kinetic temperature 56
  Negative ions concentration 56
  Positive ions concentration 56
  Vibrational temperature 56

K

Keldysh parameter 7
Kerr lens 7

L

Laser
  1030 nm 21, 28, 53

266 nm 79
3.9 µm 38
800 nm 12, 21, 44, 67, 70
Laser filament
Mid-infrared 10
Multiple filamentation 11
Near-infrared 10
Ultraviolet 10
Leader 65

M

Mid-infrared 10, 38
Mie theory 27

N

Near-infrared 9
Negative current peak 45, 49, 51
Nitrogen 34
Nonlinear refractive index 6
Nucleation 36
Heterogeneous 36
Homogeneous 36
Homomolecular 36

O

Optical Kerr effect 6
Optical Parametric Chirped Pulse Amplification (OPCPA) 10
Oxidation state 34

P

Particle
water droplet 26
Particle growth 37
Particle size 36
Parts per
billion (ppb) 34
million (ppm) 34
trillion (ppt) 34
Photo-dissociation 37
Photo-ionization 37
Photolysis 37
Photon bath 8
Plasma noise 9
Positive current peak 45, 50, 51
Positive swing 45, 47, 51
Pulse train 53

R

Relative humidity 36

S

Scattering 26
Self-focusing 7
Self-phase modulation (SPM) 8
Standard deviation σ_θ^2 21
Streamer 65
Sulfur 34
Supercontinuum generation 8
Supersaturation 37

T

Turbulence 20

U

Ultraviolet 10, 79

V

Volatile organic compounds (VOCs) . 35, 41
Voltage
DC 80

W

White-light generation 8